②

AD-A224 140

NAVAL POSTGRADUATE SCHOOL
Monterey, California

THESIS

NEAR-ANGLE SCATTERING AND BINARY OPTICS

by

Larry Vernon Chizek

December 1989

Thesis Advisor: John R. Neighbours

Approved for public release; distribution is unlimited.

REPORT DOCUMENTATION PAGE

1a REPORT SECURITY CLASSIFICATION UNCLASSIFIED	1b RESTRICTIVE MARKINGS
2a. SECURITY CLASSIFICATION AUTHORITY	3 DISTRIBUTION/AVAILABILITY OF REPORT
2b DECLASSIFICATION/DOWNGRADING SCHEDULE	APPROVED FOR PUBLIC RELEASE; DISTRIBUTION IS UNLIMITED.

4. PERFORMING ORGANIZATION REPORT NUMBER(S)	5 MONITORING ORGANIZATION REPORT NUMBER(S)

6a NAME OF PERFORMING ORGANIZATION NAVAL POSTGRADUATE SCHOOL	6b OFFICE SYMBOL (If applicable) 39	7a. NAME OF MONITORING ORGANIZATION NAVAL POSTGRADUATE SCHOOL
6c. ADDRESS (City, State, and ZIP Code) MONTEREY, CA 93943-5000		7b ADDRESS (City, State, and ZIP Code) MONTEREY, CA 93943-5000
8a. NAME OF FUNDING/SPONSORING ORGANIZATION	8b OFFICE SYMBOL (If applicable)	9 PROCUREMENT INSTRUMENT IDENTIFICATION NUMBER

8c ADDRESS (City, State, and ZIP Code)	10 SOURCE OF FUNDING NUMBERS			
	PROGRAM ELEMENT NO	PROJECT NO	TASK NO	WORK UNIT ACCESSION NO.

11 TITLE (Include Security Classification)

NEAR-ANGLE SCATTERING AND BINARY OPTICS

12. PERSONAL AUTHOR(S)
CHIZEK, LARRY VERNON

13a. TYPE OF REPORT MASTER'S THESIS	13b TIME COVERED FROM _____ TO _____	14 DATE OF REPORT (Year, Month, Day) 1989, DECEMBER	15 PAGE COUNT 126

16 SUPPLEMENTARY NOTATION   THE VIEWS EXPRESSED IN THIS THESIS ARE THOSE OF THE AUTHOR AND DO NOT REFLECT THE OFFICIAL POLICY OR POSITION OF THE DEPARTMENT OF DEFENSE OR THE U.S. GOVERNMENT.

17	COSATI CODES		18 SUBJECT TERMS (Continue on reverse if necessary and identify by block number)
FIELD	GROUP	SUB GROUP	BINARY OPTICS, DIFFRACTIVE OPTICS, NEAR-ANGLE SCATTERING

19 ABSTRACT (Continue on reverse if necessary and identify by block number)

THE RESEARCH OBJECTIVE WAS TO MEASURE NEAR-ANGLE SCATTERING (I.E., SCATTERING LESS THAN ONE DEGREE FROM THE SPECULAR BEAM) FROM A BINARY OPTIC AND DETERMINE IF A SCALAR SCATTERING THEORY COULD ADEQUATELY PREDICT SCATTERING PERFORMANCE. NEAR-ANGLE SCATTERING WAS MEASURED FROM A BINARY OPTIC BEAM SPLITTER. A SCALAR SCATTERING THEORY WAS DEVELOPED AND MODELED USING FORTRAN ON A PERSONAL COMPUTER; RESULTS FROM THE COMPUTER SIMULATION ARE COMPARED TO THE ACTUAL MEASUREMENTS.

THE SCALAR SCATTERING THEORY MODIFIES FRAUNHOFER DIFFRACTION BY INCLUDING TWO TYPES OF SURFACE TOPOGRAPHY WHICH CONTRIBUTE TO THE SCATTERING, SPECIFICALLY: 1) SURFACE ROUGHNESS DUE TO MICRO-IRREGULARITIES WHICH ARE CONSIDERED TO BE RANDOMLY DISTRIBUTED →

20 DISTRIBUTION/AVAILABILITY OF ABSTRACT XX UNCLASSIFIED/UNLIMITED ☐ SAME AS RPT ☐ DTIC USERS	21. ABSTRACT SECURITY CLASSIFICATION UNCLASSIFIED
22a NAME OF RESPONSIBLE INDIVIDUAL JOHN R. NEIGHBOURS	22b TELEPHONE (Include Area Code) (408) 646-2922	22c OFFICE SYMBOL 61NB

LINE #19 (CONT.)

AND 2) LARGE SCALE SURFACE FEATURES (I.E., THE BINARY STEP PATTERN) WHICH ARE DETERMINISTIC. THE RANDOM SURFACE ROUGHNESS, THE AUTOCORRELATION LENGTH OF THE ROUGHNESS, AND THE HEIGHT OF THE BINARY OPTIC'S PATTERN WERE DETERMINED USING A TALYSTEP SURFACE PROFILOMETER. THE SCALAR THEORY APPEARS TO GIVE GOOD RESULTS WHEN COMPARED TO THE MEASUREMENTS. HOWEVER, HIGHER VALUES WERE REQUIRED FOR THE SURFACE ROUGHNESS AND AUTOCORRELATION LENGTHS THAN THE TALYSTEP INDICATED, WHICH MAY BE DUE TO THE TALYSTEP'S SHORT SCAN LENGTH.

MILITARY AND SPACE APPLICATIONS FOR BINARY OPTICS ARE ALSO DISCUSSED.

NEAR-ANGLE SCATTERING AND BINARY OPTICS

by

Larry Vernon Chizek
Lieutenant, United States Navy
B.T., University of Idaho, 1983
B.S.E.E., Naval Postgraduate School, 1989

Submitted in partial fulfillment
of the requirements for the degree of

MASTER OF SCIENCE IN ELECTRICAL ENGINEERING

from the

NAVAL POSTGRADUATE SCHOOL
December 1989

Author: _____
Larry Vernon Chizek

Approved by: _____
John R. Neighbours, Thesis Advisor

_____
John R. Powers, Second Reader

_____
John P. Powers, Chairman, Department of
Electrical and Computer Engineering

iii

ABSTRACT

The research objective was to measure near-angle scattering (i.e., scattering less than one degree from the specular beam) from a binary optic and determine if a scalar scattering theory could adequately predict scattering performance. Near-angle scattering was measured from a binary optic beam splitter. A scalar scattering theory was developed and modeled using FORTRAN on a personal computer; results from the computer simulation are compared to the actual measurements.

The scalar scattering theory modifies Fraunhofer diffraction by including two types of surface topography which contribute to the scattering, specifically: 1) surface roughness due to micro-irregularities which are considered to be randomly distributed and 2) large scale surface features (i.e., the binary step pattern) which are deterministic. The random surface roughness, the autocorrelation length of the roughness, and the height of the binary optic's pattern were determined using a Talystep surface profilometer. The scalar theory appears to give good results when compared to the measurements. However, higher values were required for the surface roughness and autocorrelation lengths than the Talystep indicated, which may be due to the Talystep's short scan length.

Military and space applications for binary optics are also discussed.

TABLE OF CONTENTS

ACKNOWLEDGEMENT

I. INTRODUCTION

A. BINARY OPTICS

Binary optics is a revolutionary optical technology. Quality conventional optics are dependent on the skill of the lensmaker and the geometric form of the optic's surface. However, binary optics are designed with the aid of a computer and very large scale integrated (VLSI) lithographic technology. Binary optics get their name from the binary profile etched onto the optic's surface (Figure 1.1).
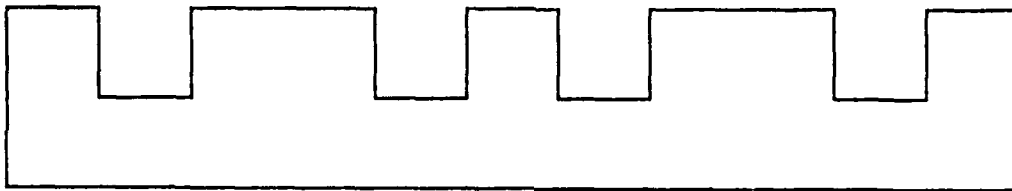
Figure 1.1 Profile of Binary Optic

Binary optics is also called diffractive optics. However, diffractive optics commonly refers to a multi-level or "staircase" pattern on the surface of the optic. The staircase pattern (Figure 1.2) is achieved by repeated application of binary masks, which is done to improve the efficiency.

1
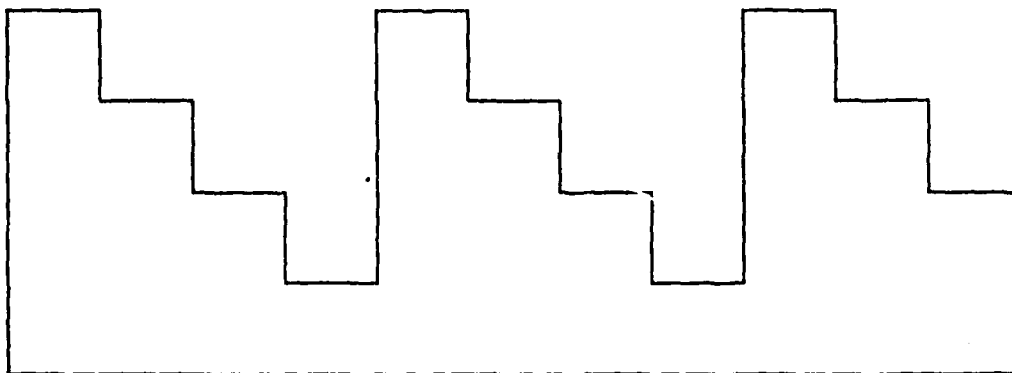
Figure 1.2 Profile of Diffractive (Binary) Optic

1. Definition of Binary Optics

Wilfrid Veldkamp, the developer of binary-optics technology, defines binary optics as:

> Binary optics is a aiffractive optics technology that uses computer generated designs of microscopic relief patterns and VLSI ion-etching technology. It creates novel diffractive optical devices and provides freedom and new materials choices for conventional refractive elements. It is a classical example of a technology transfer--from electronics to optics (and back). Through advances in VLSI technology patterns with characteristic dimensions as small as the wavelength of light can now be mass produced. The name binary optics, was coined to reflect a surface relief optics technology based on (1) a binary electronic mask technology (chrome on glass), (2) a binary mask design code, 2^N phase steps for N masks, and (3) a two level or high-low, ion etch process with uniform surface treatment. [Ref. 1]

2. Advantages of Binary Optics

Binary optics have several advantages over conventional optics, specifically:

- Multi-level binary optics can be made highly efficient.

- In a system design, use of binary elements may reduce the total number of elements, thereby saving weight. Additionally, certain applications may allow the binary

element to be embossed in plastic, which would provide a weight savings as well as the potential for cost savings.

- Binary optics can perform functions that conventional elements cannot perform.

- Binary optics allow flexibility in optical system design to generate compact optical shapes which will produce the desired optical wave front.

- Binary optics can save cost by correcting aberrations in conventional lenses, allowing a lower quality conventional lens to be used in the system. Additionally, binary optics can be used with conventional lenses to form an equivalent asphere or achromatized element which will be at a lower cost than using conventional optics.

B. APPLICATIONS FOR BINARY OPTICS

Binary optics are very versatile; they can serve as thin lenses, prisms, gratings, holograms, or phase plates. Impressively, binary optics are able to perform functions impossible with conventional optics, specifically they can function as high speed rotary scanners, multiplexers, filters, laser beam shapers and combiners. Currently, lithographic fabrication resolutions primarily limit the use of binary optics to the infrared (IR) and visible wavelengths. Binary lenses can be made in mass quantity and thus have the potential to lower optical component costs. Additionally, the binary elements can replace heavier conventional elements and in some cases reduce the number of lenses required in an optical system, simplifying and compacting the design while reducing the weight. Binary optics technology has broad applicability to military and space systems. [Ref. 2]

3

Unfortunately, binary optics is not the panacea for all optical needs; binary optics will never totally replace conventional optics. Binary optics operate using diffraction and are limited to narrow bandwidth applications. However, when you combine binary optics with conventional optics many desirable results may be obtained (e.g., improved optical performance for lower cost).

C. SCATTERING ANALYSIS

In the design and fabrication of optical systems, it is important to measure or know the level of scattering from optics. Experience indicates that even the best optical surfaces, fabricated using the best state-of-the-art (SOTA) polishing techniques, retain a microscopic scale surface roughness. Furthermore, even the best optical glasses have small local variations in their refractive indices. Both micro surface roughness and inhomogeneities within the glass produce refractive scatter on transmission. Additionally, micro surface roughness produces reflective scatter off the incident face of the optic, but this thesis addresses only the refractive scatter.

1. Benefits of Scattering Analysis

In a recent article concerning stray light analysis (scattering analysis falls under the definition of stray light analysis), system level managers are strongly urged to "first perform the required analyses and then plan on measuring the

assembled system to the best of their capability." The article also discusses benefits of scattering analysis which may be realized: [Ref. 3]

- Enhance or change design.

- Save misdirection of effort by preventing needless enhancements.

- Support a major decision during the development of a sensor.

- Perform tradeoff studies which can be used to help system level decisions.

D. NEAR-ANGLE SCATTERING FROM A BINARY OPTIC

1. Near-Angle Scattering Measurements

The research objective of this thesis was to measure near-angle scattering (i.e., scattering less than one degree from the specular beam) from a binary optic and determine if a scalar scattering theory could adequately predict scattering performance. Near-angle scattering is measured from a binary optic beam splitter manufactured by M.I.T. Lincoln Labs (see Chapter IV). The measurements were taken using a HeNe laser which is part of a near-angle scattering instrument developed by Douglas W. Ricks at the Naval Weapons Center, China Lake, California. [Ref. 4] From the scattering measurements, a qualitative indication of fabrication errors and manufacturing limitations as applied to binary optics may be obtained.

2. Scalar Scattering Theory

A scalar scattering theory was developed and modeled using FORTRAN on an IBM personal computer. Results from the

computer simulations were compared against the experimental scattering measurements (see Chapter V).

The scalar scattering theory modifies Fraunhofer diffraction by including two types of surface topography which contribute to the scattering, specifically:

- Surface roughness from micro-irregularities are considered to be randomly distributed on the surface.

- Large scale surface features (i.e., the binary step pattern) are deterministic.

The theory requires knowledge of the binary optic's random surface roughness, the autocorrelation length of the roughness, and the height of the binary pattern, which were determined using a Talystep surface profilometer. In Chapter V, the model's surface roughness and surface roughness autocorrelation length were adjusted to obtain the best fit between the scalar theory and the measurements. The scalar theory appears to give good results when higher values are used for surface roughness and autocorrelation length than the Talystep measurements indicated.

3. Advantages of Using a Scalar Scattering Theory

The primary advantage of using a scalar theory vice a full electromagnetic (EM) theory is in the relative simplicity of the theory and the reduction in computer time to perform the modeling, resulting in significant cost savings. A scalar theory is much simpler than a vector theory which must account for the phase and polarization of the light. In this thesis, a scalar scattering theory is

developed which is easily implemented on an IBM personal computer, thus providing an economical method of obtaining approximate performance based on the theory presented in Chapter V. The primary advantages of a scalar theory and the associated computer modeling, compared to the full EM theory, is twofold:

- Full EM theory requires a highly knowledgeable experimenter, it is complicated and cumbersome.

- Full EM theory is highly computer time intensive and therefore costly compared to a simple scalar model run on a personal computer (i.e., full EM theory may cost $100,000.00 using a full EM analysis program; alternately, the performance can be approximated on a personal computer for a few dollars using a scalar theory). However, the scalar theory does not yield an exact solution but provides a good approximation.

II. **FABRICATION OF BINARY OPTICS**

Binary optics is an emerging technology made possible by computer-aided design (CAD) tools, VLSI lithographic technology, and mathematical modeling of diffractive elements.

Binary optics are constructed of micron-sized rectangular (high/low) relief patterns on dielectric or metallic surfaces. By controlling the depth, width, and period of the pattern, the amplitude and phase of an EM wave is transformed to produce the desired optical transfer function. The same tools used in VLSI electronic circuit fabrication are used to fabricate binary optics.

The pattern formation is under computer control. Binary optics is named for the binary nature of making, etching, and coding techniques. Most of M.I.T.'s binary optics are made by contact printing the mask. The master lithographic mask is replicated onto a thin flexible glass mask, which is then vacuum contacted to the optical element so the flexible mask conforms to the surface, and then a contact print is made. However, for conventional optics aberration correction, the features are so large that one can simply projection print on curved or flat elements. Currently, M.I.T. Lincoln Labs is working on an extension of the technology which will allow the

diffractive patterns to be written directly onto the resist-coated optical elements with a laser beam, regardless of the curvature of the substrate. [Ref. 1]

Binary optics are truly based on an existing infrastructure of fabrication technologies; it borrows from the VLSI electronics field. Additionally, binary optics nicely matches with the replication and embossing technology developed by the video and compact disc (CD) industry. New "plastics" and polymers are now transmissive in the IR over large bandwidths and could be used to mold whole systems, giving binary-optics technology low cost potential. [Ref. 1]

A. HISTORY OF FABRICATION FOR BINARY OPTICS

In the beginning (i.e., the 1960's), a computer-generated hologram (CGH), which is used as the mask for a binary optic, was plotted on a greatly enlarged scale and then photoreduced to obtain the working CGH. "The primary drawbacks to this method are plotter precision, resolution and speed, accuracy of the photoreduction steps, and the relatively long fabrication times due to the multistep process." [Ref. 5] Recently (i.e., the 1980's), electron beam (E-beam) lithography has been used to plot CGHs directly to scale, thus eliminating the photoreduction steps. The primary disadvantages of this method are: E-beam lithographic systems are very costly to buy and maintain, and the effective writing time of the CGH can be quite long. Since the first systems

developed were for printed circuit applications, they typically had a relatively large pixel size and writing area. Based on the success of the larger area writers, industry developed high resolution writers (i.e., laser writers to generate the mask). [Ref. 5]

Veldkamp has stressed that binary optics are not CGHs. Binary optics is a more comprehensive technology than CGHs. Computer-generated holography is concerned only with the mask design of optical elements but binary optics includes such design as well as highly efficient fabrication and coding technology. The production of highly efficient optical elements is what makes binary optics unique. In real systems applications, high efficiency elements are required. Veldkamp says "binary holograms" (i.e., a two-level phase hologram) are, at best, 41% efficient with each element causing a loss of 60% of the incident light, the net result being low signal levels at the detector due to poor efficiency. Consequently, binary phase holograms found few system's applications. In the Defense Advanced Research Projects Agency (DARPA) Binary Optics Program, Dr. Veldkamp and coworkers at M.I.T. Lincoln Labs learned how to make holographic relief elements highly efficient. [Ref. 1]

High efficiency of binary optics is achieved by one of two methods. The first, relief structures can be constructed with a periodicity smaller than the wavelength of light but then the elements are very polarization and wavelength sensitive.

The preferred approach is to use structures larger than the wavelength of light, thus minimizing the polarization and wavelength effect. In the latter case, a staircase or multi-level pattern which is a repetitive mask application of the first method is used to achieve high diffraction efficiency. These staircase structures are used for broadband applications and M.I.T. Lincoln Labs have concentrated their research efforts in the last few years in this area. [Ref. 1]

B. OVERVIEW OF FABRICATION PROCESS

Figure 2.1 illustrates the overall design and fabrication process for making binary optics.

First, the binary optic is designed using an optical ray-trace program; a very popular one used by industry is CODE V (Optical Research Associates). CODE V generates a set of optimized phase coefficients defining the wave front phase map to be implemented, which is interpreted by in-house software for a particular pattern generator to define the mask for the lithography process. [Ref. 6] A primary constraint on the lens designer is that the minimum fringe spacing of the CGH does not exceed the resolution limit of lithographic mask generation hardware or alignment tolerances in the mask aligners. Additionally, the minimum period is equal to the minimum fringe spacing divided by the number of phase levels. Typically, E-beam machines are capable of eight micron fringe spacing. [Ref. 7]

The making of a binary optic is similar to ordinary CGHs; binary optics use high-resolution lithography to encode the
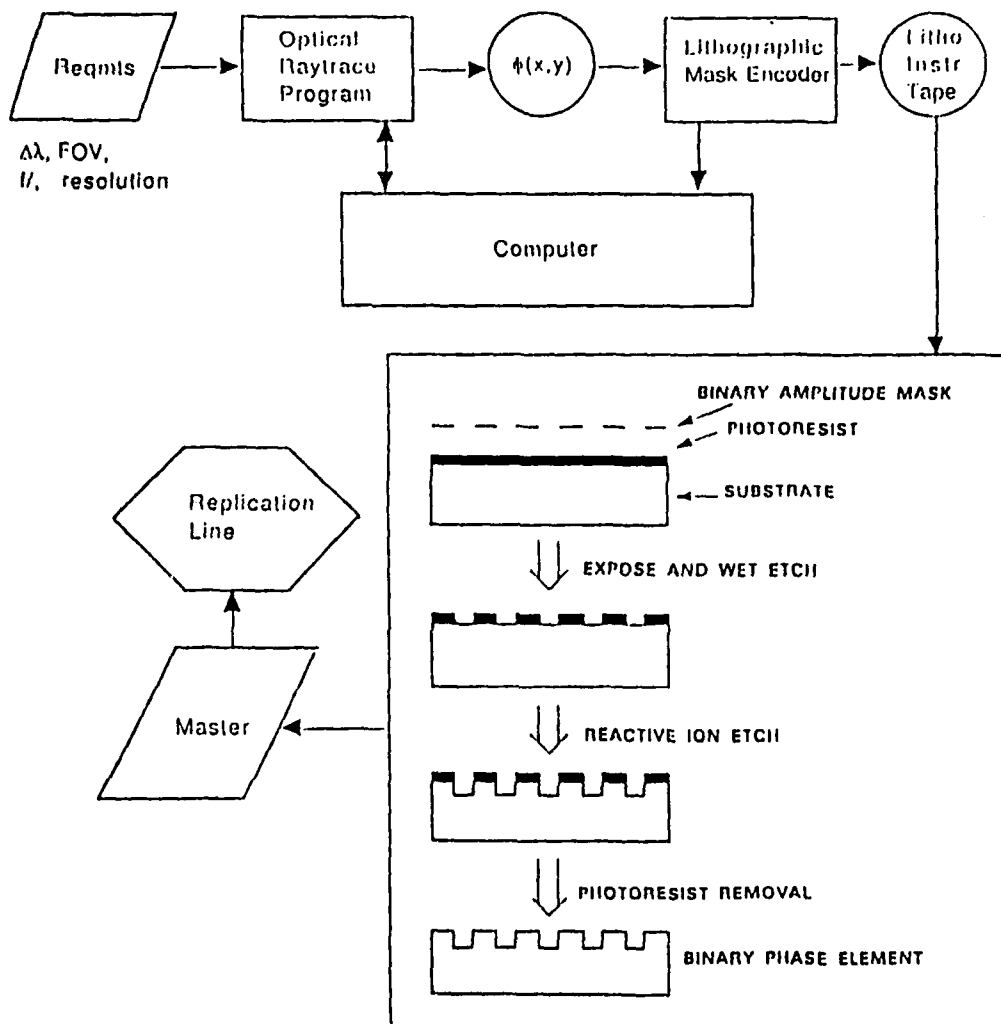
Figure 2.1   Overall Design and Fabrication Process for Binary Optics [after Ref. 6]

12

fringe patterns defining the optical transformation performed by the element. The lithographic mask represents the CGH and typically yields diffraction efficiencies of around ten percent. However, binary optics use the mask only to delineate regions of the substrate that are to be etched after the element is properly processed with photoresist. A diffractive optic made from repeated mask applications (i.e., a staircase structure) has very high efficiency (>95%).

Three broad types of binary optics are illustrated Figure 2.2.

Binary Elements

$T \sim \lambda$ $h \sim \lambda$

Fresnel Phase Lens

$T \gg \lambda$ $h < \lambda$
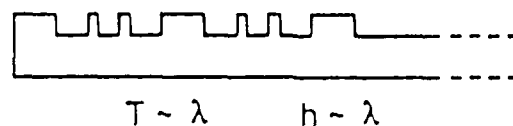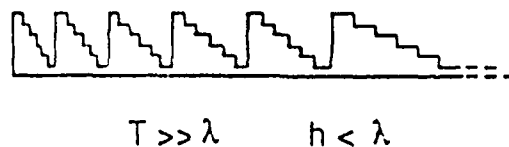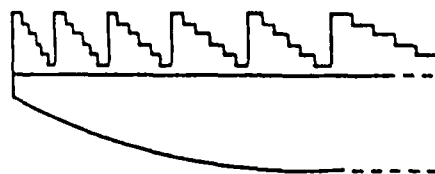
Mixed Optics

Figure 2.2   Types of Binary Optics [from Ref. 6]

13

A binary optic may be a simple two-level structure, a multi-level structure, or a mixed optic (i.e., a binary optic with a conventional optic). In general, binary elements can be made to operate for minimum wavelengths in the IR, while Fresnel phase lenses (multi-level binary optics are made with repeated mask applications) can extend down to the visible; the limitations are from current lithographic machine resolution. In principle, the binary surface can perform arbitrarily large transformations on the incident wave front. However, resolution limits of current lithographic machines restrict the optical power (focusing ability) of the binary surface.

1. **Mask Formation**

Various E-beam and optic lithographic mask-making machines are available with steps ranging from 0.1 to 1.1 micron (μm); a list is provided in Reference 6.

a. **E-beam**

Long exposures, in excess of 20 hours, can have unusually low yield factors. Perkin Elmer cites a yield of 40% for a 25 hour exposure using their E-beam machine, Manufacturing Electron Beam Exposure System (MEBES-III). A rough rule of thumb for the effect of pixel size on exposure time is that cutting the pixel size in half, may triple the exposure time. The exposure time lengthens since the number of stripes (lengthwise pass over the surface) increases by a factor of four and doubles the number of figures (shapes)

14

required to generate the pattern. The number of stripes covering the pattern to be exposed is directly related to the exposure time required, where stripe size is a function of pixel size. [Ref. 8]

E-beam machines can use different geometrical figures in writing their patterns (i.e., parallelograms, rectangles, and trapezoids), and the choice of the shape influences the exposure time. Typically, rectangles are processed faster than parallelograms which are processed faster than trapezoids; the additional processing time is from the requirement to convert diagonal lines to a raster pattern while loading the stripe memory buffer. [Ref. 8]

There are two major differences between the VLSI and CGH patterns: [Ref. 9]

- The volume of data describing a CGH pattern is generally much greater than that of a VSLI pattern.

- CGH patterns usually consist of a very small set of primitive shapes.

Research labs and industry have developed their own in-house software to generate the mask from the optical ray-trace program's output to control the pattern writing machine. General rules to keep the size of the data to manageable proportions for the mask are: [Ref. 9]

- The hologram pattern should generate the smallest number of primitive shapes (NPS) since the data is proportional to the NPS. Orientation of the patterns is also important (e.g., rectangular shapes oriented along the x-y axes generate less data than patterns consisting of curved lines in arbitrary directions).

- The amount of graphical data is a function of the CAD application that generates the data. A tradeoff exists between processing speed and compact storage of data. Organization of small clusters of data into larger ones compacts the data, but lengthens the computer access time.

- In VLSI applications (i.e., low data volumes), data fracturing programs are useful, but current CAD systems do not efficiently handle fracturing of CGH data. Therefore, special software is required for efficiency reasons.

- Significant improvements in CGH design and fabrication are achieved if the CAD and E-beam machine are both available at the same location and connected together. CGH design and recording in parallel is thereby accomplished, thus reducing graphical data storage requirements and total fabrication times by significant amounts. Moreover, complex CGHs can be fabricated because the graphical data is generated in segments (i.e., as the E-beam machine is writing the previously generated segment, the CAD system can generate the next batch of data).

b. Laser writers

Today, the majority of the patterns are generated using E-beam pattern generators. Many of the micro-applications require high resolution, requiring use of an E-beam generator. However, mask sets for 0.1 to 2.0 in binary diffractive optics can be rapidly generated on high resolution laser writers such as Texas Instrument's Laserad system. Currently, Texas Instruments has demonstrated the capability to use their laser writer to develop a simple Fresnel zone plate lens designed for use at 10 μm wavelength. The advantage of using a laser writer compared to an E-beam pattern generator are: [Ref. 5]

- The laser writer is less costly to operate and maintain.

- The laser writer has a higher effective throughput.

16

Effective pixel sizes range from 10 um to 0.5 μm for laser writers. Texas Instruments developed the Laserad system to plot photomasks for typical semiconductor applications. The Laserad I has position and overlay accuracies of better than 0.25 μm, which is useful for generation of multi-level binary optics.

2. Reactive Ion Etching

The fabrication of an N-level (multi-level) profile requires precision photolithography and processing. The masks for each relief level are used to contact print a similar relief profile in photoresist spun on the surface of the substrate. The processed photoresist consists of areas of bare surface or photoresist (unexposed areas). After subsequent material removal by reactive ion etching, a profile of etched and unetched areas is produced. The photoresist acts as an etching barrier. Reactive ion etching allows a precise way of removing material anisotropically at the atomic level. In reactive ion etching, a plasma is created from the reactive atoms over the surface to be etched, thus enhancing the efficiency and precision of material removal. The process of producing photoresist patterns and then etching relief structures is repeated N times with N different masks, requiring complete re⁻ :ration, to produce an N-level relief (multi-level or s⁺..ircase) pattern of different depths and heights. The key steps in fabricating a binary element are:

- Accurate registration of the N-level masks.

- Precise control of depth and profile of material removed.

Hence, the mask aligner and reactive ion etches are the critical pieces of equipment. [Ref. 7]

3. **Embossing a Binary Optic in Plastic**

The embossing technique involves the following major steps:

- The CGH is recorded in photoresist.

- A master metal replica is formed by electroplating the photoresist pattern.

- The metal master or a metal replica is used to repeatedly emboss its pattern into plastic. [Ref. 10]

Polaroid fabricates the metal master from nickel. The developed photoresist plate is coated with a vacuum evaporated layer of silver, making it electrically conductive, and is immersed in an electroplating bath consisting of an electrolyte and a nickel anode. The resist plate acts as the cathode and a layer of nickel is plated onto the resist surface. Afterwards, the resist plate is stripped away, the nickel plate can be used for embossing. The nickel plate has a surface relief profile which is the mirror image of the original CGH pattern in the photoresist, making the pattern which is impressed into the plastic the same as the photoresist's. The plate can be mounted into a machine which allows for continuous embossing into plastic. The plastic must be softened by either heat, pressure, solvent or a

18

combination of these. Typical plastics used for embossing are vinyl, polycarbonate, mylar, or cellulose esters. [Ref. 10]

Currently, M.I.T. Lincoln Labs, Polaroid, and 3M have demonstrated the ability to fabricate a binary optic in plastic. 3M Corporation mass produces commercially a binary optic used in a diffractive bifocal intraocular lens. [Ref. 11] The replication (embossing) technology is the same used to manufacture CDs. Additionally new plastics transmissive in the IR are also available. [Ref. 1] If the lenses are produced in quantity, this technology is critical to lightweight and low-cost optics.

III. **MILITARY AND SPACE APPLICATIONS**
FOR BINARY OPTICS

The applications of binary optics to military and space systems is in its infancy; most current applications are still in the research and development stage. In the future, binary optics may be routinely used for: solar concentrators for solar panels, combining two-dimensional arrays of semiconductor lasers to produce a single powerful coherent laser beam, beam sampling, reshaping of laser beams for particular energy distribution, laser beam multiplexing for communication systems, beam steering, optical storage devices, head-up displays for pilots and astronauts, telescopes, and numerous other applications.

Veldkamp divides binary optics into two classes of applications. Currently, the most attention is directed toward basic aberration correction with large features on flat and curved elements, and the direction is toward larger optics. The goal is to perform conventional aberration corrections: better, cheaper, and lighter. The second class of binary optics is comprised of hundreds of thousands of micro-optic elements of a few-inch-diameter wafer (e.g., microfine structures for delicate switching functions, multiplexers, filters, and amacronic sensors). [Ref. 1]

This chapter summarizes current applications and speculates on the future for binary optics. Currently, both industry and research labs are trying to determine how to best exploit this new technology which has been called an "optical revolution," which will change the way future optical systems are designed.

A. USING CONVENTIONAL OPTICS WITH BINARY OPTICS

1. Equivalent Asphere

A low-cost, conventional, spherical element can have a pattern etched onto the back surface and turn the lens into an equivalent asphere. Cost and producibility motivate this mix of conventional optics with binary optics. [Ref. 1]

2. Deliberate Dispersion

Diffractive rings can be etched onto a surface in order to achieve a deliberate amount of dispersion into the element. Since this dispersion is opposite to most refractive dispersion, an achromatized element (i.e., all colors in a waveband focus at the same spot) can be made by balancing the mix of refraction and dispersion. [Ref. 1]

Therefore, binary etch patterns allow control of both the surface profile of an element (asphericity) and the bulk properties of the material (dispersion).

3. Correction of Spherical and Chromatic Aberrations

When the staircase patterns are used to correct for spherical and chromatic aberrations in conventional elements,

the spherical curved surfaces of the conventional element performs the raw focusing power, and the features of the corrective diffraction patterns can be very large (e.g., typically hundreds of microns in width). Since the features are larger than the wavelength of light, they become polarization-independent and color insensitive. Typical IR aberration corrections can be several hundred microns or more in width, and two or three microns in depth. However, depending on the application, features can also be submicron in scale. For example, fast planar optics (f/1) used as micro-lenses in front of detector arrays have the smallest lithographic feature as:

$$s = \frac{\lambda f}{N} \qquad (3.1)$$

where

s = size of lithographic feature,
λ = wavelength,
f = f number of the lens, and
N = number of phase levels.

Therefore, features can be submicron in scale, depending on the application. [Ref. 1]

4. IR Applications

Binary optics can improve the performance of IR systems when combined with refractive elements. Additionally, arbitrary phase profiles are possible since the elements are computer generated. Possible applications include forward looking infrared (FLIR) systems, laser radar sensors, and

other laser applications (i.e., beam profile shaping and beam combining from diode arrays).

In general, optical systems are confined to spherical surfaces. Aspheric surfaces can be used to reduce the number of elements but are significantly more expensive to manufacture. The majority of IR lens elements are made from germanium, silicon, and zinc selenide. Unfortunately, these materials are inherently dispersive and therefore require optical systems with more elements to correct for the dispersion. However, by etching a diffractive surface onto a conventional refractive surface, the diffractive surface can correct for the dispersion and thereby reduce the number of required elements. The reasons for making a hybrid (combination diffractive and refractive) lens are: [Ref. 12]

- The easily manufactured spherical surface can do the majority of the focusing.

- The tolerances of making and aligning the diffractive masks are significantly reduced.

- Spherical surfaces are inherently better in minimizing off-axis aberrations over a finite field of view.

- The operative wavelength band of the system is greatly increased over that of a completely diffractive element.

a. Broadband IR Imaging

Information in this section is summarized from research by Fritz and Cox. [Ref. 13]

Fritz and Cox investigated two optical designs for IR imagers, a fast staring system using an f/1 lens (field of 6 degrees) and a slower scanning system using an f/2.4 lens

23

(field of 1.5 degrees). Their designs included hybrid refractive/diffractive elements as replacements for conventional spherical elements for use in the eight to twelve micron band. The diffractive element is used to apply aspheric or chromatic corrections.

Mosaic arrays of uncooled detectors for low-cost staring systems require fast (<f/1) optics. Fritz and Cox found that the sensitive dependence of spherochromatic aberrations (introduced by the binary optic) on f number limit the performance improvements for a fast system (e.g., an uncooled staring system). A f/1 triplet of conventional spherical elements cannot be replaced by a hybrid system of two spherical elements, each with an aspheric diffractive surface while maintaining resolution over the desired field of view and bandwidth. However, a 33% reduction in the number of elements could be achieved in the slower system using the hybrid elements with no loss in resolution, field of view, or bandwidth.

B. IR FILTERS

Dale Byrne has fabricated diffractive IR filters using microlithographic techniques; the minimum feature sizes less than 0.25 μm for use as mesh filters with near and middle IR. These meshes may be used in applications like optically pumping far IR lasers which use a hybrid metal mesh dielectric mirror to have a high reflectivity at the pump's wavelength,

partial reflectivity and low absorptivity at the lasing wavelength, and couples a broad area of the laser mode. [Ref. 14] Previously, three different mesh filters were used for ground based millimeter wave astronomical measurements and metal meshes were used as spectral filters in a far IR and submillimeter wavelength satellite radiometer. [Ref. 15]

C. COHERENT LASER ARRAY BEAM ADDITION

This section summarizes research by M.I.T. Lincoln Labs concerning coherent laser array beam addition. [Ref. 16]

Coherent laser beam addition offers the potential to combine the power from many individual lasers into one extremely powerful coherent beam. The three techniques involved each use binary optics and can be employed to produce diffraction-limited laser sources from large two-dimensional arrays of laser diodes or by combining the output of several gas lasers. Specifically, the three techniques are: superposition using binary phase gratings, aperture filling by amplitude-to-phase conversion, and aperture filling by coupled microcavities.

Currently, an individual diode laser is limited to approximately 25 milliwatts (mW) of power to prevent facet damage and device heating. Arrays of laser diodes overcome the heating problem by designing adequate space between lasers with the proper heat sinks; naturally, the power of each laser is limited in order to prevent facet damage. The collective

output of today's diode arrays is several hundred watts of quasi-continuous wave (CW) power with larger CW and pulsed arrays under laboratory development. Two-dimensional laser arrays have the potential of achieving power densities of over 1 kilowatt per square centimeter.

Power is extremely important if the laser is to be used as an illuminator, multimode fiber source, or laser pump. In some applications, power concentration and the far-field behavior is equally important; these applications include laser radar, optical communications, single-mode fiber sources, and optical printing. Arrays of mutually incoherent lasers have a low degree of spatial coherence across the array; therefore, if laser diodes are to be used for these applications, the outputs of the individual lasers must be combined coherently in order to achieve high luminance (luminance is a measure of power per unit area per unit solid angle and is sometimes called brightness). To achieve high luminance and optimal far-field performance from laser diode arrays, three conditions must be met:

- Mutual coherence must be established across the array insuring good spatial coherence for good collimation and focusing properties.

- The phases of the lasers must be adjusted to provide the maximum power along the optical axis. Improper phasing results in beam broadening and reduced power along the optical axis.

- The wave front emanating from the array is modified to produce a single lobed far-field pattern. The far-field pattern of an in-phase array consists of several narrow beams called beam combining.

26

It is of special interest to note that there are no conventional optic counterparts for the following methods of beam combining (i.e., binary optics are critical to the design).

1. Superposition using Binary Phase Gratings

The laser beams in the array may be combined via a binary phase grating to superimpose N lasing apertures, making the array effectively appear as a single emitter with N times the power density of single laser diode. The power per unit area increases by a factor of N while the divergence remains constant and the luminance increases by a factor of N, also. The laser beams are made to cross each other at a particular point in space, the resulting interference pattern is $|E(x,y)|\exp[j(x,y)]$ which is dependent on the beam angles and respective phases of the lasers. The binary phase grating is positioned in the interference plane to convert the field into a single beam. For perfect plane wave beam conversion, the transmittance of the grating, $t(x,y)$, is the reciprocal of the interference, namely:

$$t(x,y) = \frac{1}{|E(x,y)|} \exp\left\{-j\phi(x,y)\right\} \tag{3.2}$$

The transmittance is less than or equal to one; any absorption will produce a loss in laser power, so the amplitude transmittance is chosen to be unity, and the amplitude component of the interference pattern is not corrected. However, the phase term is corrected by

27

constructing a grating to give the desired phase from Equation 3.2. After the light passes through the conjugate phase grating, the light amplitude coupled into the zero order beam, A_o, is given by the average of the resultant field:

$$A_o = \int\int_{-\infty}^{+\infty} |E(x,y)|\, dx\, dy \qquad (3.3)$$

The grating coupling efficiency is maximized by choosing the phases of the lasers that produce an interference amplitude $|E(x,y)|$ which maximizes Equation 3.3. For example, six lasers are maximized using laser phases of π, π, 0, 0, π and π, resulting in a coupling efficiency of 81% using Equation 3.3.

The binary phase grating is placed inside a common cavity for the lasers (Figure 3.1) and combines the output into a single beam. Of particular interest is the fact that it can
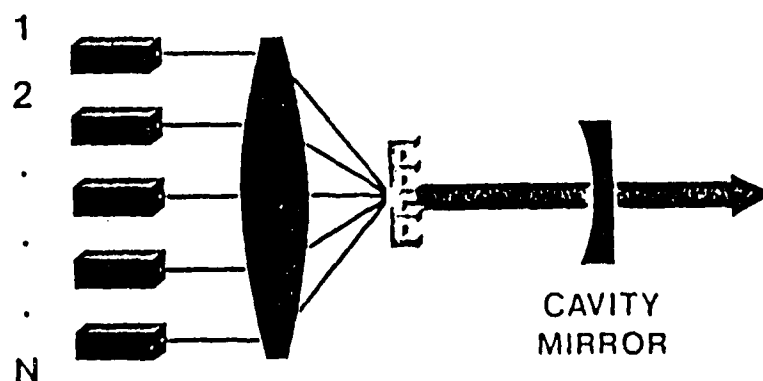

Figure 3.1 Superposition of Laser Diodes using a Binary Phase Grating [from Ref. 12]

28

be shown that the combining efficiency is identical to the efficiency of splitting a single beam into N separate beams (i.e., a good beam splitter is also a good combiner). Veldkamp used iterative techniques to optimize the desired diffraction pattern in a least squares sense for the combination of six laser beams; the six lasers were positioned along the +/- 1, 2, and 3 diffraction orders of the grating.

The angular plane wave spectrum of the grating output is shown in Figure 3.2 and the far-field output of the six lasers is compared with a single laser (scaled in intensity) in Figure 3.3.

Although this technique has also been applied to HeNe lasers and CO_2 lasers, it is most appropriate for low divergence sources where additional collimation of the laser beams is unnecessary. High divergence sources (e.g., semiconductor lasers) require collimating optics; therefore, this method is limited to small arrays of semiconductor lasers.

2. Aperture Filling by Amplitude-to-Phase Conversion

Aperture filling combines the laser beams by spreading the light uniformly across the entire laser array. The desired light distribution is uniform in amplitude and phase; the distribution is approximated by using binary elements to perform the required spatial filtering and phase correction. This method differs from superposition in that coherence is

INTENSITY

-10 -8 -6 -4 -2 0 2 4 6 8 10

DIFFRACTION ORDER
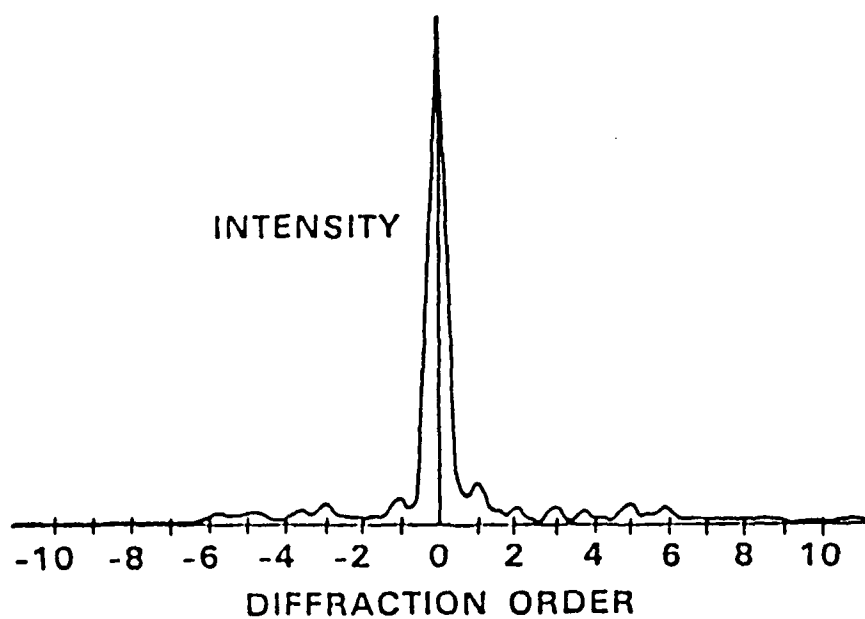
**Figure 3.2   Angular Plane Wave Spectra of Combined
Laser Output [from Ref. 12]**

——— SIX LASERS
——— ONE LASER

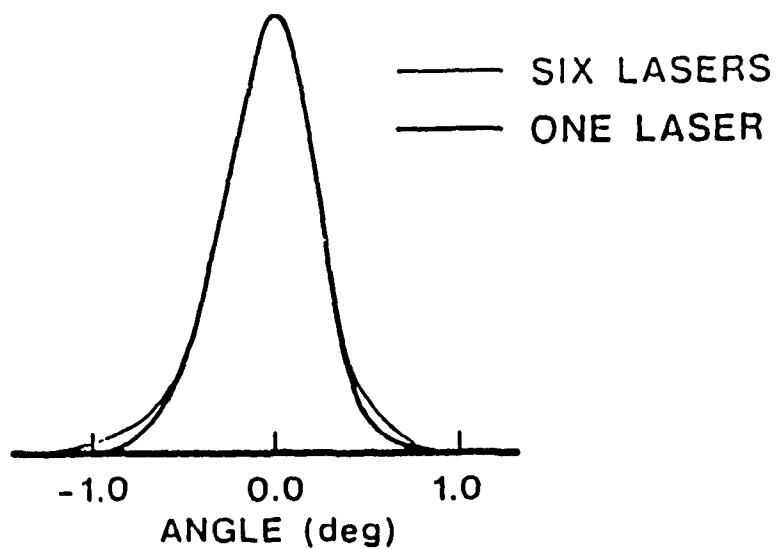-1.0   0.0   1.0

ANGLE (deg)

**Figure 3.3   Far-Field Output of Combined Beam Compared
with Single Beam [from Ref. 12]**

30

provided by the design of the array and not an external cavity. The array radiates in-phase so the phase component of the electric field is constant. However, the amplitude component of the fields are nonuniform due to the laser separation and their Gaussian mode structure; this amplitude variation produces unwanted grating lobes in the far-field. It can be shown that the percentage of energy in the central grating lobe equals the ratio of the area of the laser apertures to the area of the entire array; this ratio is defined as the **fill factor**. The remaining energy resides in higher order grating lobes.

In this technique, two binary optical elements are required. The first element transforms the field by altering the phase to get the amplitude approximately constant and the *second element*, a phase-correcting plate, removes the phase variation introduced by the first. Both elements affect only the phase so no light is lost in the combining process; in theory, 100% of the light from an ideal array can be coupled into the central lobe. Computer simulations indicate coupling efficiencies of greater than 95% are possible with many real laser arrays.

Figure 3.4 shows results from combining a ten-element AlGaAs array containing 2.4 micrometer laser sources spaced by six micrometers. Figure 3.5 shows aperture filling almost doubled the intensity in the main lobe (91% vice 51% of the total power produced by the array).
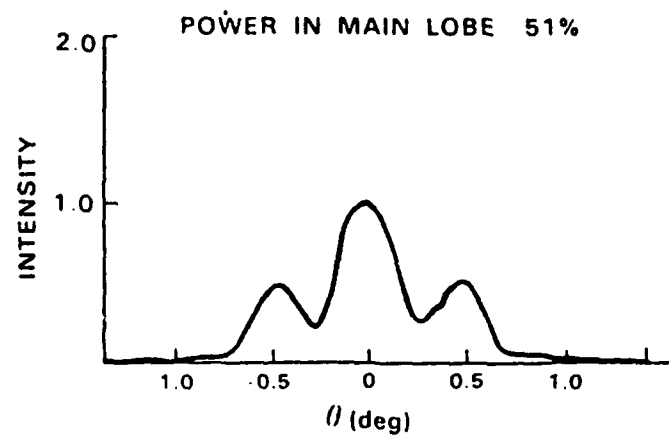
31

POWER IN MAIN LOBE 51%

Figure 3.4 Before Aperture Filling [from Ref. 12]

POWER IN MAIN LOBE 90%
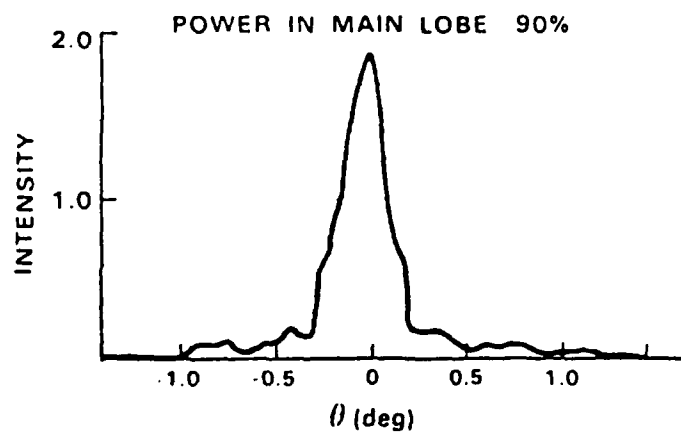
Figure 3.5 After Aperture Filling [from Ref. 12]

32

The aperture filling technique yields a diffraction-limited far-field beam which is inversely proportional to the transverse dimension of the laser array vice the individual laser. Consequently, smaller diffraction spots and lower beam divergence is achievable without the use of beam-expanding optical elements; this feature allows simplification of some optical systems. This technique is limited to lasers with fill factors greater than 25%.

Aperture filling may also be applied to beam combining of phased arrays of lasers for beam steering applications. Additionally, this method can be cascaded in order to transfer 100% of the power into another system (e.g., use as a laser pump).

3. Aperture Filling by Coupled Microcavities

Diffractive microlens technology and Fresnel diffraction are used to create an array of small coupled laser cavities. The coupling locks the laser cavities together coherently and produces a narrow far-field pattern. The microlenses uniformly spread out the light via diffraction across the array, thereby producing the desired light into the central lobe of the far-field. The small apertures of semiconductor lasers have beams which expand into a cone of 20 to 30 degrees and intersect with adjacent lasers a few hundred microns from the aperture. Collimating each laser beam at this point results in the desired uniform phase and quasi-uniform intensity of the wave front.

33

An array of diffractive optical elements is used which have the flexibility and precision required to adapt to virtually any size and shape. The lens requirements are quite strict but are achievable with binary optics, specifically:

- The lens size must equal spacing of the lasers; typically ranging from ten to several hundred microns.

- Each lens must be located as close to its neighbor as possible.

- The shape of the lens aperture may be noncircular.

- The lens should have low f number for efficient light collection.

- Diffractive and absorptive losses must be low.

- Each lens must produce an aberration-free collimated beam.

- Each lens needs to have the ability to correct for aberrations in the original laser beam.

a. Coupling Microcavities by Talbot Self Imaging

Talbot discovered that illuminating a periodic object with coherent light produces an image at regular intervals due to free space diffraction. [Ref. 17] The diffraction pattern of the array has self imaging properties but each element also has diffracted light which continues to expand contributing to several elements in the first self image. This property is combined with Talbot imaging of the entire array to form a Talbot cavity. Light from a single laser is reflected from an external mirror which provides feedback to all the other lasers in order to ensure coherence. The output mirror is positioned so that one cavity trip corresponds to the Talbot distance, ensuring the free space

34

diffraction from the entire laser array produces a self image of the original laser apertures, allowing light to couple efficiently into the individual laser waveguides. If the lasers are not mutually coherent, the Talbot effect does not apply and no self image is formed. Consequently, much of the light falls between the laser apertures and is lost. Since the best efficiency only occurs for coherent operation, the system acts in a manner to sustain the coherent output.

Lincoln Labs has used a linear array of AlGaAs diodes which used a Talbot cavity (Figure 3.6). The lasers are collimated using a microlens array and a Talbot cavity was formed by placing a planar mirror half the Talbot distance from the microlens array.

The far-field pattern from six laser diodes is shown in Figure 3.7. The unlocked phase illustrates the output without the mirror positioned to satisfy the Talbot condition and the in-phase output illustrates the output for the mirror position satisfying the Talbot condition. The far-field pattern of Figure 3.7 was almost diffraction limited; 85% of the energy was in the central lobe. Spectral analysis of the lasers showed lasing occurred for a common wavelength and all the lasers were locked in-phase.

The beam shaping and aberration correction abilities of microlenses are particularly suited to combining large arrays of two dimensional diode lasers. Additionally,
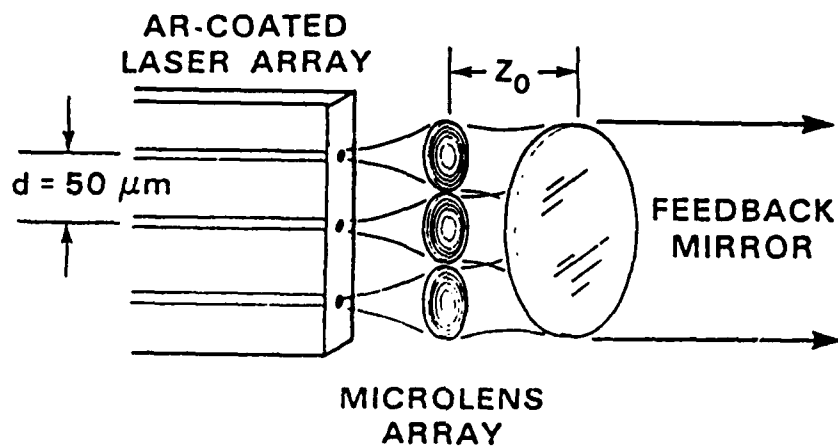
Figure 3.6 Coupling Microcavity using Talbot Self Imaging [from Ref. 12]
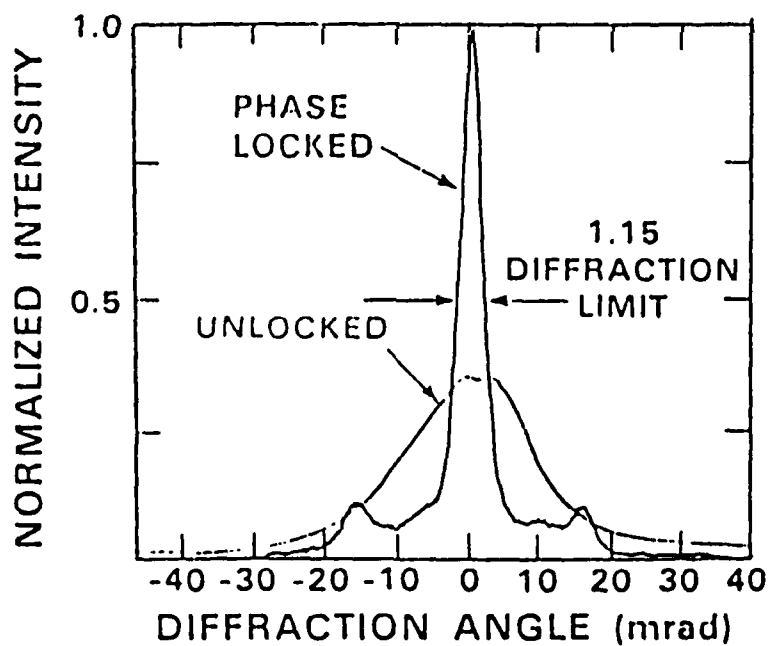
Figure 3.7 Far-Field Pattern for Microcavity Coupling [from Ref. 12]

the entire system can be enclosed in a single substrate (Figure 3.8). The microlens array is etched into the front surface of the substrate, and a partially reflecting mirror is placed on the back surface. The thickness of the substrate satisfies the Talbot self-imaging condition.

SURFACE
EMITTING
LASERS

DIFFRACTIVE
LENSLET
ARRAY

OUTPUT
MIRROR

COHERENT
OUTPUT

MONOLITHIC DIODE
LASER ARRAY

BEAM COMBINER

z_0
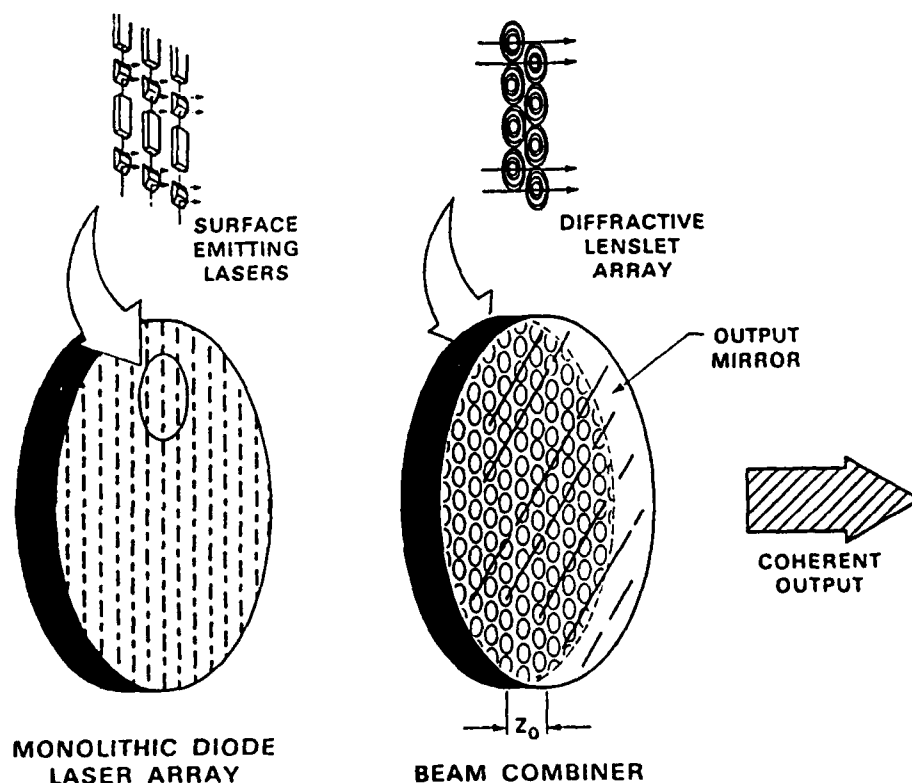
**Figure 3.8 Microlens Array in Single Substrate
[from Ref. 12]**

4. <u>**Advantages of Laser Beam Addition**</u>

Reliability is a key issue for any military or space system. Each of the methods of beam combination is immune to catastrophic failure since a single laser failure only

slightly diminishes the system's power output. The high
efficiency and reliability of these applications to laser
diode arrays makes them ideally suited to military and space
applications.

D. LASER BEAM PROFILE SHAPING

This section summarizes research by M.I.T. Lincoln Labs
concerning laser beam profile shaping. [Ref. 18]

Veldkamp at M.I.T. Lincoln Labs has shaped a far-field
laser beam profile from a Gaussian into a uniform intensity
profile in either one or two dimensions. Uniform intensity
profiles are needed in particular applications, such as laser
radar systems utilizing heterodyning detector arrays, laser
fusion, optical data processing, industrial laser heat
treating of material surfaces, semiconductor annealing of
material defects, vaporization of deposition materials, and
improvements in energy extraction efficiency from high energy
lasers. [Ref. 19]

For power efficiency reasons, energy redistribution is
more desirable than selective attenuation of the beam to
achieve the desired profile. In a laser radar, the far-field
intensity pattern must match the far-field projected image of
the linear detector array, known as the radar footprint, with
a uniform intensity. An N-fold beam compression was used to
achieve the necessary far-field beam eccentricity for
efficient coverage of the detector array's footprint. The

38

conversion of the Gaussian profile to a sinc profile was achieved by spatial phase modulation of the beams using a binary diffraction grating. The grating produced constructive and destructive interference to help flatten the profile.

The process is simply done in two steps. First, the laser beam intensity distribution is converted to a sinc function. Next, the beam profile undergoes an N:1 anamorphic compression. Compression in the near-field results in expansion in the far-field in order to match the rectangular extent of the N-element array's footprint. As seen in Figure 3.9, the shaper is composed of one phase grating and two one-dimensional anamorphic compressors.

A far-field intensity profile for a CO_2 laser is shown in Figure 3.10. The dotted line shows the profile of the input beam, the output was scanned by a simple detector in steps of 70 mils in the direction normal to the plane of Figure 3.10. Approximately 82% of the incident energy is contained within the first intensity crossings of the shaped intensity profile.

E. LASER MULTIPLEXER

Material in this section summarizes research by M.I.T. Lincoln Labs. [Ref. 20]

Veldkamp has developed a binary diffraction grating which serves to multiplex local oscillator wave fronts for use in an IR laser radar system. The phase and amplitude matching of the signal to the local oscillator wave fronts maximizes

LASER PROFILE
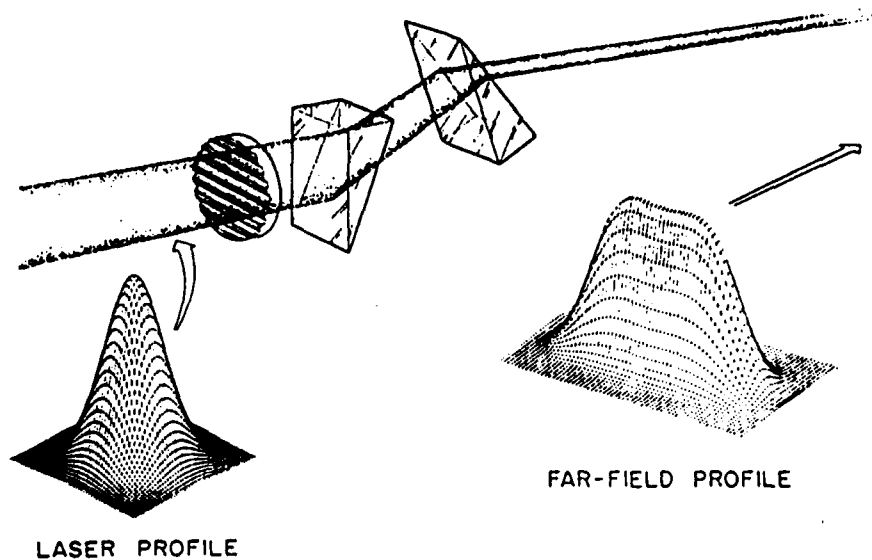
FAR-FIELD PROFILE

**Figure 3.9   Diffractive Optics Performing Laser Beam
Profile Shaping [from Ref. 13]**

---- LASER BEAM PROFILE
—— SHAPED PROFILE

$\sigma \cdot 085$
$\phi \cdot 087\pi$
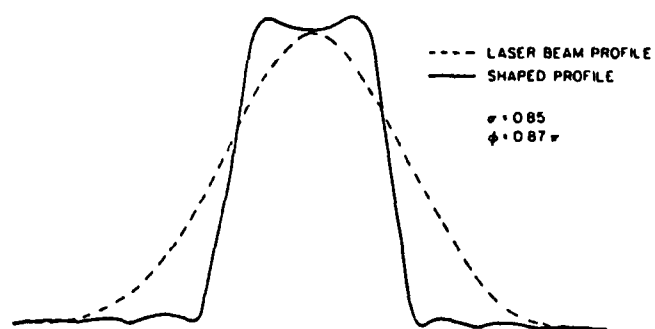
**Figure 3.10   Far-Field Intensity Profile of a TEMoo
10.6 Micron CO2 Laser with and without Beam Shaper
[from Ref. 14]**

the signal-to-noise ratio, provides the proper spatial resolution and minimizes the heat generated on the focal plane.

The holographic surface relief grating takes a uniform plane wave from a single local oscillator (LO) laser and divides the beam into N plane waves focused on each of the N elements in phase with the incoming signal (Figure 3.11). The virtual exit aperture calculated for the signal beam path is equal to the hologram size, resulting in a diffraction-limited LO amplitude distribution matched to the signal. As a result, the signal wave fronts and the LO wave fronts are spatial frequency bandwidth limited by the same low-pass filter, matching the signal precisely with the LO, resulting in diffraction-limited performance. Veldkamp believes it is
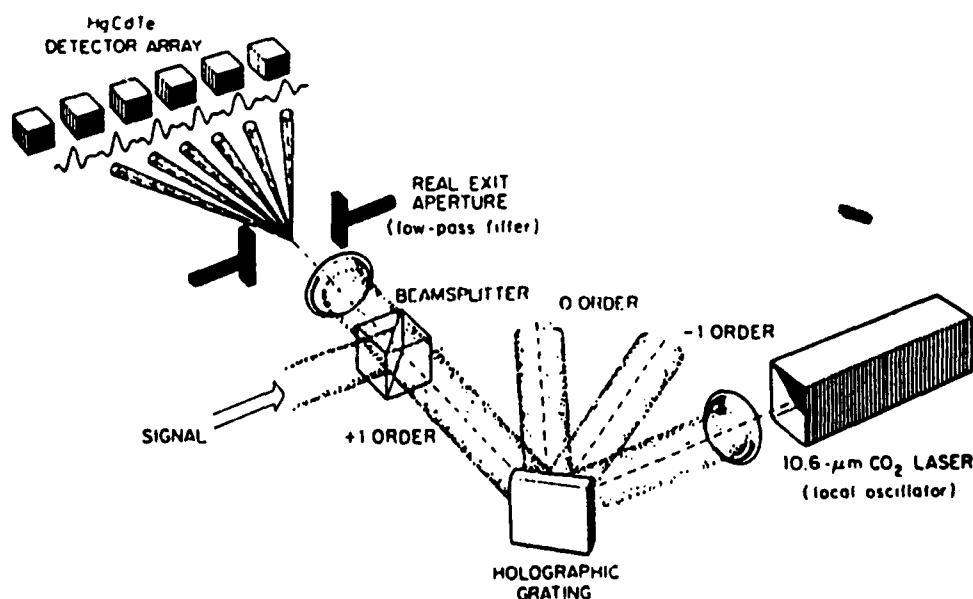
Figure 3.11 Holographic Generation of a Multibeam Local Oscillator [from Ref. 13]

41

feasible to illuminate a 100 element heterodyning detector array with LO beams from a single binary grating with reasonable power efficiency.

This beam splitter performs a similar function as the one measured in Chapter IV, but the beam splitter in this section operates in the IR vice the visible waveband.

F. SOLAR CELL CONCENTRATORS

Currently, the Strategic Defense Initiative Organization (SDIO) is working on a survivable solar power array called Super and the Air Force is working on a Survivable Concentrator Photovoltaic Array (Scopa); both will eventually be used on military satellites. The Scopa designs include a solar concentrator; the purpose of the concentrator is to increase the power output of the cell by collecting more light and to increase the solar cell's survivability against enemy attack. Although binary optics are not currently considered for the concentrator's optics, there is no reason why they could not be used to perform the required function. Survivability against lasers is made possible since now the enemy must aim an antisatellite laser along the optical axis of the concentrator to get near the cell. [Ref. 21]

The concentrating lenses focus sunlight at 25 to 100 times the normal intensity onto the cells. Concentrators are used because current and voltage in a cell increase linearly with the intensity of the sunlight that reaches them.

Concentrating the sunlight increases the power output of the cells and makes high efficiency possible. The use of concentrators results in higher temperatures in the solar cells, 75 to 100 C, which reduces efficiency. However, the gain in efficiency offsets the losses from increased temperature. Building cells to operate efficiently at those higher temperatures is still unrealized. Concentrators add weight, a critical factor in the design of space systems. The weight gain in the Scopa design is compensated by reducing the size of the solar cells; instead of using two by four centimeter cells, the new cells will be four to five millimeters in diameter. Additionally, fewer cells will be required. Another problem introduced by concentrators is the complication of designing the solar panels to track the Sun to within one degree to enable sunlight to enter along the optical axis of the concentrators; this problem remains to be explored. [Ref. 22]

Polaroid has conducted research on a solar window or microscopic compound parabolic concentrator (CPC). Polaroid's solar window is a holographic optical element (HOE) and not a binary optic; its fringe pattern is made by holographically interfering laser beams vice computer generating the pattern. It can be made transmissive selective with characteristics similar to a nonimaging CPC; it transmits the visible and near IR and reflects the longer wavelength IR. The CPC is a reflecting surface that is generated by rotating a parabola

around a central axis; it resembles a truncated paraboloid. Light enters the large end of the CPC over a fairly wide range of acceptance angles, is totally reflected within the CPC, and exits at the small end. The CPC can be made out of transparent dielectric material allowing total internal reflection at the walls in passing from one end to the other. The main advantage of the CPC is that it can track the sun over a large angle and still provide a reasonable amount of concentration; this may relax constraints on a solar panel control system for aiming the solar arrays. Polaroid has not considered this technology for space applications but there is no reason to prevent its application, but research for a suitable material is required. Polaroid has embossed microlenses of this shape into plastic from a master, demonstrating ease of manufacture and low cost. They constructed an array of lenslets with a diameter of 4 μm at the large end and tapering to 2 μm at the small end (Figure 3.12). If the space between the parabolas is either coated or filled with a highly reflective material, such as aluminum, then any long wavelength IR radiation that is incident on the embossed side will be reflected because the 2 μm opening is too small for the radiation to pass. [Ref. 23]

For space applications, further research is required to find an appropriate material suitable for use in the space environment. [Ref. 24] The space station will use deployable

44
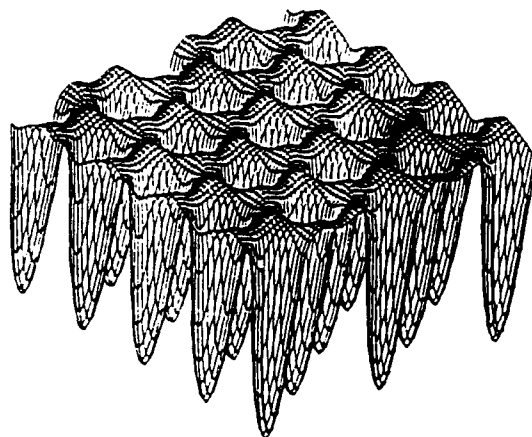
**Figure 3.12   Isometric View of Hexagonal Pattern
[from Ref. 25]**

arrays of solar cells; in the future, a roll or collapsible panel of solar concentrators could be made and attached to the outside of such solar panels to increase the efficiency. Polaroid's ability to mass produce binary optics is an extremely important achievement because it will help demonstrate the low cost as well as the next generation of lightweight optics.

G.   CURRENT INDUSTRIAL APPLICATIONS

Honeywell is currently researching the application of binary optics to ring laser gyro (RLG) readout optics, uncooled thermal imagers, helmet-mounted displays, antireflective avionics displays, and optical storage disk readout.   The RLG readout optics are for use in determining

the interference pattern from the missile's RLG, providing 25% cost reduction, a two fold improvement in signal to noise ratio, and easier assembly and alignment. The uncooled thermal imagers are using binary microlenses which provide a two-fold increase in sensitivity while reducing weight by 40%; they will be used on missile seekers and infantry night scopes. Helmet-mounted displays require lightweight optics; by using binary optics, a 25% reduction in weight, a 30% increase in the aperture, and reduced assembly and alignment costs were realized. [Ref. 26] The helmet-mounted displays currently designed are for helicopter pilots. The antireflective avionics displays use a low cost plastic replication of a binary optic (estimated cost savings of a factor of ten) and provides reduced glare thereby enhancing safety. The optical storage disk readout may be used on aircraft as well as the space shuttle and space station. [Ref. 27]

3M currently produces a diffractive bifocal intraocular lens which has been surgically implanted in patients in both the United States and Europe. The lens includes a blazed phase zone plate which directs most of the light to two diffractive orders. The combination of the diffractive and refractive surface enable the patient to have simultaneous bifocal vision, which is impossible with only conventional optics. The actual design is proprietary company information.

[Ref. 11] The diffractive lens is made using the replication procedure of embossing plastic from a master. [Ref. 28]

H. FUTURE APPLICATIONS

1. Near Term Future of Binary-Optics Technology

Veldkamp speculated on the future of binary-optics technology in the next three to five years by saying:

> Two years ago, when we felt that the technology was developed far enough to be practical, we expected that it would be accepted by the optics industry with open arms—it could solve a specific but narrow set of problems. Quite the opposite happened. We went to missile seeker optics and other systems people. Basically they said: are you crazy? These are systems that were designed ten years ago, we're not going to change the design why should we? There's no money in it. So what is slowing down the acceptance of the technology is really the inertia in captive DoD (Department of Defense) industries. If we could put in the same technology transfer effort in the commercial optics market, acceptance would go ten times faster. There's a commercial market now for bifocal interocular lenses, for binary optics in fiber communication, for deep UV (ultra-violet) systems, for landscape lenses in compact folded cameras, for flat 3-D (three dimensional) displays, and for micro-optics in CDs and VCRs (video cassette recorders). It is the commercial market that will have binary optics in place before it will appear in DoD systems on a large scale. [Ref. 1]

2. Amacronics

The following is summarized from research by M.I.T. Lincoln Labs concerning amacronics. [Ref. 1]

Amacronics is a layered structure of processing electronics, binary micro-optics, and detector arrays, with applications in imaging systems with focal plane processing.

Today's sensors use a computer system that follows a conventional optics front end, the raster scanner system, and

47

the electronic detector array. A large computer is required to handle the signal processing for the array's output which is taken in a serial manner. Similar to computer systems, all electro-optic systems suffer from a "bottleneck"; computer systems use a single central processing unit which slows down the overall system. In electro-optical systems, all the optical information goes through a detector array at the focal plane which is the bottleneck. A massive amount of information comes in and is serially carried away from the focal plane which is in a raw form not easily handled by digital computers.

Amacronic structures take advantage of parallel processing of the array output. Since processing occurs at the array, a smaller computer can be used to perform any remaining signal processing. Currently, M.I.T. Lincoln Labs is developing layered structures of optics and electronics in a parallel form (a processing unit per pixel), similar to the human retina which uses similar amacrine clustered processing layers. "Amacrine" is from the Greek **a macros** meaning short range. Hence, the idea is to couple dynamically clusters of detector arrays. Similar to the vision of diurnal insects, amacrine structures may be able to dynamically allow tradeoffs between sensitivity and resolution. Carver Mead of Caltech has built networks tuned to detect motion with the electronics distributed in a uniform way. [Ref. 1] With binary optics, it may be possible to build systems with peripheral vision

48

much more motion sensitive than an on-axis fovial view, or systems tuned for edge detection or noise reduction. Dynamic control of detector arrays is the goal of amacronics.

Military and space systems should see increased use of binary optics because they can save weight and improve performance of systems. In general, military applications will find increased use of binary optics because of their versatility and ability to accomplish what conventional lenses cannot do.

I. ADVANTAGES AND COST

1. Advantages of Binary Optics

Binary optics can perform tasks that conventional optics cannot. One of the major advantages of binary optics is its adaptability to an optical system; the optic can be made in an arbitrary shape and be designed to yield the desired wave front while allowing very compact sensor designs. Additionally, using diffractive elements may reduce the number of required elements by 25 to 33 percent. [Ref. 29]

2. The Cost Issue

A common claim is that binary optics are low cost. However, the cost issue is yet to be fully proved. [Ref. 27] 3M and Polaroid have demonstrated the ability to emboss lenses in plastic from a master; if the lenses are produced in quantity, then the embossing technology is critical to low-cost optics as well as lightweight optics. If only a single

lens is to be produced, it is not clear if there is a cost advantage to using binary optics. However, if the system requires micro-optics (i.e., ten millimeters (mm) or smaller) in mass quantities or if quantities of at least 100 are planned for an equivalent system using binary optics, then binary optics should prove more economical and in some cases yield better performance. [Ref. 30]

IV. NEAR-ANGLE SCATTERING MEASUREMENTS

Near-angle scattering is the light scattered less than one degree from the main beam. In optical systems, near-angle scatter degrades the image contrast, especially near bright sources or dark objects against bright backgrounds. [Ref. 31] As mentioned in Chapter I, the scattering measurements give a qualitative indication of fabrication errors and manu-facturing limitations. Knowing the amount of scatter from an optic indicates how well the optic will perform in the system. In the next chapter, the scattering measurements are compared to a scalar theory which is developed and modeled an a personal computer.

The near-angle scattering from the specular transmitted beams of a binary optic beam splitter (transmissive optic with no focusing power) designed and manufactured by M.I.T. Lincoln Labs was measured. The optic used had known manufacturing defects (i.e., it was etched to an improper depth), and time constraints precluded obtaining a better specimen. The binary optic was designed to be a helium neon (HeNe) laser multiplexer, dividing a laser beam into seven separate equal intensity coherent beams (Figure 4.1). Because the binary optic was etched too deeply, the seven beams were not equal in intensity. The main lobe had slightly lower intensity than the first, second, and third lobes. Theoretical limitations
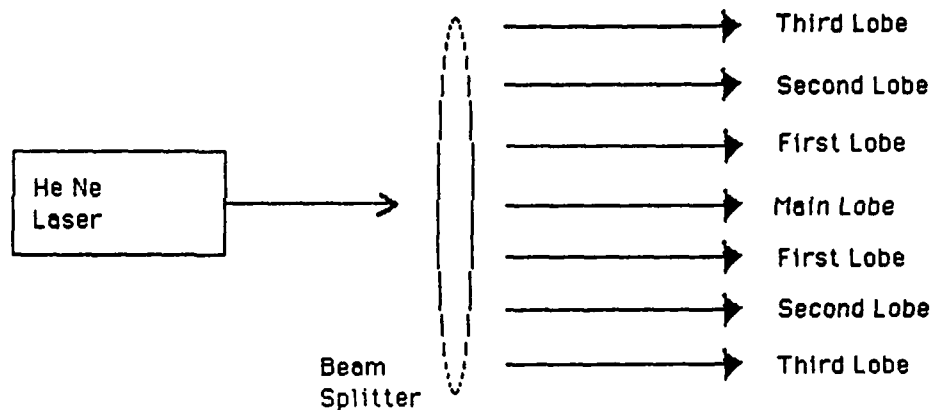
```
                                    ─────────────────▶  Third Lobe

                                    ─────────────────▶  Second Lobe

                                    ─────────────────▶  First Lobe

    ┌──────────┐                    ─────────────────▶  Main Lobe
    │ He Ne    │ ──────────▶
    │ Laser    │                    ─────────────────▶  First Lobe
    └──────────┘
                                    ─────────────────▶  Second Lobe

              Beam                  ─────────────────▶  Third Lobe
              Splitter
```

Figure 4.1   Beam Splitter made by M.I.T. Lincoln Labs

prevent the manufacture of an optic with only seven orders, hence unwanted orders will always be present.   [Ref. 32]

A.   NEAR-ANGLE SCATTER INSTRUMENT

The instrument used to measure the near-angle scatter was designed by Douglas W. Ricks at the Naval Weapons Center at China Lake, California [Ref. 4].   A top view of the instrument is shown in Figure 4.2.   The instrument is capable of measuring scattered light from one degree to a few ten thousandths of a degree from the main transmitted beam. Scatter measurements at extremely small angles are possible because the detector is scanned through the specular beam which can then be subtracted from the scatter measurements (i.e., the background level may be subtracted from the
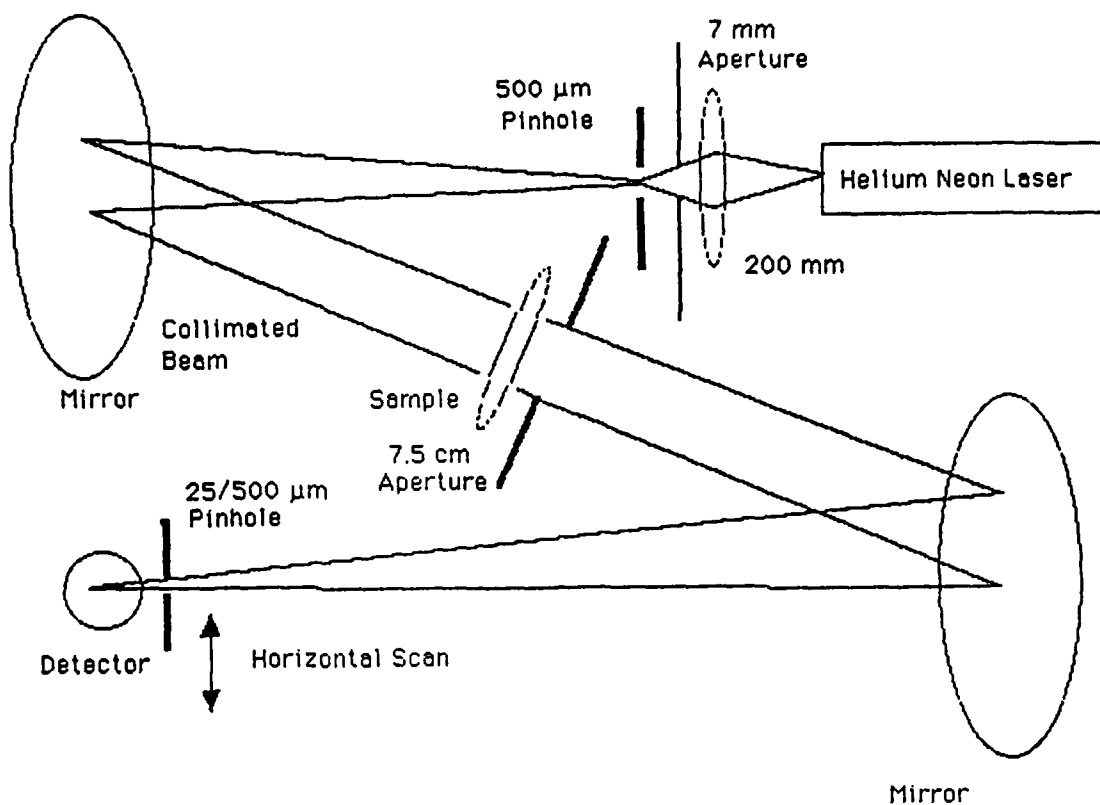
**Figure 4.2   Near-Angle Scatter Instrument
(Top View) [Ref. 31]**

measurement). Small angular measurements are possible since
the mirror has a long focal length and a very small horizontal
scan distance (in the plane of Figure 4.2) is used for the
detector.

$$\beta \approx \frac{d}{f_m} \qquad\qquad (4.1)$$

where

β = angle from the specular beam,
d = horizontal scan distance, and
f_m = focal length of the mirror.

By substituting d = 0.0002 in and f_m = 71.6 in into Equation 4.1, the angle β representing the best angular resolution of the system is:

$$\left[\frac{0.0002 \text{ in}}{71.6 \text{ in}}\right] = 2.8 \text{ } \mu\text{radians} \qquad (4.2)$$

Equation 4.2 assumes the sample has no focusing power.

Additionally, the instrument is capable of measuring power down to eight or nine orders of magnitude from the peak of the transmitted specular beam. This is made possible by using a moderately high power laser, a sensitive detector, by eliminating stray light, by reducing the odd order aberrations through symmetry, and by carefully controlling the effects of diffraction.

Lens samples are placed in one of two positions depending on whether the sample has a focal length. Figure 4.2 shows that a sample with no focal length is placed in the collimated beam between the mirrors. The binary optic beam splitter which was measured had no focal length, therefore the configuration of Figure 4.2 was used. If the sample is a lens with a focal length then it is placed after the mirror as shown in Figure 4.3 and the detector assembly is located at the combined effective focal length for the mirror and the sample. (The mirror shortens the effective focal length of the sample.)

A Spectra-Physics Stabilite model 124A HeNe laser, operating at 632.8 nanometer (nm) was the source. Following
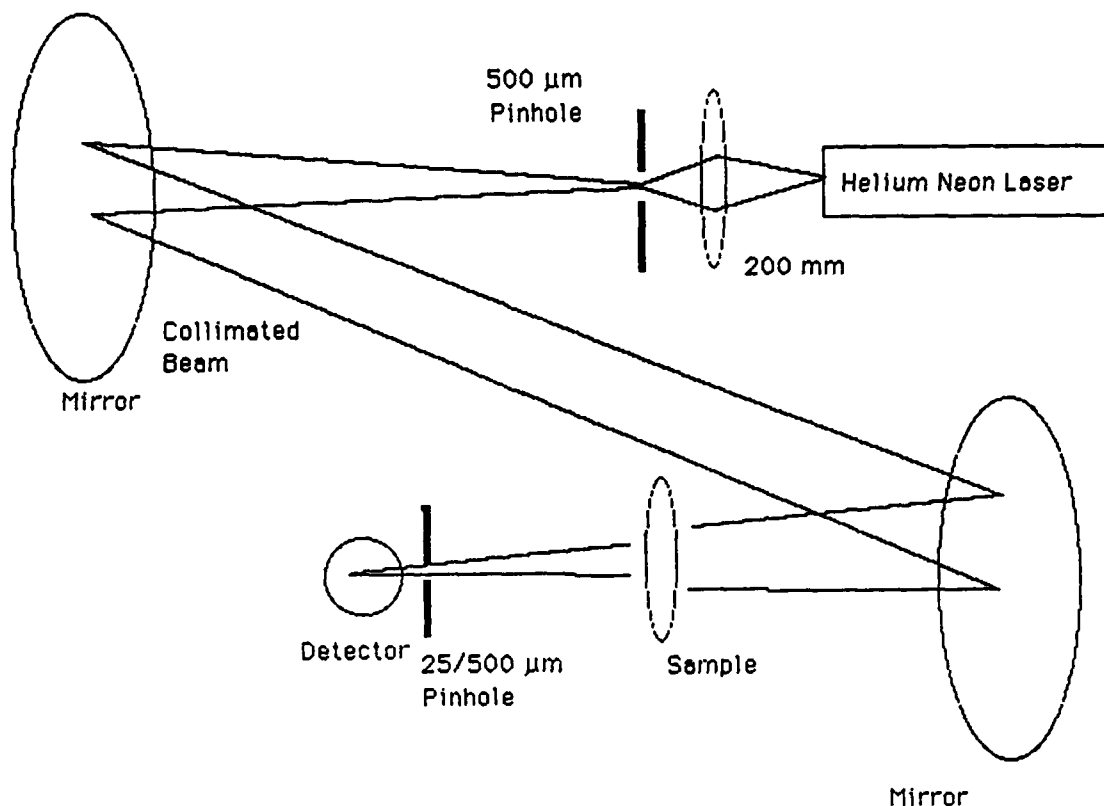
**Figure 4.3   Near-Angle Scatter Measurement for Sample
with Focal Length (Top View)**

the laser is a plano-convex lens (convex side facing laser)
with a 200 mm focal length.   The ratio of the focal length of
the mirror to the focal length of the lens determines the
expansion of the laser beam.   A large aperture of 7 mm on a
15 by 15 centimeter (cm) plate was used following the 200 mm
lens in order to eliminate stray light between the laser and
the first mirror which is reflected by the optical bench and
other surfaces.   A small aperture, 500 μm, is placed at the
common focus of the mirror and the plano-convex lens.   The
pinhole is approximately three or four times larger than the

focused beam at the 1/e points to avoid diffraction effects. (Each mirror and lens is at least four times the beam diameter in this apparatus.) The spherical mirrors are twins, each has a focal length of 71.6 in (1.82 m) and is approximately 12 in in diameter.

The first mirror is placed to give the optimum collimation in the horizontal plane. The angle of incidence for the laser beam on each mirror must be the same in order to cancel the coma introduced by the spherical mirrors. Degradation occurs from spherical aberrations but is minimized by the long focal length of the plano-convex lens and mirrors. Since the spherical mirrors are used off-axis, astigmatism is introduced in the vertical plane. The astigmatism does not affect the system's horizontal resolution (i.e., the direction of scan is unaffected by astigmatism). Although astigmatism could be completely eliminated by the use of off-axis paraboloid mirrors, they are costly and difficult to align. Normally, if the sample has no focal length it is positioned in the collimated beam between the two mirrors. A large aperture of 7.5 cm on a 50 by 50 cm plate was used after the sample to block all stray light between the two mirrors. The binary optic holder actually blocks stray light as close as one half inch from the center of the binary optic.

A pinhole is placed at the best focus in the horizontal plane of the second mirror. The silicon detector, made by Newport Corporation, is connected to their laser pico-watt

digital power meter, model 835. A 633 nm narrow-band filter is used in front of the detector; the filter has a transmittance of 57% at 632.8 nm and is used to block out ambient light. Translation stages with 0.0002 in resolution are used to position the pinhole and detector assembly at the focus. The pinhole and detector are simultaneously scanned in the horizontal plane to measure the scattered light from the sample. [Ref. 31]

Laboratory air currents and temperature gradients can cause angular beam deflections comparable to the resolution of the instrument, so most of the instrument was enclosed in a Plexiglas enclosure. [Ref. 33] Two small windows were cut into the enclosure to permit the laser beam to enter unimpeded and to allow the experimenter to operate the micrometers on the translation stage. The laser was located outside the enclosure in order to isolate the heat generated from the laser with the instrument.

The size of the pinhole in front of the detector involves a tradeoff between angular resolution and intensity available for the measurement. In other words, a small pinhole has excellent angular resolution but does not admit as much light so it has a lower signal-to-noise ratio than a larger pinhole. However, the small pinhole admits less stray scattered light and permits measurements at small angles. More than one size pinhole can be used to get a broader angular range of scatter information for a particular sample.

The instrument is optimized for an optic with no focusing power (i.e., the transmitted light is collimated). If the sample has a focal length, the configuration for the instrument in Figure 4.3 has less angular resolution. Additionally, the incoming beam to the sample is not collimated, and the focal plane becomes three dimensional which degrades results. A circular scan stage for the detector could compensate for this effect.

B. PROCEDURE USED FOR MEASUREMENTS

The actual beam splitter pattern is depicted in Figure 4.4. From Figure 4.4, it is evident that the pattern is symmetrical; therefore, only four of the seven main orders were measured.

The procedure to make measurements is relatively straight forward. First, a set of readings was taken without the sample in position using a particular size pinhole in front of the detector. These readings form the background readings which account for all the scattered light from the instrument
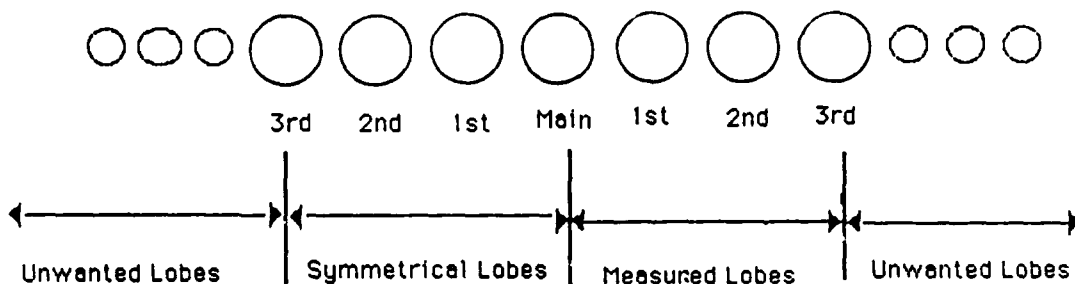

Figure 4.4 Actual Beam Splitter Pattern

58

and surroundings. Next, the sample was positioned and the measurements were repeated. The micrometer was moved the same distance relative to the respective peak; the angles are calculated by taking the arctan of the horizontal scan distance divided by the focal length.

A lens with a focal length has less angular sensitivity since the effective focal length of the lens and mirror must now be used. The effective focal length is approximately equal to:

$$\frac{1}{f_{eff}} \approx \frac{1}{f_1} + \frac{1}{f_2} + \frac{d}{f_1 f_2} \tag{4.3}$$

where

    d   = distance from mirror to lens,
    f_1 = focal length of the mirror,
    f_2 = focal length of lens sample, and
    f_{eff} = effective focal length of mirror and lens combination.
          The effective focal length is always less than the
          focal length of the lens.

C. SCATTERING MEASUREMENTS

The data is presented in plots using a log-log scale because the scattered light varies over nine orders of magnitude. The lines on the graphs merely connect the data points.

The abscissa has units of log sine angle of the scattered light in radians from the specular incident beam which is normal to the optic. Proceeding on the graphs from left to right, the angles become larger further away from the specular (nonscattered) beam. For very small angles, the sine of an

angle is the same as the tangent of that angle. Since near-angle scattering deals with angles less than one degree from the specular beam, the small angle approximation for the sine of the angle equalling the angle can be used. To illustrate the angular range of the instrument, consider the graph in Figure 4.5. The angular range is $10^{-5.6} < \beta < 10^{-2.0}$ radians which corresponds to $0.00014 < \beta < 0.573$ degrees. Each beam starts with the specular beam as zero reference for the angular measurements.

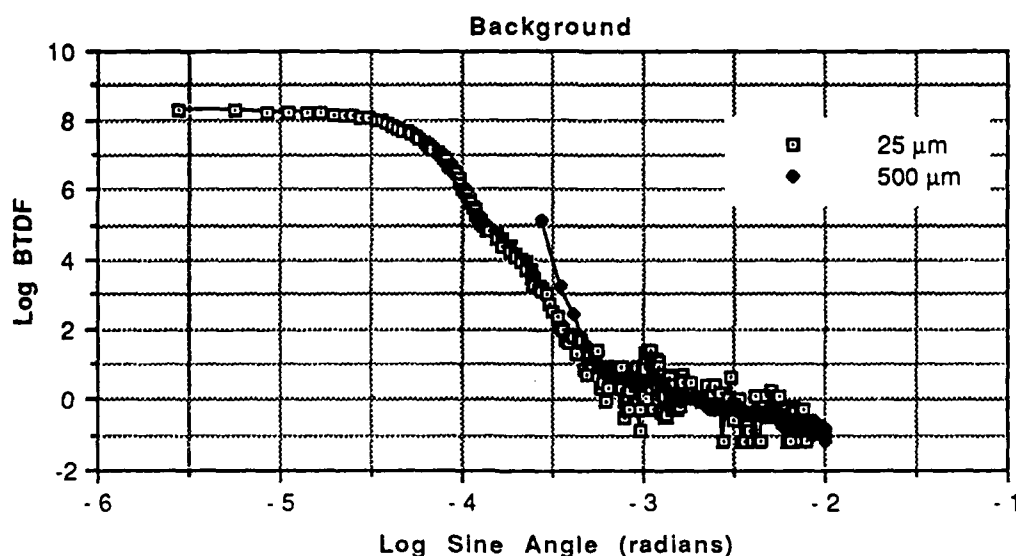**Figure 4.5 Background Measurements for 25 and 500 μm Pinholes**

The term Bidirectional Transmission Distribution Function (BTDF) was invented by Edwards and is universally used by professionals [Ref. 34]. The bidirectionality arises from the

incidence and exitance directions [Ref. 35]. Exitance is the radiant flux density of a wave field leaving a surface at a normal direction. The ordinate is in terms of the log of the BTDF, which has units of 1/steradian. The BTDF is:

$$BTDF = \frac{P_{scat}(\beta)}{P_{in}} \qquad (4.4)$$

where

$P_{scat}(\beta)$ = power scattered as a function of β per solid angle in steradians (sr),
β = scattering angle from the specular beam, and
P_{in} = power incident on the optic, which is constant.

The solid angle Ω subtended by the detector as seen by the scattering test optic is given by:

$$\Omega = \frac{A_p}{[f_m]^2} \qquad (4.5)$$

where

A_p = area of detector pinhole, and
f_m = focal length of mirror (for test optic with no focusing power).

If $P_{det}(\beta)$ is the power scattered through the detector at angle β then

$$P_{scat}(\beta) = \frac{P_{det}(\beta)}{\Omega} \qquad (4.6)$$

Substituting into Equation 4.4, the BTDF is:

$$BTDF = \frac{[f_m]^2}{A_p}\left[\frac{P_{det}(\beta)}{P_{in}}\right] \qquad (4.7)$$

To illustrate the calculation of the BTDF, values from the experiment are substituted into Equation 4.7:

61

$$BTDF = \frac{(1.82 \text{ m})^2}{\pi \left(\frac{25 \text{ μm}}{2}\right)^2} \left(\frac{0.26 \text{ mW}}{6.3 \text{ mW}}\right)$$

$$(4.8)$$

$$BTDF \approx 2.8 * 10^8 \qquad\qquad (4.9)$$

$$\text{Log}(BTDF) = 8.4 \qquad\qquad (4.10)$$

The 25 μm and 500 μm pinholes were measured and verified to be the proper size using a differential interference contrast (Nomarski) microscope.

To adjust data for displaying two different size pinholes on the same graph, the respective BTDFs are set equal to each other:

$$\frac{P_{500}}{P_{in}} \left[\frac{f_m^2}{A_{500}}\right] = \frac{P_{25}}{P_{in}} \left[\frac{f_m^2}{A_{25}}\right] \qquad\qquad (4.11)$$

Isolating P_{25} in Equation 4.11 yields:

$$P_{25} = \left[\frac{A_{25}}{A_{500}}\right] P_{500} \qquad\qquad (4.12)$$

where

P_{500} = power readings for 500 μm pinhole,
P_{25} = power readings for 25 μm pinhole,
A_{500} = area of 500 μm pinhole, and
A_{25} = area of 25 μm pinhole.

The results show that P_{500} is multiplied by A_{25}/A_{500}.

1. Background Measurements

The background measurements without the sample present are shown in Figures 4.5 and 4.6. An expanded view of $10^{-3.5}$ to 10^{-2} radians is shown in Figure 4.6 where it is evident that
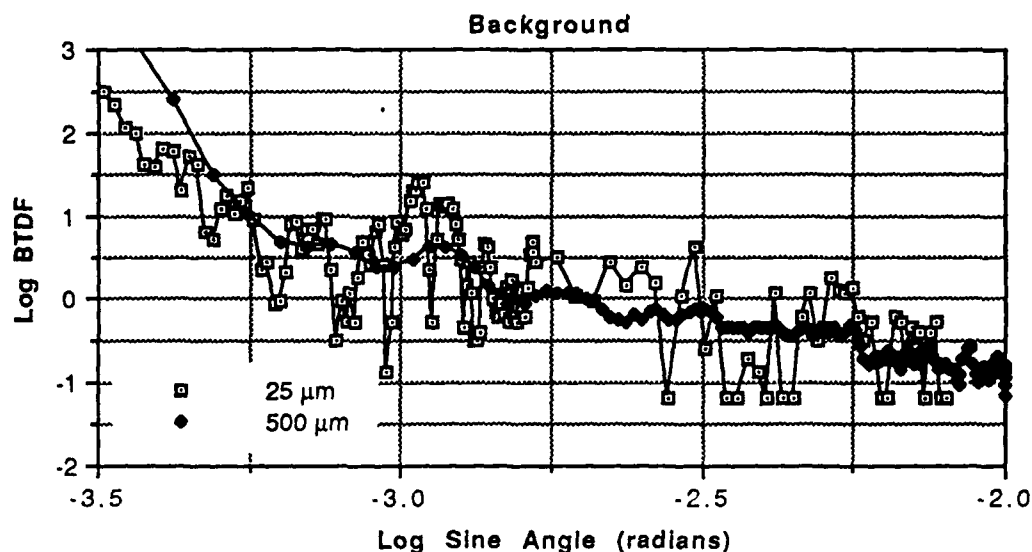
Figure 4.6 Expanded View of Background Measurements

the larger pinhole tends to average the readings. The range of the instrument from Figure 4.5 is slightly more than nine orders of magnitude for the 25 μm pinhole and six orders of magnitude for the 500 μm pinhole. The data for the larger pinhole starts at $10^{-3.6}$ radians because a larger pinhole lets in so much light that the detector saturated for an unimpeded specular beam (i.e., background measurements). The larger pinhole lacks angular resolution closer to the specular beam since the detector views a larger area and thereby tends to average light over a larger area. Two sizes of pinholes provide better information. The larger pinhole gives averaged reading further from the specular beam, and should have a larger signal-to-noise ratio for low scattering levels.

63

Background measurements are presented to indicate the angular range in which the background may be considered insignificant. If insignificant is defined as three orders of magnitude from the specular peak, then readings for angles greater than or equal to 10^{-4} radians can be considered to have little influence by the background, whereas readings in the angular range from 10^{-5} to 10^{-4} radians would be influenced by the background. One may choose a less or more stringent definition for insignificant levels of background. Background measurements should be compared to measurements of the scattering test optic. If the relative background scatter is nearly equal to or greater than the relative scattering from the optic being tested for scatter, then the background scatter is significant. If the relative scattering at some angle *from the optic under test* is much greater than the relative background scattering at that angle then the background scattering is insignificant. There is no standard.

2. Main, First, Second, and Third Lobes

The experimentally measured main, first, second, and third lobes are depicted in Figures 4.7 through 4.14. Figures 4.8, 4.10, 4.12, and 4.14 are expanded views of the respective lobes at larger angles. Readings for each lobe start to increase at the larger angles since light is received from the adjacent beam (see Figure 4.4). Again, the 500 μm pinhole averages the readings and the same conditions noted with the background readings occur. The background and beams were

64

Beam Splitter Main Lobe
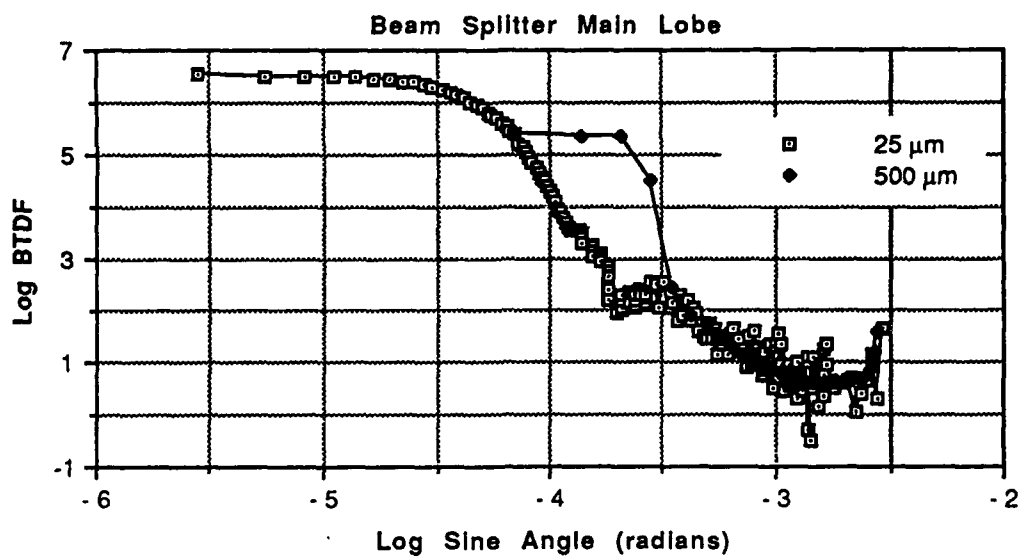
Figure 4.7   Main Lobe Measurements for 25 and
500 μm Pinholes

Beam Splitter Main Lobe
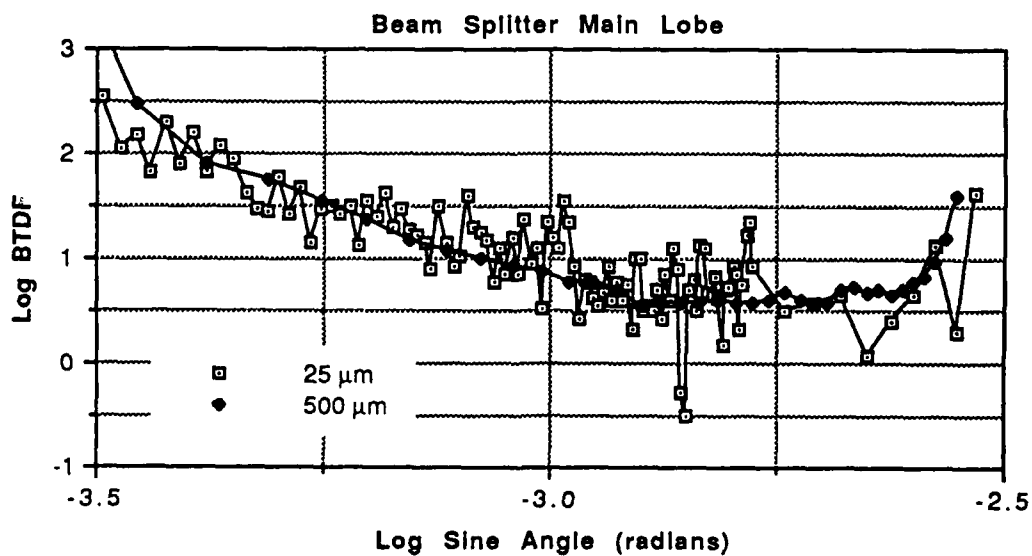
Figure 4.8   Expanded View of Main Lobe

65
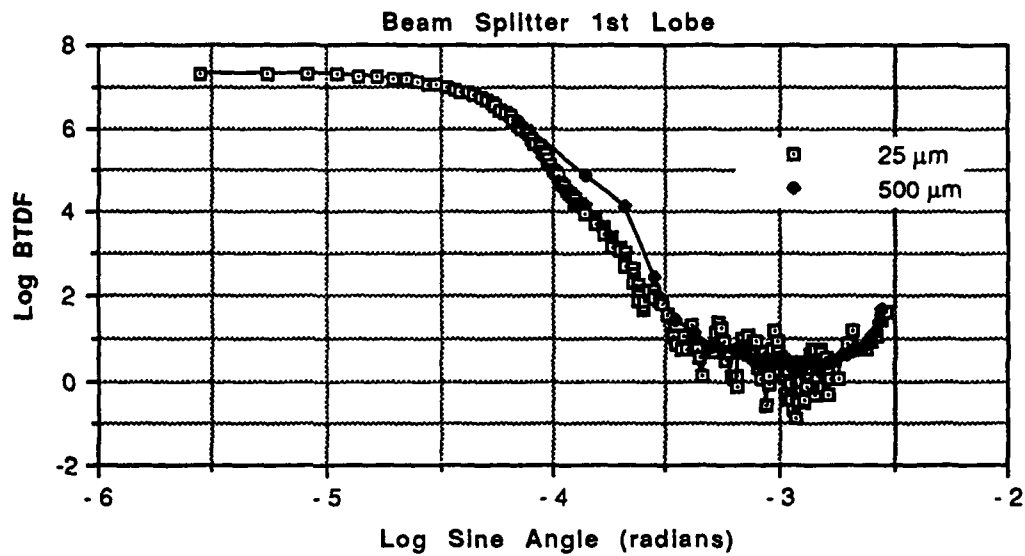
Figure 4.9   First Lobe Measurements for 25 and 500 μm Pinholes
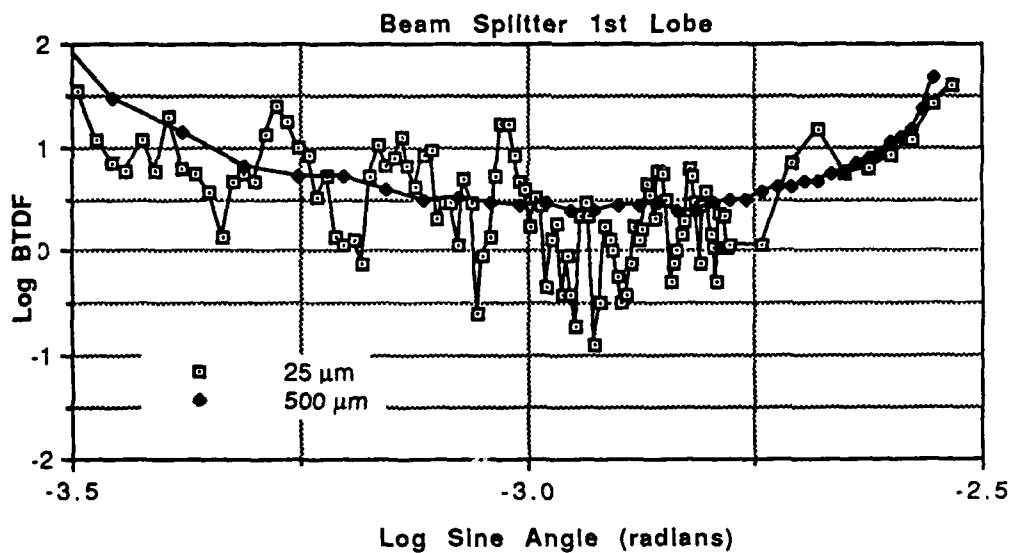
Figure 4.10   Expanded View of First Lobe

66

Beam Splitter 2nd Lobe
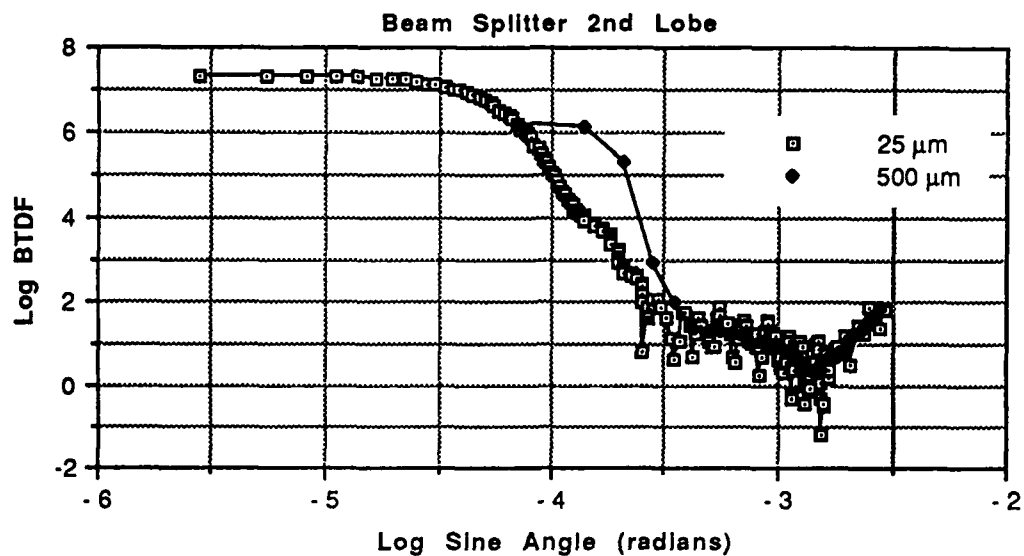
Figure 4.11   Second Lobe Measurements for 25 and 500 μm Pinholes

Beam Splitter 2nd Lobe

Figure 4.12   Expanded View of Second Lobe

67

Figure 4.13   Third Lobe Measurements for 25 and 500 μm Pinholes
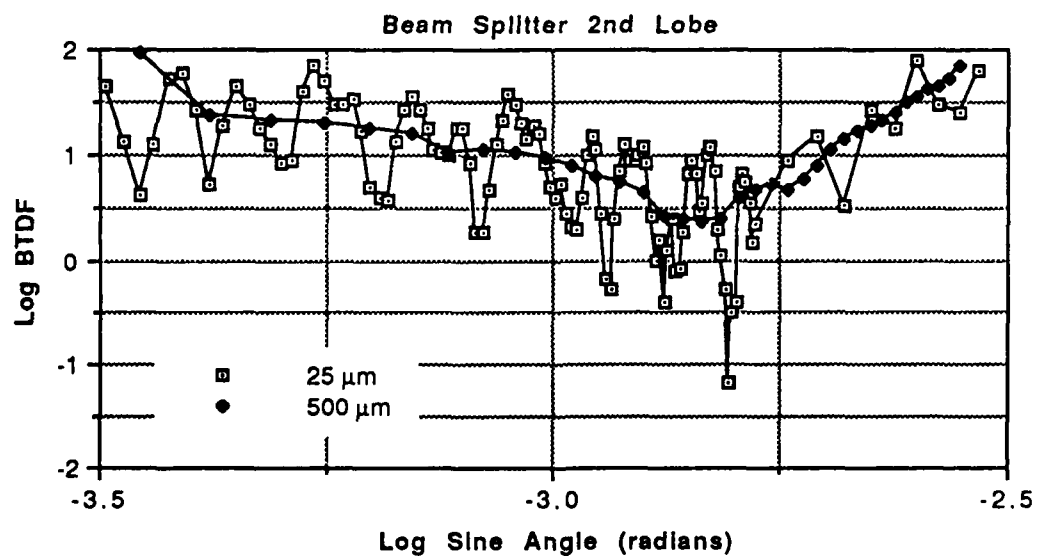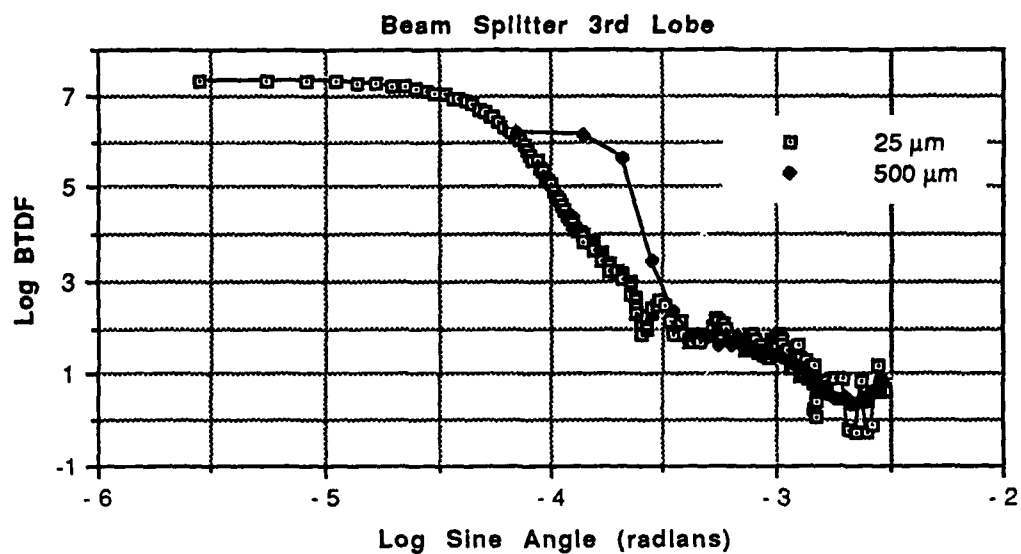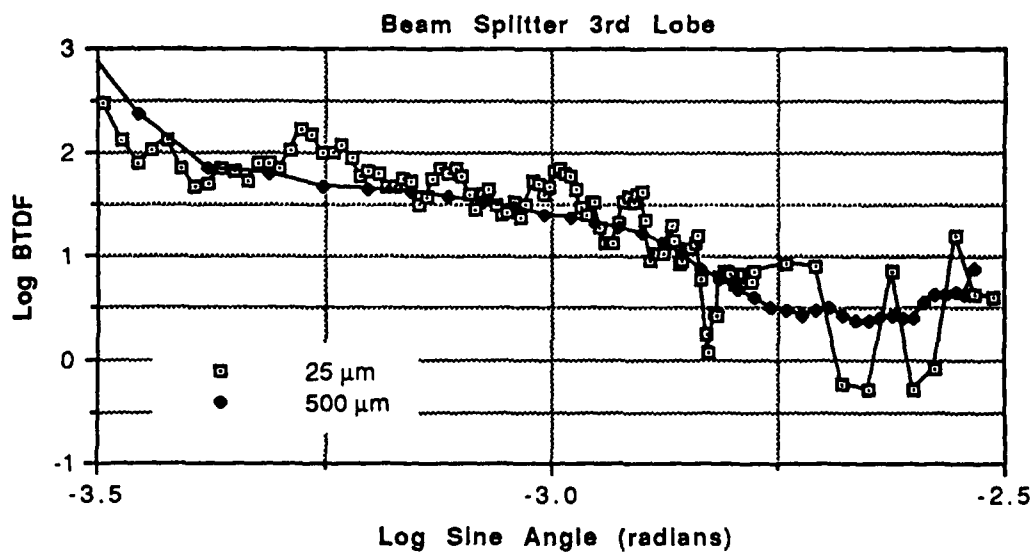

Figure 4.14   Expanded View of Third Lobe

68

measured by moving the micrometer 0.0002 in for 100 data points, 0.001 in for 100 data points, and then 0.01 in for the remaining data points (approximately 25 to 100 additional points). The detector stage was moved in 0.005 in increments for the 500 μm pinhole instead of the smaller increments used previously (i.e., 0.0002, 0.001, and 0.01 in); approximately 75 data points were obtained. Fewer data points are required for the larger pinhole since the readings do not change significantly with small horizontal detector movement.

a. Main Lobe

The measurements for the main beam in Figure 4.7 show the range of the measurement as approximately six orders of magnitude; the range is smaller than the background due to the scattering which dominates at larger angles. The background shows a range of about eight or nine orders of magnitude, indicating approximately two orders of pure scatter in the main lobe. The power in the beam measured for the background is now divided into the separate lobes (see Figure 4.4) and the specular power level is reduced. A small increase in the 25 μm readings for angles greater than or equal to $10^{-3.75}$ radians is evident in Figure 4.7 (i.e., the slope does not have a gradual decrease as does the background in Figure 4.5); the irregularity in the slope is probably associated with a manufacturing defect. As mentioned earlier the main beam is of slightly lower intensity than the first, second, and third lobes which is attributed to the improper

etch depth. The upward trend at $10^{-2.5}$ radians is due to the received power from the adjacent first lobe (see Figure 4.4).

b. First Lobe

The measurements for the first lobe in Figure 4.9 show the range of the measurement as approximately seven orders of magnitude. As before, greater resolution is obtained with the smaller pinhole and the larger pinhole averages the readings. The data closely follows the shape of the background reading indicating good performance. The background shows a range of about eight or nine orders of magnitude, indicating one or two orders of pure scatter in the first lobe. Power from the adjacent second lobe is detected at $10^{-2.5}$ radians producing an upward trend.

c. Second Lobe

In Figure 4.11, the second lobe displays characteristics similar to the main lobe. Slightly less range is seen when compared to the first lobe, approximately 6.5 orders of magnitude vice 7. The background shows a range of about eight or nine orders of magnitude, indicating approximately two orders of pure scatter in the second lobe. The intensity does not fall off as smoothly as the background (see Figure 4.5). Manufacturing defects are probably responsible for the increase in intensity after $10^{-3.5}$ radians. The upward trend at $10^{-2.5}$ radians is from received power in the third lobe.

70

d. Third Lobe

The third lobe measurement, Figure 4.13, displays similar behavior to the main and second lobes. The range is 6.5 orders of magnitude for the 25 μm pinhole. The background shows a range of about eight or nine orders of magnitude, indicating approximately two and a half orders of pure scatter in the third lobe. Again, an increase in intensity is observed for angles greater than $10^{-3.6}$ radians probably due to manufacturing defects. The intensity does not rise as much at larger angles since the next adjacent lobe is an unwanted lobe (see Figure 4.4).

V. SCATTERING THEORY FOR BINARY OPTICS

A scalar scattering theory for binary optics was originated by J. Merle Elson at the Naval Weapons Center, China Lake, California [Ref. 36]. The author collaborated with Elson in developing the theory; the author modeled the theory using a personal computer and compared the theory with the measurements from Chapter IV. This relatively simple theory was modeled using Microsoft FORTRAN and run on an IBM compatible personal computer. The scalar theory for binary optics yields approximate results; exact results require a full EM theory which considers boundary conditions and the polarization of the light. More accurate results are computer time-intensive, costing thousands of dollars to run a simulation. Additionally, the complexity of programming or running an existing program has increased by several orders of magnitude. For these reasons, a scalar scattering theory is a more attractive alternative.

The scalar scattering theory developed considers scattering from two types of surface topography. Scattering is produced from surface roughness (micro-irregularities) and large scale surface features (i.e., binary step pattern). The micro-roughness is assumed to be generated by a random process and the binary surface profile is assumed to be deterministic.

The theoretical model developed is compared with experimental near-angle scattering measurements from Chapter IV.

A. SURFACE ROUGHNESS MEASUREMENTS

Surface roughness may be measured by using an instrument that gives a surface profile by either one of two methods. One method involves contact with the sample and the other does not. The contact method uses a probe which contacts the surface and follows height variations as either it or the surface is translated. The noncontact method uses optical interferometry techniques to measure surface height variations. Advantages and disadvantages exist for both methods and are thoroughly discussed in Reference 37.

A contact method using a Talystep instrument was used to measure the roughness of the binary optic. The Talystep uses a diamond styles probe that touches the surface. Talystep measurements were performed by Jean Bennett at the Naval Weapons Center, China Lake, California. Figures 5.1 and 5.2 show the Talystep profile of the binary optic measured. The average height of the optic is 6554 angstrom (Å) and the period is 200 μm. A small defect is observable in one of the trailing edges of the binary optic and is more evident in Figure 5.2. The Talystep can measure roughness less than 1 Å root mean square (rms) on polished surfaces. [Ref. 37] The
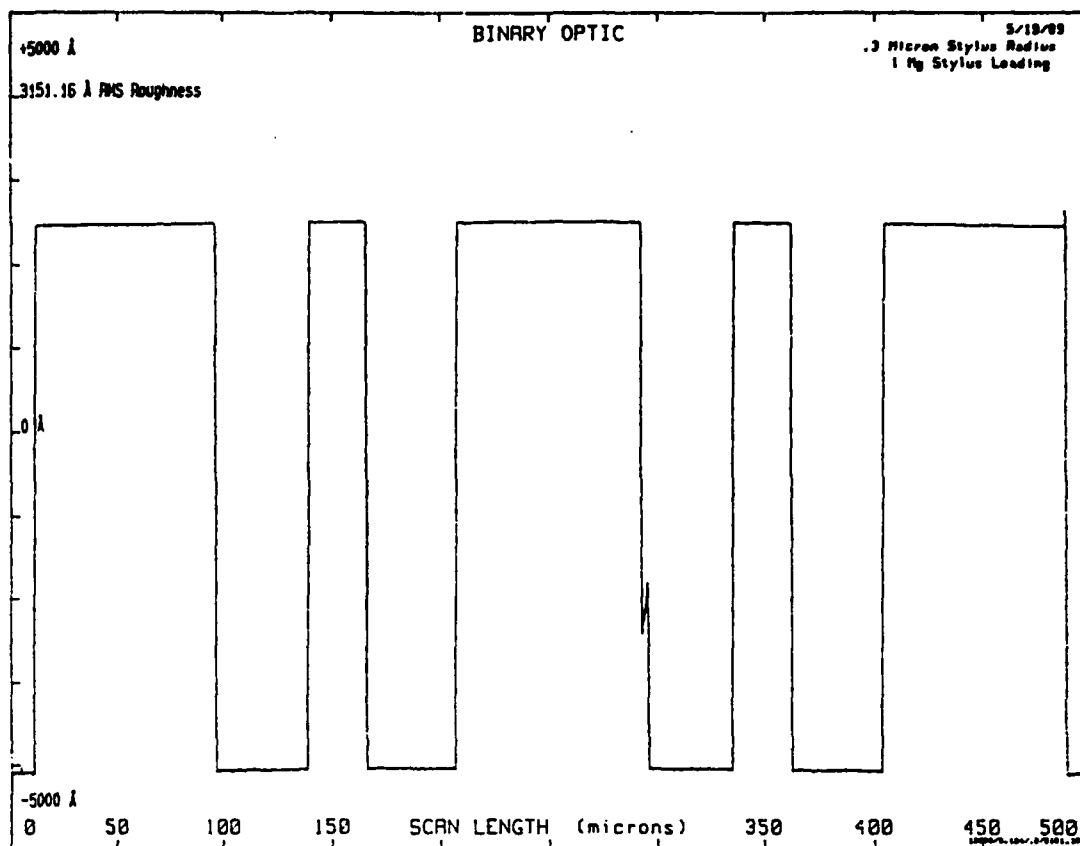
73

Figure 5.1   Talystep Profile of Binary Optic
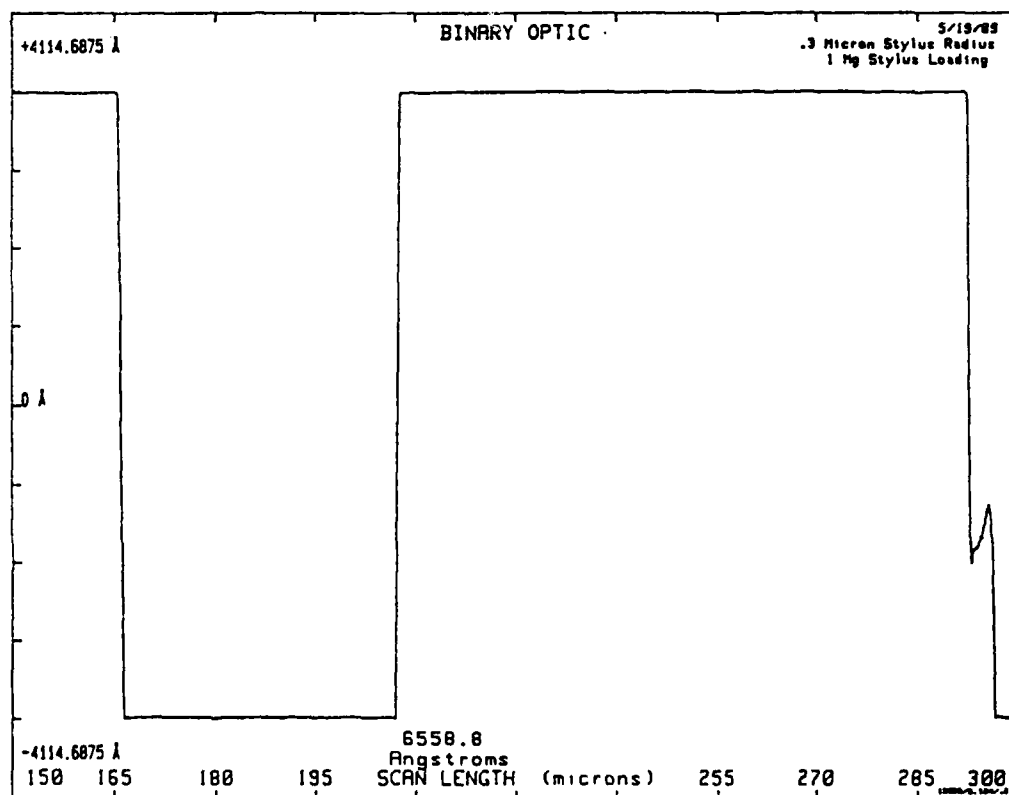
Figure 5.2   Enlarged Talystep Profile of Binary Optic

horizontal resolution of the Talystep is determined by the diameter of the stylus (0.6 μm for the measurements in this chapter).

Figures 5.3 and 5.4 show the roughness of the top and bottom of a groove measured using the Talystep. In Figures 5.3 and 5.4, 3.5 Å roughness was measured on the top and 4 Å roughness was measured on the bottom. The binary optic was made using reactive ion etching which produced an extremely smooth surface.

The instrument noise for the Talystep was 0.5 Å rms. Figure 5.1 used 13,098 points on a 500 μm profile with a 0.0382 μm sampling interval. The profile length for the groove top was 70 μm and the bottom was 30 μm.

The autocovariance function is a measure of the correlation properties of the random surface roughness. It is the product of two "copies" of the same surface profile where one copy is shifted relative to the other. The amount of lateral shift between the two copies is called the lag length. A large (small) value of the autocovariance function indicates that the random surface roughness is statistically correlated over larger (smaller) lag lengths. In other words, a large value of the autocovariance function indicates that one "copy" is a good approximation for the other "copy" for that particular lag length. The value for zero lag length is important because it equals the square of the rms roughness of the profile. The correlation length may be defined as the
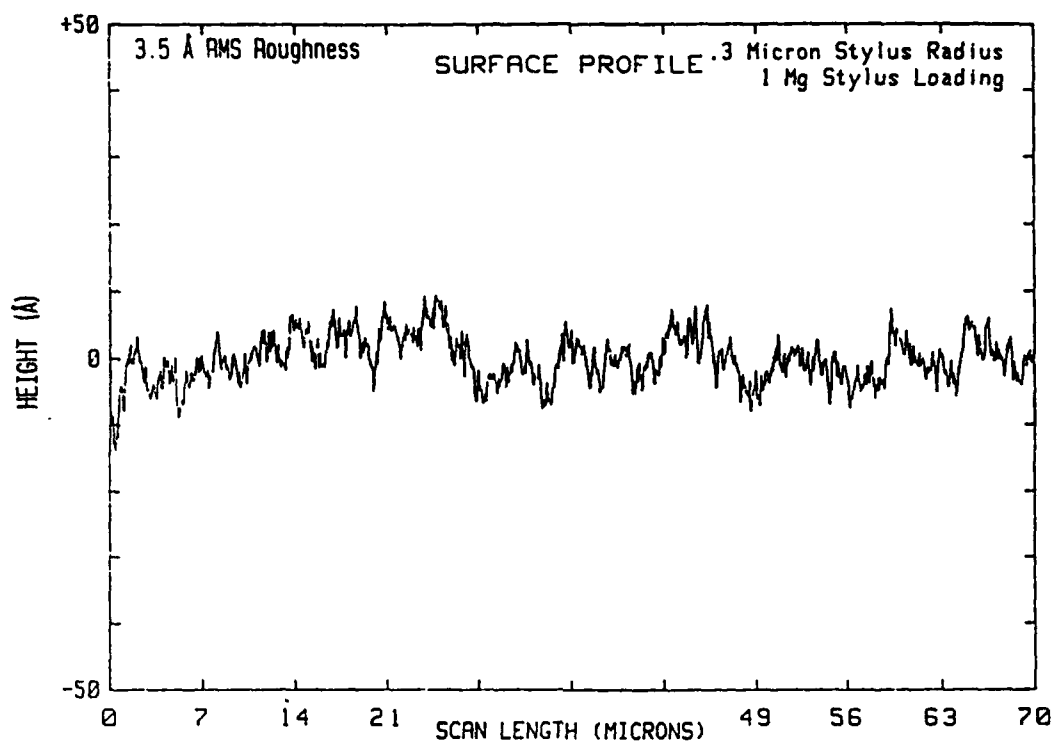
Figure 5.3   Groove Top Surface Roughness
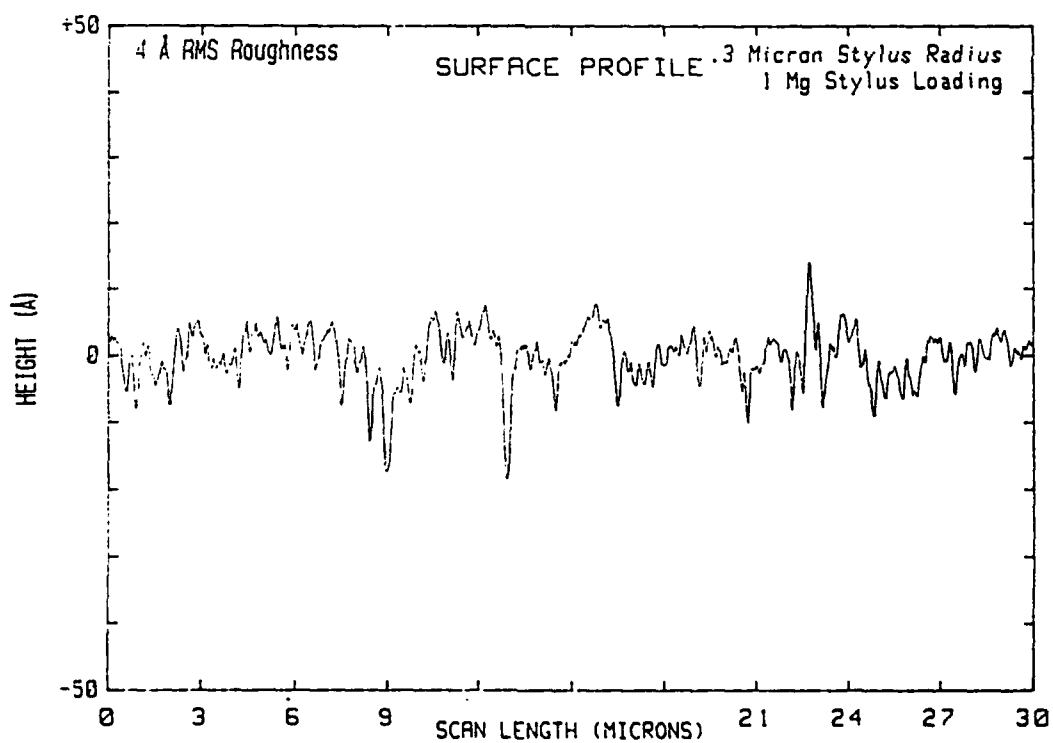
Figure 5.4   Groove Bottom Surface Roughness

76

value at which the autocovariance function drops to 1/e (0.368) of its value at zero lag. Alternate definitions use 1/10 of the value at zero lag, or where it first becomes zero. The autocorrelation function is sometimes used instead of the autocovariance function. The autocorrelation function is normalized to have a value of unity for zero lag length and is dimensionless. [Ref. 37]

From the Talystep data, the autocovariance function was computed to verify the form of function assumed for the autocorrelation function. Since the autocovariance function is normalized to one, it is the same as the autocorrelation function. Figures 5.5 and 5.6 show the average autocovariance for the top and bottom of the grooves.

An exponential autocorrelation function is a traditional assumption that appears to give good results in many cases. Unfortunately, the autocorrelation length from the Talystep can be misleading due to the short length of the scan run. Near-angle scatter is primarily concerned with long autocorrelation lengths on the surface; therefore, a long scan run for the Talystep is desirable. Previous measurements made by Wyco Corporation on this binary optic using a Wyco profilometer which uses optical interferometry techniques, yielded autocorrelation lengths ranging from 1 μm to 1,000 μm. [Ref. 38]
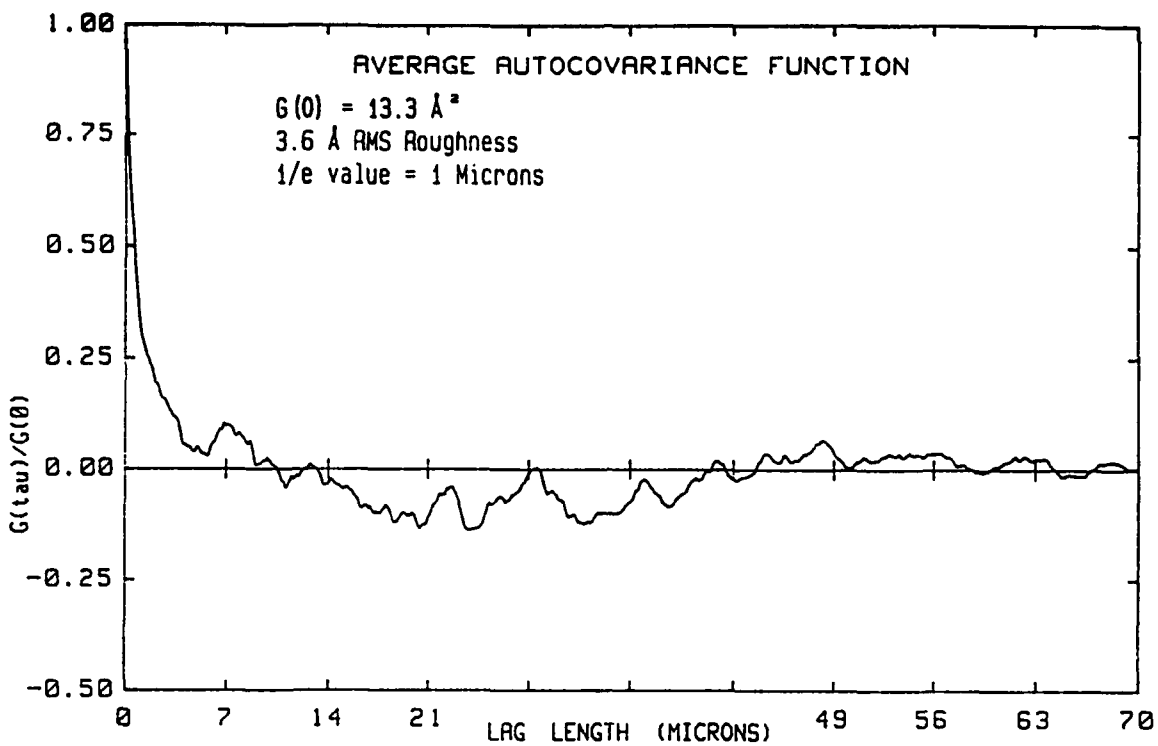
Figure 5.5   Average Autocovariance for Groove Top
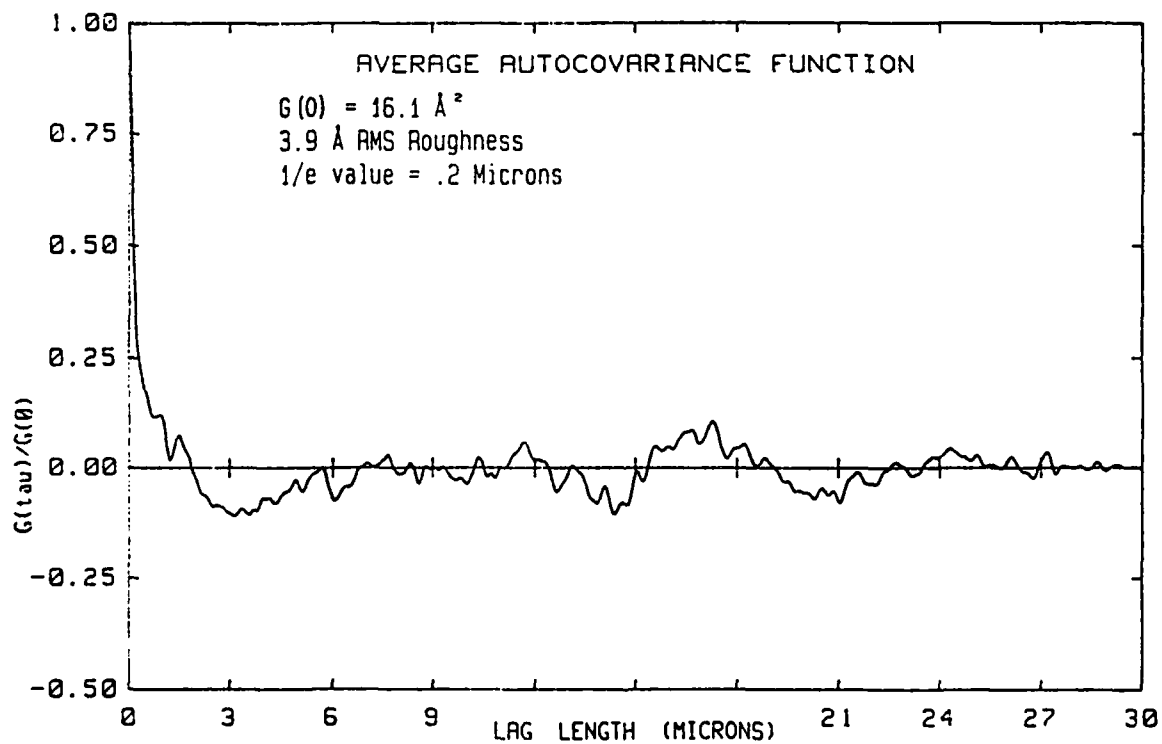
Figure 5.6   Average Autocovariance for Groove Bottom

78

B. SCALAR SCATTERING THEORY

The scalar theory developed assumes a Gaussian wave with constant phase incident on the binary optic. The phase changes after the aperture or source plane (see Figure 5.7) are due to the step height variations (i.e., the binary surface) and the surface roughness. It should be emphasized that this is a scalar solution and vector notation is used as a convenient shorthand in the following notation (i.e., the phase and polarization of the light are not considered in the theory presented).
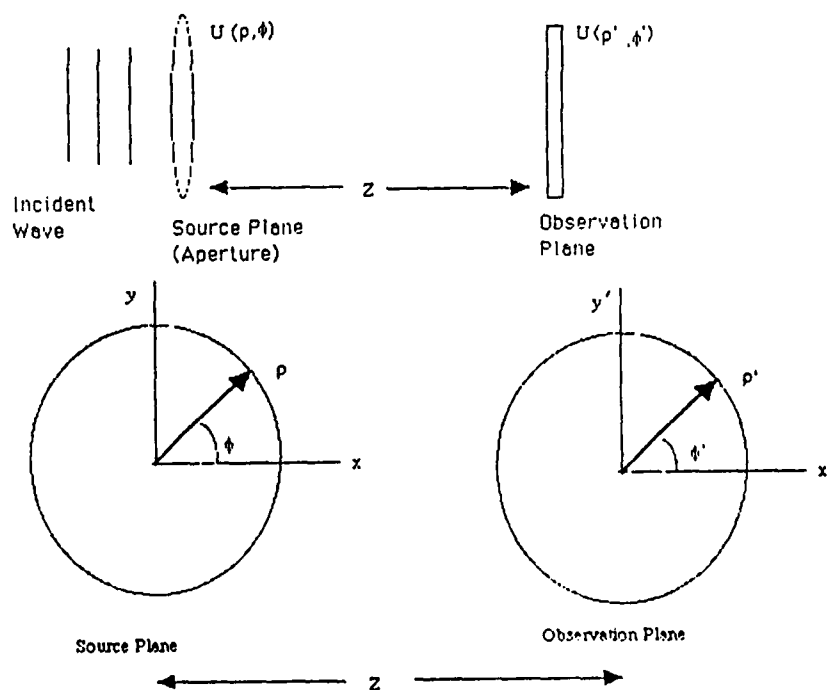
Figure 5.7   Diagram for Development of Theory

In Figure 5.7, z is the distance between the source and observation plane, and U is the intensity which has both amplitude and phase. The field after the aperture assumes no absorption within the optic or back scatter from light reflecting off the incident face of the binary optic. The on-axis incident amplitude is assumed to be unity with a Gaussian amplitude distribution.

For Fraunhofer diffraction the diffracted wave is: [Ref. 39]

$$U(x',y') = \frac{\exp\{ikz\} \exp\left\{\frac{ik}{2z}\left[x'^2 + y'^2\right]\right\}}{i\lambda z} \int\!\!\int_{-\infty}^{+\infty} U(x,y) \exp\left\{\frac{-i2\pi}{\lambda z}[xx' + yy']\right\} dxdy$$

(5.1)

where

U(x,y)   = amplitude in the source plane,
U(x',y')   = amplitude in the observation plane, and
z   = distance from the exit pupil to the observation plane.

In the experiment, the second spherical mirror focuses the collimated beam at the location of the detector which eliminates the quadratic phase term.

To account for phase changes due to the binary step pattern, a term accounting for the phase change is added. Assuming additional aberrations are introduced by random surface roughness, $\xi(x,y)$, an additional phase term is added to model this roughness. A Gaussian amplitude term is used for U(x,y) since a TEM_{00} laser was used as the source. These modifications are incorporated into Equation 5.2.

$$U(x',y') = \frac{\exp(ikz)}{i\lambda z} \iint_{-\infty}^{+\infty} dxdy \sum_p a_p \exp\left\{\frac{2\pi i p x}{D}\right\} \exp\left\{\frac{2\pi i \vec{\xi}(\rho)(n-1)}{\lambda}\right\} \exp\left\{\frac{-2\pi i \vec{\rho}\cdot\vec{\rho'}}{\lambda z}\right\} \exp\left\{\frac{-|\vec{\rho}|^2}{b^2}\right\}$$

(5.2)

where

$\sum_p a_p \exp\left\{\frac{2\pi i p x}{D}\right\}$ = Fourier series expansion of phase changes due to the binary height variations of surface,

$\exp\left\{\frac{2\pi i \vec{\xi}(\rho)(n-1)}{\lambda}\right\}$ = phase change due to the random roughness

$\vec{\xi}(\rho)$ = random roughness on surface,
n = index of refraction (constant),
D = period of binary optic (constant),
a_p = Fourier coefficients (calculated for binary surface profile),
λ = wavelength (constant),
b = radius of the beam width (constant), and

$\exp\left\{\frac{-|\vec{\rho}|^2}{b^2}\right\}$ = Gaussian laser beam with unit amplitude.

The integral in Equation 5.2 is evaluated in Appendix A, resulting in:

$$\langle|U|^2\rangle = \langle|U|^2\rangle_{\text{roughness}} + \langle|U|^2\rangle_{\text{specular}}$$

(5.3)

$$\langle|U|^2\rangle = \sum_p |a_p|^2 \left[\frac{C_1}{\left[1 + (\alpha - \beta_x)^2 \sigma^2\right]^{3/2}} + C_2 \exp\left\{-\frac{b^2}{2}(\alpha - \beta_x)^2\right\} \right]$$

(5.4)

$$C_1 = \frac{b^2 \pi^2 \sigma^2}{(\lambda z)^2} \left[\frac{2\pi(n-1)\delta}{\lambda}\right]^2$$

(5.5)

$$C_2 = \left(\frac{b^2 \pi}{\lambda z}\right)^2 \left[1 - \left[\frac{2\pi(n-1)\delta}{\lambda}\right]^2\right]$$

(5.6)

81

C. DETERMINATION OF FOURIER COEFFICIENTS

To evaluate the Fourier coefficients, a_p, the surface profile, h(x), must be known. To determine h(x) for the binary optic, measurements were made and then averaged from a photograph of the optic and a ruler at the same magnification using a Nomarski microscope (Figures 5.8 and 5.9). Each increment on the ruler in Figure 5.9 corresponds to 1 μm. The surface profile shown in Figure 5.10.

The height, H, was previously determined using the Talystep as 6554 Å. From the photographs, X_1 = 42.92 μm and X_2 = 86.5μm.

To analytically find the Fourier coefficients, we use:

$$\int_{-\infty}^{+\infty} \exp\left\{\frac{2\pi i h(x)(n-1)}{\lambda}\right\} dx = \int_{-\infty}^{+\infty} \sum_{p=-\infty}^{+\infty} a_p \exp\left\{\frac{2\pi i p x}{L}\right\} dx \qquad (5.7)$$

where

    n   = index of refraction,
    h(x) = surface profile as a function of x, and
    a_p = Fourier coefficients.

The integral in Equation 5.7 is evaluated in Appendix B, resulting in:

If p = 0, then

$$a_0 L = 2\left(x_2 - x_1\right) + \exp\left\{\frac{2\pi i H(n-1)}{\lambda}\right\} 2\left(\frac{L}{2} - x_2 + x_1\right) \qquad (5.8)$$
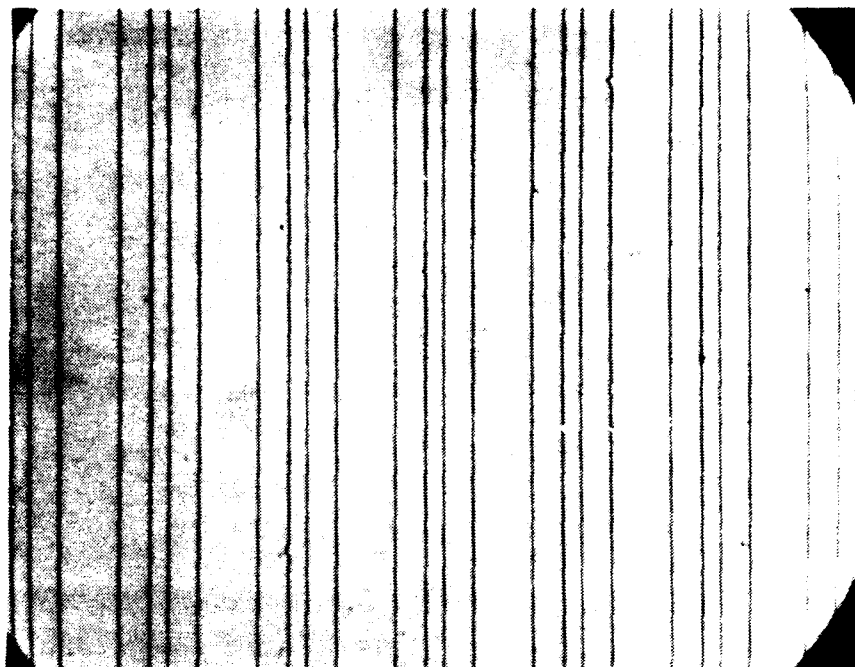
**Figure 5.8   Photograph of Binary Optic Using a
Nomarski Microscope**
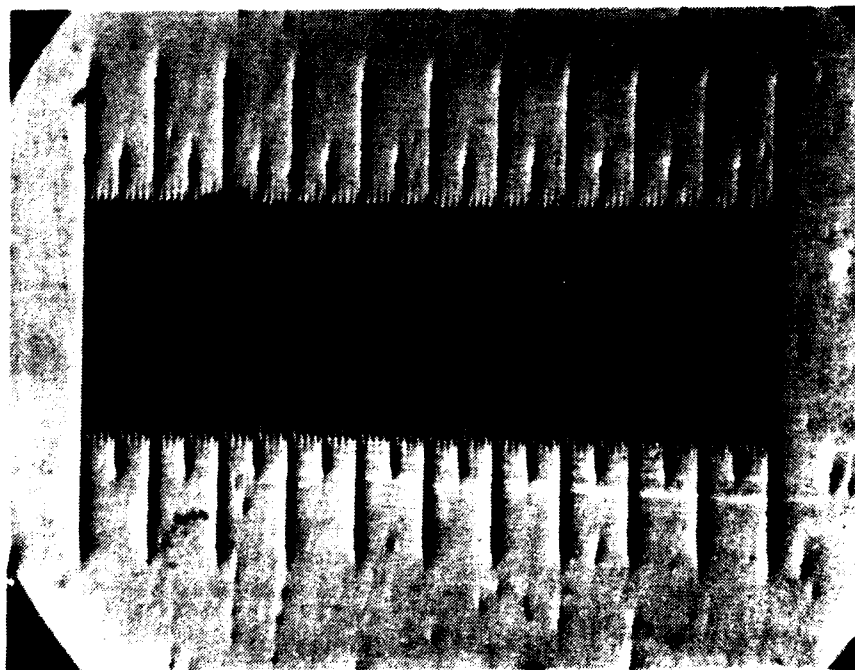
**Figure 5.9   Photograph of Ruler Using a
Nomarski Microscope**
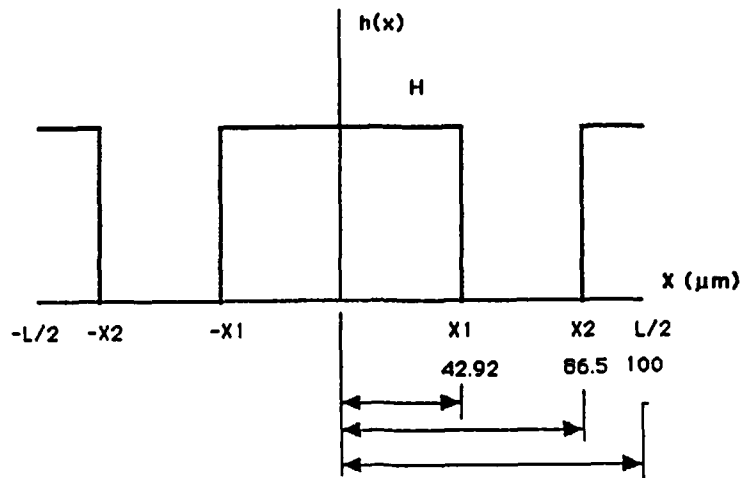
Figure 5.10   Surface Profile of Binary Optic

If $p \neq 0$, then

$$a_p = \frac{\left[1 - \exp\left\{\frac{2\pi iH(n-1)}{\lambda}\right\}\right]\left[\sin\left(\frac{2\pi px_1}{L}\right) - \sin\left(\frac{2\pi px_2}{L}\right)\right]}{-\pi p} \tag{5.9}$$

Substituting values from the experiment into 5.8 and 5.9 will give the Fourier coefficients. The period, L, is 100 μm; the height, H, is 6554 Å; X_1 is 42.92 μm; X_2 is 86.5 μm; and the index of refraction, n, for quartz is approximately 1.45702. The square of the magnitude of the Fourier coefficients is:

$$|a_0|^2 = 0.0219 \tag{5.10}$$

$$|a_1|^2 = 0.128 \tag{5.11}$$

$$|a_2|^2 = 0.141 \tag{5.12}$$

$$|a_3|^2 = 0.136 \tag{5.13}$$

84

More coefficients may be computed but they will have negligible effect on the calculation since these Fourier coefficients correspond to the measured beams of the binary optic and the magnitudes are later squared which makes their effect even smaller.

D. COMPUTER MODELING

The results from 5.3, 5.8, and 5.9 were programmed using Microsoft FORTRAN for an IBM personal computer. (The program requires a math co-processor.) A copy of the program is included in Appendix C. The data files generated by the program were plotted along with experimental values for the 25 and 500 μm pinholes using Hewlett Packard's Charting Gallery program on an IBM personal computer.

The following assumptions were used in modeling the theory. The form of the autocorrelation function is exponential (traditional form for function), the average surface height is 6554 Å, the rms surface roughness is 4 Å, and the period is 200 μm (where the average surface height and rms surface roughness are from the Talystep measurements, and the surface period was measured from photographs).

E. COMPARISON OF EXPERIMENT WITH THEORY

The theoretical values generated by the computer program in Appendix A are compared with experimental data. Two sets of graphs were produced. First, a set of graphs was produced to yield a best fit of the theory for each lobe to the

experiment by adjusting values for autocorrelation length and roughness (Figures 5.11 through 5.14). A second set of graphs was produced for each lobe using the same value of roughness and autocorrelation length (Figures 5.15 through 5.18). The lines on the graphs merely connect the data points with the exception of the solid line labeled "theory" which is obtained from theoretical equations.

The data is presented in a log-log format because the data varies over nine orders of magnitude. The abscissa has units of log sine angle of the scattered light in radians from the specular incident beam which is normal to the optic. Proceeding on the graphs from left to right, the angles become larger further away from the specular beam. Since near-angle scattering deals with angles less than one degree from the specular beam, the small angle approximation for the sine of the angle equalling the angle may be used. To illustrate the angular range of the instrument, consider Figure 5.11. The angular range is $10^{-3.85}$ to $10^{-2.55}$ radians which corresponds to 0.00809 to 0.16148 degrees. The ordinate is expressed in terms of log relative intensity; the data is normalized to the power in the specular peak for each beam.

1. **Best Fit Graphs (Figures 5.11, 5.12, 5.13, and 5.14)**

   a. **Main Lobe**

   In Figure 5.11, a best fit for the main lobe was obtained using a correlation length of 0.75 mm (750 μm) and roughness of 250 Å. The correlation length from Figure 5.5

86
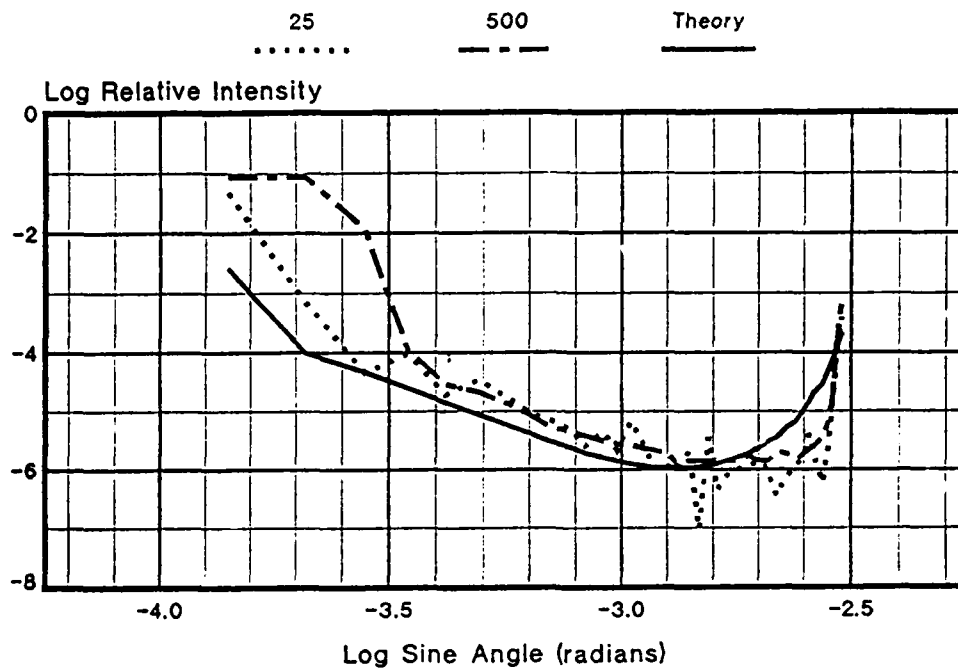
**Figure 5.11   Comparison of Theory for Main Lobe
(Autocorrelation Length 750 μm, Roughness 250 Å, Best Fit)**
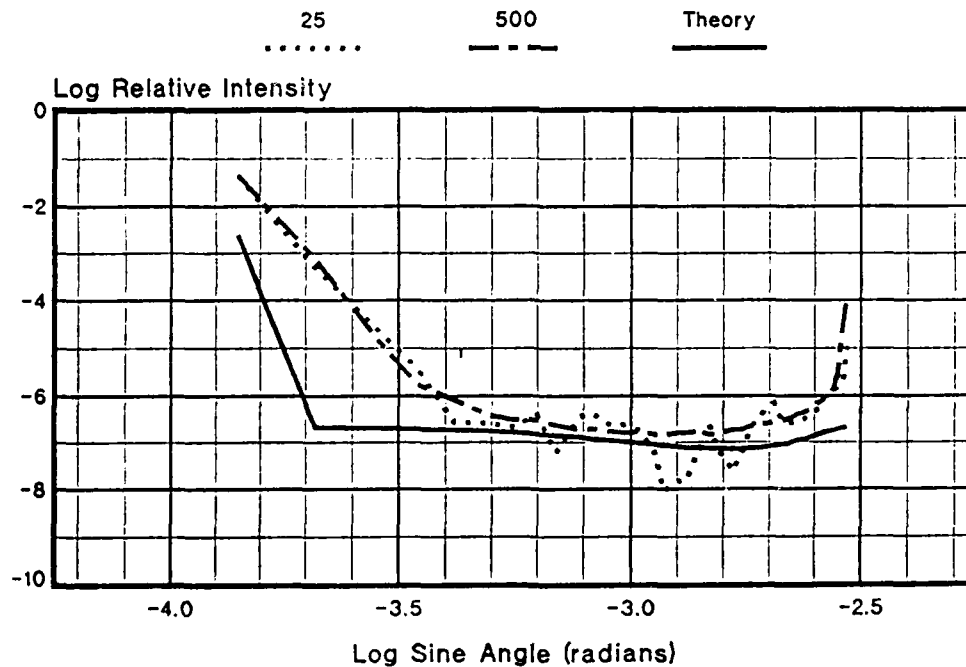
**Figure 5.12   Comparison of Theory for First Lobe
(Autocorrelation Length 100 μm, Roughness 50 Å, Best Fit)**

87
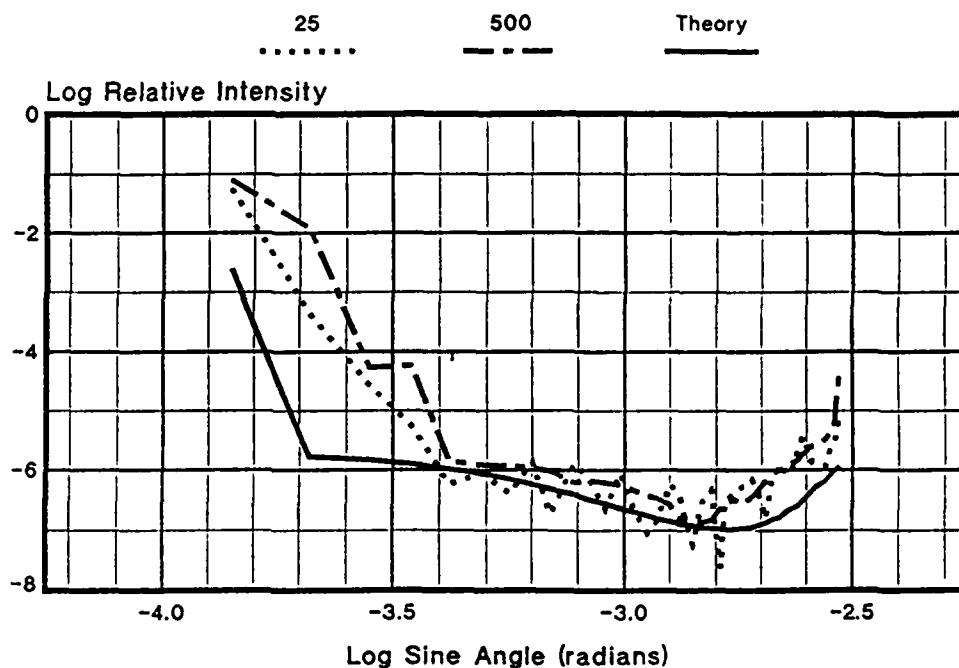
Figure 5.13   Comparison of Theory for Second Lobe
(Autocorrelation Length 200 μm, Roughness 75 Å, Best Fit)
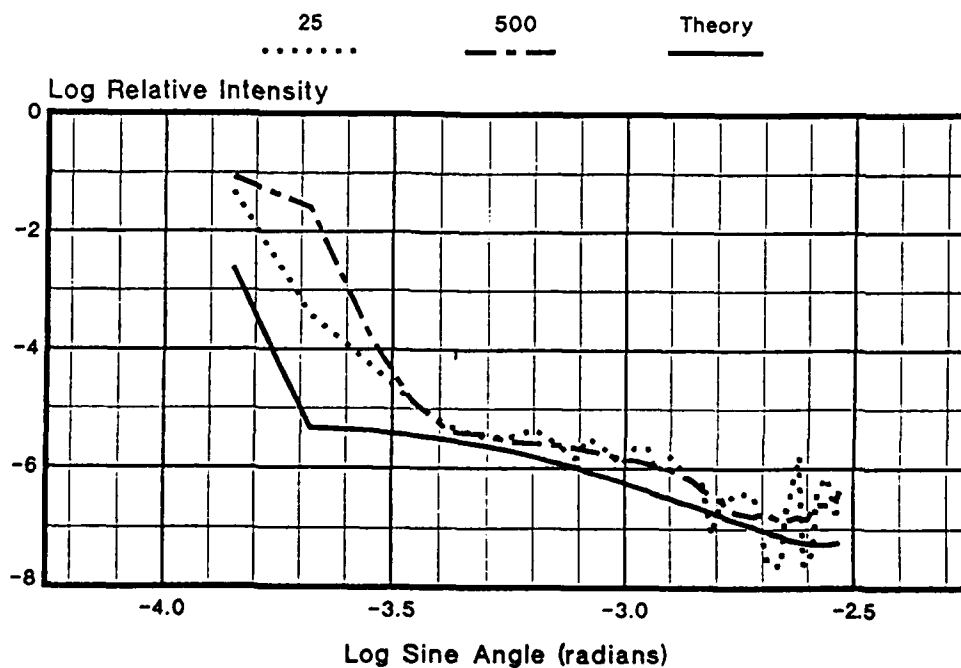
Figure 5.14   Comparison of Theory for Third Lobe
(Autocorrelation Length 200 μm, Roughness 125 Å, Best Fit)
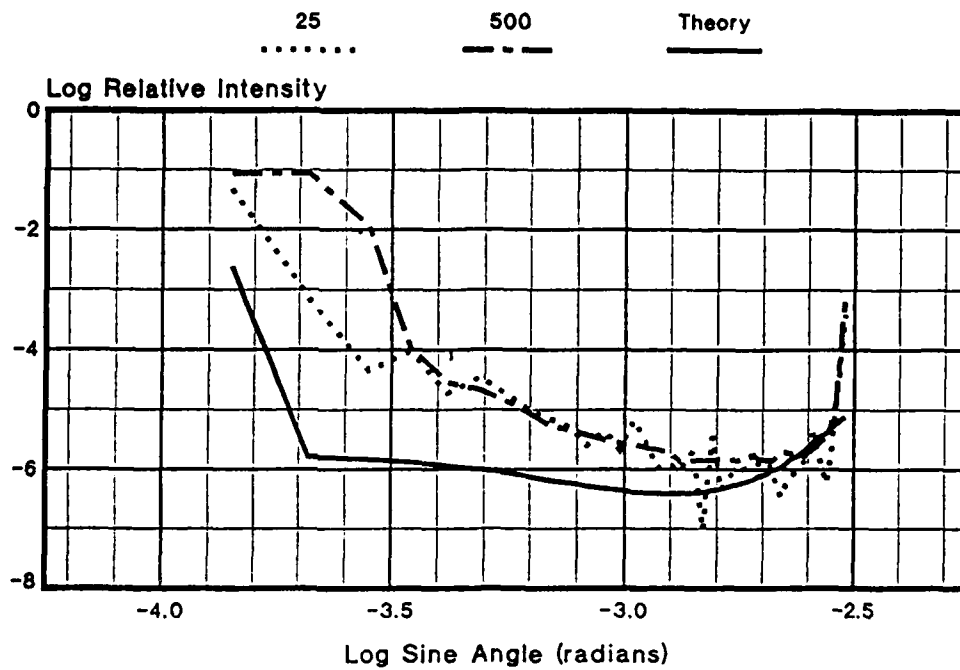
Figure 5.15 Comparison of Theory for Main Lobe
(Autocorrelation Length 175 μm, Roughness 80 Å, Average Fit)
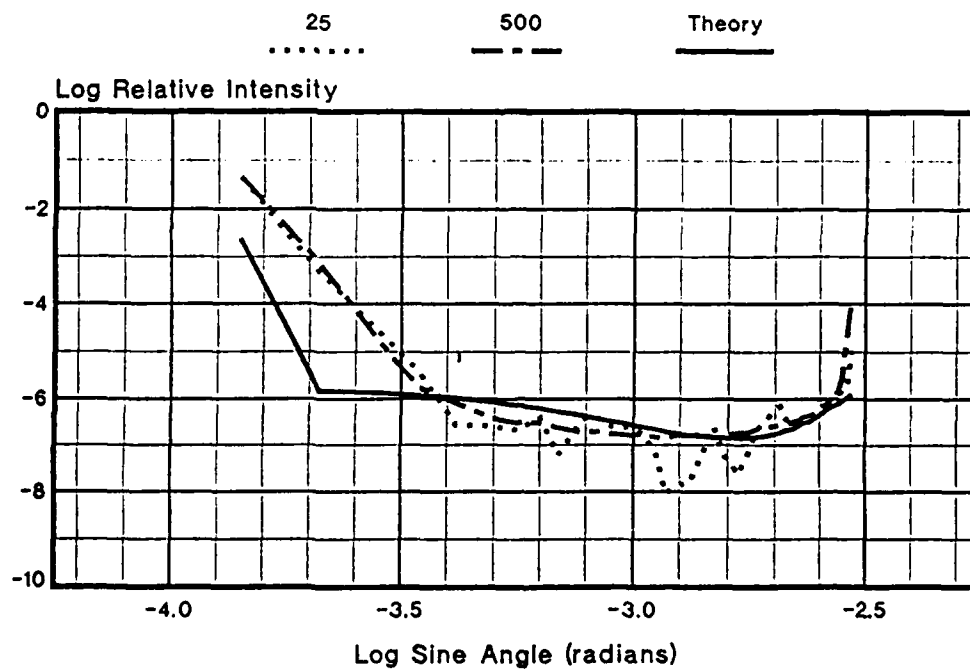
Figure 5.16 Comparison of Theory for First Lobe
(Autocorrelation Length 175 μm, Roughness 80 Å, Average Fit)

89

25 ······· 500 ——— Theory ——

Log Relative Intensity
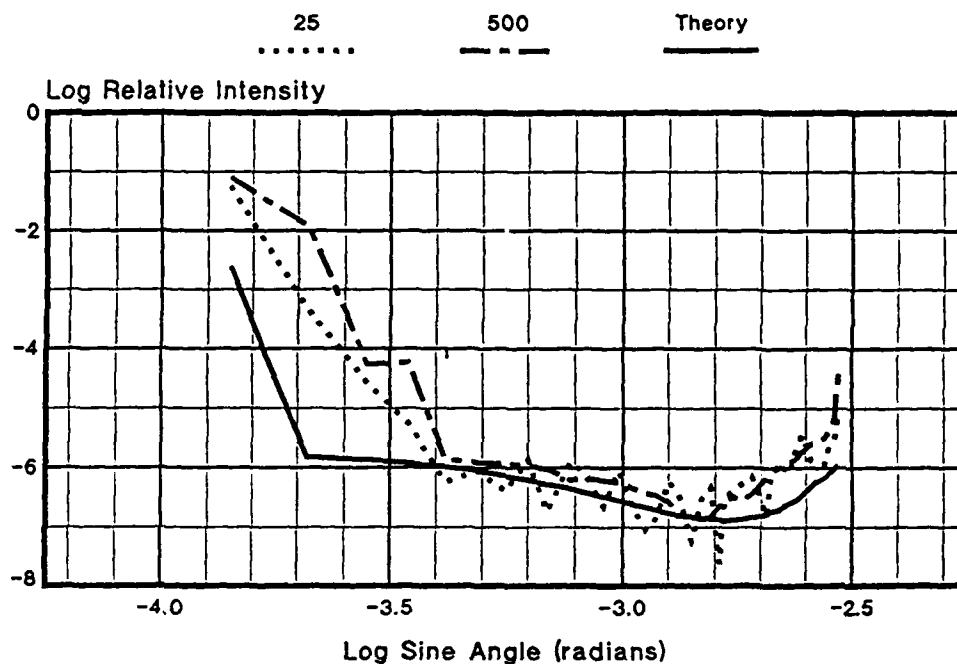
Figure 5.17   Comparison of Theory for Second Lobe
(Autocorrelation Length 175 μm, Roughness 80 Å, Average Fit)

25 ······· 500 ——— Theory ——

Log Relative Intensity
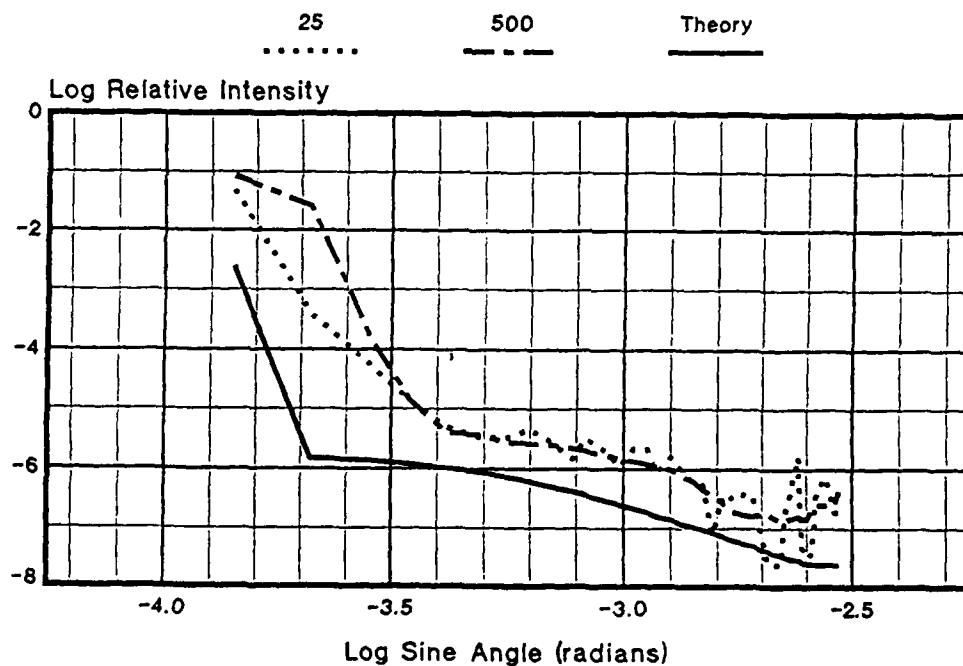
Figure 5.18   Comparison of Theory for Third Lobe
(Autocorrelation Length 175 μm, Roughness 80 Å, Average Fit)

90

is 1 μm at the 1/e point but previously measured correlation lengths from the Wyco profilometer ranged from 1 μm to 1,000 μm so 750 μm is reasonable. [Ref. 37] The roughness was much higher than the Talystep indicated (4 Å from Figure 5.4).

The scatter in the angular range of $10^{-3.85}$ to $10^{-3.68}$ is the specular scatter from the shape of the binary optic's surface and has a constant slope. It is evident that the theory predicts less scatter in this region. The scatter at angles larger than $10^{-3.68}$ is due largely to the micro-roughness on the surface; this area on the graph departs from the constant slope indicating the scatter due to roughness is overpowering the scatter due to the binary optic's shape. The theory agrees will with the experiment in the larger angular range. The upward trend of the data at $10^{-2.6}$ radians is from the detector sensing energy from the next lobe.

b. **First Lobe**

In Figure 5.12, more reasonable values were used for the autocorrelation length and roughness, 100 μm and 50 Å respectively. The theory predicted less scatter in the angular region of $10^{-3.85}$ to $10^{-2.5}$ radians. Overall, the theory is in good agreement with the experiment.

c. **Second Lobe**

A best fit for the data in Figure 5.13 used 200 μm correlation length and 75 Å roughness. The theory fit the data well for the angular range of $10^{-3.4}$ to $10^{-2.55}$ radians.

91

d. Third Lobe

A best fit for the data in Figure 5.14 used 200 μm for the correlation length and 125 Å roughness. Similar fit to the second lobe was obtained.

2. Average Fit Graphs (Figures 5.15, 5.16, 5.17, and 5.18)

Based on the best fit values for roughness and correlation length used to generate Figures 5.11 through 5.14, average values were obtained. An autocorrelation length of 175 μm and roughness of 80 Å was used for each lobe in Figures 5.15 through 5.18.

a. Main Lobe

In Figure 5.15, moderate discrepancies exist (i.e., an order of magnitude difference in the angular range $10^{-3.34}$ to $10^{-3.0}$ radians) where the theory previously fit the data well. The improper etch depth in the binary optic caused the main lobe to be lower in intensity than the other lobes and may account for the variation not present in the other lobes.

b. First Lobe

Overall, a good fit of the data in Figure 5.16 is obtained, the theory closely follows the experiment from $10^{-3.45}$ to $10^{-2.5}$ radians.

c. Second Lobe

In Figure 5.17, a good fit of the data is obtained. Theoretical results coincide well with the experiment for $10^{-3.4}$ to $10^{-2.55}$ radians.

d. Third Lobe

In Figure 5.18, results are similar to the main lobe, moderate discrepancies exist but the shape of the theory curve matches the shape of the experimental curves.

F. DISCUSSION OF RESULTS

The graphs in Figures 5.11 through 5.14 are best fits of the theory to the experiment by adjusting the autocorrelation length and surface roughness in the computer model. The average fit in Figures 5.15 through 5.18, which use the same value for the autocorrelation length and surface roughness, yielded poorer results, especially in the main lobe. Clearly, the values of autocorrelation length and roughness obtained from the Talystep measurements were either unrepresentative of the binary optic or the scalar theory requires further revision. The discrepancies in using larger values for the autocorrelation length and roughness may be attributable to the short scan length, 500 μm, used by the Talystep, which is a physical limitation of the instrument.

The short scan length used by the Talystep leads to two problems. The first problem concerns the instrument's inability to measure the overall roughness across the entire

optic. Therefore the Talystep may not be able to determine long autocorrelation lengths which primarily affect near-angle scattering. The Talystep is merely giving us a sample of the binary optic's surface, although runs are made in different areas of the optic. The question remains exactly how to determine the roughness and autocorrelation length. The variety in the Wyco's autocorrelation measurements are also frustrating. Perhaps the roughness and autocorrelation length vary with both the scan direction and the length of the run on the surface of the optic. The Wyco profilometer looks at different surface areas depending on the magnification of the lens used and will consequently generate different values. Additionally, the Wyco profilometer is highly dependent on the experience and skill of the operator, especially when using low magnifications which view a larger surface area of the optic.

In general, the graphs indicate that the theory conforms well to the experiment. The scalar theory follows the shape of the actual measurements, especially in the central angular region. The greatest disagreement occurs at the smallest angles, where the measurements exceeded the theory by several orders of magnitude.

The average fit for the graphs in Figures 5.15 through 5.18 indicates some disagreement between the theory and experiment for the main and third lobes. The worst fit occurs for the main lobe which may be attributable to the improper

etch depth of the optic which caused the main beam to be lower in intensity. The longer autocorrelation lengths may be justified by using the Wyco profilometer instead of the Talystep. The Talystep was not desirable due to the short profile lengths.

The results are very promising for using a scalar theory to predict the scattering from binary optics. The theory is relatively straight-forward and precludes time-intensive computer simulation using the full EM theory. The scalar theory is a good approximation but it did not account for:

- Back scatter off the front (incident) surface of the binary optic (i.e., all incident light is transmitted).

- Any inhomogeneities or defects present within the material the binary optic is made from.

- Polarization of the light.

Future work should determine how to best obtain measurements for the autocorrelation length and roughness of a binary optic. It may also be helpful to revise the theoretical model to include a random offset in the period of the binary step pattern. An attempt to account for the backscatter or polarization would complicate the model excessively.

VI. SUMMARY

A. ADVANTAGES AND APPLICATIONS FOR BINARY OPTICS IN MILITARY AND SPACE ELECTRO-OPTICAL SYSTEMS

In summary, binary optics will never totally replace conventional optics. However, by using binary optics the following may be realized:

- Correction of spherical and chromatic aberrations in conventional optics.

- Use of binary optics with conventional optics to form an equivalent asphere or achromatized element.

- Potential for low cost replication.

- A reduction in the optical elements required thereby resulting in a weight savings of approximately 33%.

- Coherent laser array beam addition to form a single powerful laser from many low power lasers.

- Laser beam profile shaping for more uniform intensity distribution for applications like laser radar.

- Laser multiplexer for use in laser radar.

- IR broadband imaging systems and IR filters for use in optically pumping far IR lasers.

- Solar cell concentrators to improve efficiency and reduce vulnerability to antisatellite threats.

- Flexibility in optical system design to generate arbitrary compact optical shapes which produce the desired optical wave front.

Other applications include helmet-mounted displays, uncooled thermal imagers, RLG readout optics, antireflective avionic displays, optical storage disc readout, laser beam

96

steering, and advanced electro-optic image processing at the detector (i.e., amacronics).

B. NEAR-ANGLE SCATTERING ANALYSIS AND RECOMMENDATIONS

1. Near-Angle Scattering Analysis

Results are very promising for using a scalar theory to predict the near-angle scattering from binary optics. The advantages of using a scalar theory are:

- The scalar theory is relatively straight-forward. Full EM theory is not required (i.e., polarization and phase angle of the light and boundary conditions are not required) to give an adequate approximation of scattering performance.

- The scalar theory is **not** computer intensive and may be implemented on an IBM personal computer, resulting in significant cost savings in comparison to computer simulations requiring full EM theory.

The shape of the theoretical curves closely follows the shape of the measured lobes in the central angular regions. The most disagreement with the scalar theory occurred at extremely small angles. Overall, experimental results agreed well with theoretical results. However, values for the autocorrelation length and surface roughness were much higher than the Talystep measurements indicated, which may be due to the short scan length limitation of the Talystep instrument. Longer autocorrelation lengths can be justified using a Wyco surface profilometer.

Unfortunately, the binary optic used had known manufacturing defects (i.e., it was etched to an improper depth) and time constraints precluded obtaining a better

specimen. Keep in mind that this is a very new technology, hence an imperfect sample was generated in the process of "working out the bugs" with the manufacturing process. Consequently, this should not be considered detrimental to this promising technology nor as a typical occurrence.

2. Recommendations

Since the scalar scattering theory developed depends on the autocorrelation length due to micro-roughness on the surface, future work is needed to determine how to best measure the autocorrelation length using either the Talystep or Wyco profilometer. Additional research could modify the theory by introducing a random offset to the periodicity of the surface structure (i.e., binary profile).

DoD should implement binary optics in future electro-optic systems or upgrades to current military and space systems. Binary optics is a worthwhile area for research dollars. The ability to improve optical system performance with potential significant cost savings as well as perform functions impossible with conventional lenses, makes binary-optics technology a true revolution that will change the electro-optics industry.

APPENDIX A

DEVELOPMENT OF SCALAR SCATTERING THEORY FOR BINARY OPTICS

Equation A.1 represents Fraunhofer diffraction from a binary optic and is evaluated in this appendix.

$$U(x',y') = \frac{\exp(ikz)}{i\lambda z} \iint_{-\infty}^{+\infty} dx\,dy \sum_p a_p \exp\left\{\frac{2\pi i p x}{D}\right\} \exp\left\{\frac{2\pi i \,\xi(\vec{\rho})\,(n-1)}{\lambda}\right\} \exp\left\{\frac{-2\pi i\, \vec{\rho}\cdot\vec{\rho}\,'}{\lambda z}\right\} \exp\left\{\frac{-|\vec{\rho}|^2}{b^2}\right\}$$

$$(A.1)$$

where

$$\sum_p a_p \exp\left\{\frac{2\pi i p x}{D}\right\}$$ = Fourier series expansion of phase changes due to the binary height variations of surface,

$$\exp\left\{\frac{2\pi i\, \xi(\vec{\rho})\,(n-1)}{\lambda}\right\}$$ = phase change due to the random roughness,

$\xi(\rho)$ = random roughness on surface,
n = index of refraction (constant),
D = period of binary optic (constant),
a_p = Fourier coefficients (calculated for binary surface profile),
λ = wavelength (constant),
b = radius of the beam width (constant), and

$$\exp\left\{\frac{-|\vec{\rho}|^2}{b^2}\right\}$$ = Gaussian laser beam with unit amplitude.

For convenience in notation, define $\rho = x\,\mathbf{x} + y\,\mathbf{y}$, where $\mathbf{x}$ and $\mathbf{y}$ are unit vectors along the x and y axes respectively in the source plane, and $\rho = x\,\mathbf{x}' + y\,\mathbf{y}'$, where $\mathbf{x}'$ and $\mathbf{y}'$ are unit vectors along the x'and y' axes respectively in the image plane.

The point spread function (PSF) is equal to the square of Equation A.1:

$$|U|^2 = \frac{1}{(\lambda z)^2} \iiiint_{-\infty}^{+\infty} dx\,dy\,dx''dy'' \sum_p \sum_q a_p a_q^* \exp\left\{\frac{2\pi i\,(px - qx'')}{D}\right\} \exp\left\{\frac{2\pi i\,(n-1)\left[\vec{\xi}(\vec{\rho}) \cdot \vec{\xi}(\vec{\rho}'')\right]}{\lambda}\right\}$$

$$\exp\left\{\frac{-2\pi i\,\vec{\rho}' \cdot \left[\vec{\rho} - \vec{\rho}''\right]}{\lambda z}\right\} \exp\left\{\frac{-\left|\vec{\rho}\right|^2 - \left|\vec{\rho}''\right|^2}{b^2}\right\} \tag{A.2}$$

Next, a change of variables is made. Let $\tau = \rho - \rho''$, $\tau_x = x - x''$, and $\tau_y = y - y''$. Making the change of variables in Equation A.2 results in:

$$|U|^2 = \frac{1}{(\lambda z)^2} \iint_{-\infty}^{+\infty} dx''dy'' \sum_p \sum_q a_p a_q^* \exp\left\{\frac{2\pi ix''(p-q)}{D}\right\} \exp\left\{\frac{-\vec{\rho}''^2}{b^2}\right\}$$

$$\iint_{-\infty}^{+\infty} d\tau_x d\tau_y \exp\left\{\frac{2\pi i\,(n-1)\left[\vec{\xi}(\vec{\tau}+\vec{\rho}'') \cdot \vec{\xi}(\vec{\rho}'')\right]}{\lambda}\right\} \exp\left\{\frac{-2\pi i\,\vec{\rho}' \cdot \vec{\tau}}{\lambda z}\right\} \exp\left\{-\left|\vec{\rho}'' + \vec{\tau}\right|\right\} \exp\left\{\frac{2\pi p\tau_x}{D}\right\} \tag{A.3}$$

Ensemble averaging both sides of Equation A.3 yields, for Gaussian random variables:[1]

$$\left\langle \exp\left\{\frac{2\pi i\,(n-1)\left[\vec{\xi}(\vec{\tau}+\vec{\rho}'') \cdot \vec{\xi}(\vec{\rho}'')\right]}{\lambda}\right\} \right\rangle = \exp\left\{-\left[\frac{2\pi(n-1)\delta}{\lambda}\right]^2 \left[1 - G(\vec{\tau})\right]\right\} \tag{A.4}$$

where

< > denotes the ensemble average,

δ = rms surface roughness, and

$G(\tau)$ = autocorrelation function.

Substituting Equation A.3 into the ensemble average of Equation A.2 yields:

---

[1]Sung, C. C. and Holzer, J. A., "Scattering of Electromagnetic Waves from a Rough Surface," Applied Physics Letters, Vol. 28, No. 8, pp. 429-431, 1976.

$$\langle |U|^2 \rangle = \frac{1}{(\lambda z)^2} \int\!\!\int_{-\infty}^{+\infty} dx''dy'' \sum_p \sum_q a_p a_q^* \exp\left\{\frac{2\pi i x''(p-q)}{D}\right\} \exp\left\{\frac{-|\vec{\rho''}|^2}{b^2}\right\}$$

$$\int\!\!\int_{-\infty}^{+\infty} d\tau_x d\tau_y \exp\left\{\frac{2\pi i p \tau_x}{D}\right\} \exp\left\{-\left[\frac{2\pi(n-1)\delta}{\lambda}\right]^2\left[1-G(\vec{\tau})\right]\right\} \exp\left\{\frac{-2\pi i\,\vec{\rho'}\cdot\vec{\tau}}{\lambda z}\right\} \exp\left\{\frac{-|\vec{\rho''}+\vec{\tau}|^2}{b^2}\right\}$$

$$\text{(A.5)}$$

Treating the random roughness as a perturbation on the binary profile, first-order perturbation theory is applied for near angle scatter since $\delta \ll \lambda$.

$$\exp\left\{-\left[\frac{2\pi(n-1)\delta}{\lambda}\right]^2\left[1-G(\vec{\tau})\right]\right\} \approx 1-\left[\frac{2\pi(n-1)\delta}{\lambda}\right]^2\left[1-G(\vec{\tau})\right] \qquad \text{(A.6)}$$

Substituting A.6 into A.5 resullts in:

$$\langle |U|^2 \rangle = \left[\frac{1}{\lambda z}\right]^2 \int\!\!\int_{-\infty}^{+\infty} dx''dy'' \sum_p \sum_q a_p a_q^* \exp\left\{\frac{2\pi i x''(p-q)}{D}\right\} \exp\left\{\frac{-|\vec{\rho''}|^2}{b^2}\right\}$$

$$\int\!\!\int_{-\infty}^{+\infty} d\tau_x d\tau_y \exp\left\{\frac{2\pi i p \tau_x}{D}\right\}\left[1-\left[\frac{2\pi(n-1)\delta}{\lambda}\right]^2\left[1-G(\vec{\tau})\right]\right] \exp\left\{\frac{-2\pi i\,\vec{\rho'}\cdot\vec{\tau}}{\lambda z}\right\} \exp\left\{\frac{-|\vec{\rho''}+\vec{\tau}|^2}{b^2}\right\} \text{ (A.7)}$$

First, expand the $d\tau_x d\tau_y$ integral in Equation A.7.

$$\left[1-\left[\frac{2\pi(n-1)\delta}{\lambda}\right]^2\right] \int\!\!\int_{-\infty}^{+\infty} d\tau_x d\tau_y \exp\left\{\frac{2\pi i p \tau_x}{D}\right\} \exp\left\{\frac{-2\pi i\,\vec{\rho'}\cdot\vec{\tau}}{\lambda z}\right\} \exp\left\{\frac{-|\vec{\rho''}+\vec{\tau}|^2}{b^2}\right\}$$

$$+\left[\frac{2\pi(n-1)\delta}{\lambda}\right]^2 \int\!\!\int_{-\infty}^{+\infty} d\tau_x d\tau_y\, G(\vec{\tau}) \exp\left\{\frac{2\pi i p \tau_x}{D}\right\} \exp\left\{\frac{-2\pi i\,\vec{\rho'}\cdot\vec{\tau}}{\lambda z}\right\} \exp\left\{\frac{-|\vec{\rho''}+\vec{\tau}|^2}{b^2}\right\} \qquad \text{(A.8)}$$

The first integral in A.8 is the specular component and the second integral is the scatter from the surface roughness. For the second integral in Equation A.8, assume the form of the autocorrelation function is exponential:

$$G(\vec{\tau}) = \exp\left\{\frac{-|\vec{\tau}|}{\sigma}\right\} \tag{A.9}$$

where σ = autocorrelation length.

Substituting Equation A.9 into the second integral of Equation A.8 results in:

$$\langle|U|^2\rangle_{\text{roughness}} = \left[\frac{2\pi(n-1)\delta}{\lambda}\right]^2 \iint_{-\infty}^{+\infty} d\tau_x d\tau_y \exp\left\{\frac{2\pi i p \tau_x}{D}\right\} \exp\left\{\frac{-|\vec{\tau}|}{\sigma}\right\} \exp\left\{\frac{-2\pi i \, \vec{\rho}' \cdot \vec{\tau}}{\lambda z}\right\} \exp\left\{\frac{-|\vec{\rho}'' + \vec{\tau}|^2}{b^2}\right\} \tag{A.10}$$

The following approximation can be made since the $\exp\{-|\tau|/\sigma\}$ falls off much more rapidly than the $\exp\{-|\rho'' + \tau|^2/b^2\}$ for $\sigma < b$:

$$\exp\left\{\frac{-|\vec{\tau}|}{\sigma}\right\} \exp\left\{\frac{-|\vec{\rho}'' + \vec{\tau}|^2}{b^2}\right\} \approx \exp\left\{\frac{-|\vec{\rho}''|^2}{b^2}\right\} \exp\left\{\frac{-|\vec{\tau}|}{\sigma}\right\} \quad \text{for all } \tau \tag{A.11}$$

To show Equation A.11 is a valid approximation, typical values are substituted into the left hand side of Equation A.11 ($\sigma = 100$ μm, $b = 5000$ μm, and $\tau = 2000$ μm):

$$\exp\left\{\frac{-|\tau|}{\sigma}\right\} \exp\left\{\frac{-|\vec{\rho}'' + \vec{\tau}|^2}{b^2}\right\} \geq \left(2.1 * 10^{-9}\right)\left[\exp\left\{\frac{-|\vec{\rho}''|^2}{b^2}\right\} \exp\left\{\frac{-|\vec{\tau}|^2}{b^2}\right\}\right] \tag{A.12}$$

$$\geq \left(2.1 * 10^{-9}\right)\left[0.85 \exp\left\{\frac{-|\vec{\rho}''|^2}{b^2}\right\}\right] \tag{A.13}$$

$$\approx \left(2.1 * 10^{-9}\right) \exp\left\{\frac{-|\vec{\rho}''|^2}{b^2}\right\} \tag{A.14}$$

102

Since $\exp(-|\tau|/\sigma)$ is equal to values from 1 to 0 while $\exp(-|\rho" + \tau|^2/b^2) \approx \exp(-|\rho"|^2/b^2)$, the approximation can be made that $\exp(-|\rho" + \tau|^2/b^2) \approx \exp(-|\rho"|^2/b^2)$ for $\sigma < b$. Substituting A.11 into A.7 using only terms associated with scattering due to the roughness results in:

$$\langle |U|^2 \rangle_{\text{roughness}} = \left[\frac{1}{\lambda z}\right]^2 \left[\frac{2\pi(n-1)\delta}{\lambda}\right]^2 \int\int_{-\infty}^{+\infty} dx"dy" \sum_p \sum_q a_p a_q^* \exp\left(\frac{2\pi i x"(p-q)}{D}\right) \exp\left(\frac{-|\vec{\rho"}|^2}{b^2}\right)$$

$$\exp\left(\frac{-|\vec{\rho"}|^2}{b^2}\right) \int\int_{-\infty}^{+\infty} d\tau_x d\tau_y \exp\left(\frac{2\pi i p \tau_x}{D}\right) \exp\left(\frac{-|\vec{\tau}|}{\sigma}\right) \exp\left(\frac{-2\pi i \vec{\rho'}\cdot\vec{\tau}}{\lambda z}\right) \quad (A.15)$$

Evaluating the second integral in Equation A.15 results in:

$$\left[\frac{2\pi(n-1)\delta}{\lambda}\right]^2 \frac{2\pi\sigma^2}{\left[1 + \left[(\alpha - \beta_x)^2 + \beta_y^2\right]\sigma^2\right]^{3/2}} \quad (A.16)$$

$$\alpha = \frac{2\pi m}{D} \quad (A.17)$$

$$\beta_x = \frac{2\pi x'}{\lambda z} \quad (A.18)$$

$$\beta_y = \frac{2\pi y'}{\lambda z} \quad (A.19)$$

Evaluating the first part of the integral in A.15, results in:

$$\frac{b^2 \pi}{2(\lambda z)^2} \sum_p \sum_q a_p a_q^* \exp\left(\frac{-b^2 \pi^2 (p-q)^2}{2D^2}\right) \quad (A.20)$$

Since $\exp\left(\frac{-b^2\pi^2(p-q)^2}{2D^2}\right) \approx 0$ for $p \neq q$, this simplifies to:

103

$$\frac{b^2 \pi}{2 (\lambda z)^2} \sum_p |a_p|^2 \tag{A.21}$$

Using the results from A.16 and A.21, the integral in A.15 simplifies to:

$$\langle |U|^2 \rangle_{roughness} = \frac{b^2 \pi}{2 (\lambda z)^2} \sum_p |a_p|^2 \left[\frac{2\pi(n-1)\delta}{\lambda} \right]^2 \frac{2\pi\sigma^2}{\left[1 + \left[(\alpha - \beta_x)^2 + \beta_y^2 \right] \sigma^2 \right]^{3/2}} \tag{A.22}$$

A further simplification of A.22 is possible if we examine the scatter in the plane (i.e., y' = 0 due to horizontal scan).

$$\langle |U|^2 \rangle_{roughness} = \sum_p |a_p|^2 \frac{\frac{b^2 \pi^2 \sigma^2}{(\lambda z)^2} \left[\frac{2\pi(n-1)\delta}{\lambda} \right]^2}{\left[1 + (\alpha - \beta_x)^2 \sigma^2 \right]^{3/2}} \tag{A.23}$$

Next, the specular scatter from the first integral in A.8 is evaluated resulting in:

$$\left[1 - \left[\frac{2\pi(n-1)\delta}{\lambda} \right]^2 \right] b^2 \pi \exp\left\{ 2\pi i x'' \left(\frac{x'}{\lambda z} - \frac{p}{D} \right) \right\} \exp\left\{ -b^2 \pi^2 \left(\frac{x'}{\lambda z} - \frac{p}{D} \right)^2 \right\} \exp\left\{ 2\pi i \frac{y'y''}{\lambda z} \right\} \exp\left\{ -b^2 \pi^2 \left(\frac{y'}{\lambda z} \right)^2 \right\} \tag{A.24}$$

Substituting A.24 into A.7 using only terms associated with the specular scatter results in:

$$\langle |U|^2 \rangle_{specular} = \frac{b^2 \pi}{(\lambda z)^2} \left[1 - \left[\frac{2\pi(n-1)\delta}{\lambda} \right]^2 \right] \int\!\!\int_{-\infty}^{+\infty} dx'' dy'' \sum_p \sum_q a_p a_q^* \exp\left\{ \frac{2\pi i x'' (p-q)}{D} \right\} \exp\left\{ \frac{-x''^2}{b^2} \right\}$$

$$\exp\left\{ \frac{-y''^2}{h^2} \right\} \exp\left\{ 2\pi i x'' \left(\frac{x'}{\lambda z} - \frac{p}{D} \right) \right\} \exp\left\{ -b^2 \pi^2 \left(\frac{x'}{\lambda z} - \frac{p}{D} \right)^2 \right\} \exp\left\{ 2\pi i \frac{y'y''}{\lambda z} \right\} \exp\left\{ -b^2 \pi^2 \left(\frac{y'}{\lambda z} \right)^2 \right\} \tag{A.25}$$

104

Evaluating Equation A.25 yields:

$$\langle |U|^2 \rangle_{specular} = \left(\frac{b^2 \pi}{\lambda z}\right)^2 \left[1 - \left[\frac{2\pi(n-1)\delta}{\lambda}\right]^2\right] \sum_p \sum_q a_p^* a_q \exp\left\{-b^2 \pi^2\left[\left(\frac{x'}{\lambda z} - \frac{p}{D}\right)^2 + \left(\frac{y'}{\lambda z}\right)^2\right]\right\}$$

$$\exp\left\{-b^2 \pi^2\left[\left(\frac{q}{D} - \frac{x'}{\lambda z}\right)^2 - \left(\frac{y'}{\lambda z}\right)^2\right]\right\} = 0 \quad \text{if } p \neq q$$

$$(A.26)$$

If p = q

$$\langle |U|^2 \rangle_{specular} = \left(\frac{b^2 \pi}{\lambda z}\right)^2 \left[1 - \left[\frac{2\pi(n-1)\delta}{\lambda}\right]^2\right] \sum_p |a_p|^2 \exp\left\{-2b^2 \pi^2\left[\left(\frac{x'}{\lambda z} - \frac{p}{D}\right)^2 + \left(\frac{y'}{\lambda z}\right)^2\right]\right\}$$

$$(A.27)$$

A further simplification of A.27 is possible if we consider scatter only in the horizontal plane (i.e., y' = 0).

$$\langle |U|^2 \rangle_{specular} = \left(\frac{b^2 \pi}{\lambda z}\right)^2 \left[1 - \left[\frac{2\pi(n-1)\delta}{\lambda}\right]^2\right] \sum_p |a_p|^2 \exp\left\{-2b^2 \pi^2\left(\frac{x'}{\lambda z} - \frac{p}{D}\right)^2\right\}$$

$$(A.28)$$

The integral in Equation A.7 has been evaluated and simplified using the results from A.23 and A.28.

$$\langle |U|^2 \rangle = \langle |U|^2 \rangle_{roughness} + \langle |U|^2 \rangle_{specular}$$

$$(A.29)$$

$$\langle |U|^2 \rangle = \sum_p |a_p|^2 \left[\frac{C_1}{\left[1 + (\alpha - \beta_x)^2 \sigma^2\right]^{3/2}} + C_2 \exp\left\{-\frac{b^2}{2}(\alpha - \beta_x)^2\right\}\right]$$

$$(A.30)$$

$$C_1 = \frac{b^2 \pi^2 \sigma^2}{(\lambda z)^2} \left[\frac{2\pi(n-1)\delta}{\lambda}\right]^2$$

$$(A.31)$$

$$C_2 = \left(\frac{b^2 \pi}{\lambda z}\right)^2 \left[1 - \left[\frac{2\pi(n-1)\delta}{\lambda}\right]^2\right]$$

$$(A.32)$$

105

APPENDIX B

DETERMINATION OF FOURIER COEFFICIENTS FOR BINARY OPTICS

Equation B.1 represents the integrals used to determine the Fourier coefficients from the binary optic's surface profile (refer to Figure 5.10 in Chapter V). The integrals in B.1 are evaluated in this appendix.

$$\int_{-\infty}^{+\infty} \exp\left\{\frac{2\pi i h(x)(n-1)}{\lambda}\right\} dx = \int_{-\infty}^{+\infty} \sum_{p=-\infty}^{+\infty} a_p \exp\left\{\frac{2\pi i p x}{L}\right\} dx \tag{B.1}$$

where

  n = index of refraction,
  $h(x)$ = surface profile as a function of x, and
  a_p = Fourier coefficients.

Using the orthogonality relation, Equation B.1 becomes:

$$\int_{-L/2}^{+L/2} \exp\left\{\frac{2\pi i h(x)(n-1)}{\lambda}\right\} \exp\left\{\frac{-2\pi i q x}{L}\right\} dx = \int_{-L/2}^{+L/2} \sum_{p=-\infty}^{+\infty} a_p \exp\left\{\frac{2\pi i (p-q) x}{L}\right\} dx \tag{B.2}$$

where L is the period of the step structure on the binary optic.

Evaluating B.2 results in:

$$\int_{-L/2}^{+L/2} \exp\left\{\frac{2\pi i h(x)(n-1)}{\lambda}\right\} \exp\left\{\frac{-2\pi i q x}{L}\right\} dx = \sum_{p=-\infty}^{+\infty} a_p \left[\frac{\sin(\pi(p-q))}{\frac{\pi(p-q)}{L}}\right] \tag{B.3}$$

if $p = q$, then

$$\frac{\frac{\sin(\pi(p-q))}{\pi(p-q)}}{L} = L \qquad (B.4)$$

if p ≠ q, then

$$\frac{\frac{\sin(\pi(p-q))}{\pi(p-q)}}{L} = 0 \qquad (B.5)$$

Consequently, B.3 simplifies to:

$$\int_{-L/2}^{+L/2} \exp\left\{\frac{2\pi i h(x)(n-1)}{\lambda}\right\} \exp\left\{\frac{-2\pi i p x}{L}\right\} dx = L\, a_p \qquad (B.6)$$

Next, the left side of the integral in B.6 is expanded:

$$\exp\left\{\frac{2\pi i H(n-1)}{\lambda}\right\} \int_{-L/2}^{-X_2} \exp\left\{\frac{-2\pi i p x}{L}\right\} dx + \int_{-X_2}^{-X_1} \exp\left\{\frac{-2\pi i p x}{L}\right\} dx$$

$$+ \exp\left\{\frac{2\pi i H(n-1)}{\lambda}\right\} \int_{-X_1}^{+X_1} \exp\left\{\frac{-2\pi i p x}{L}\right\} dx + \int_{+X_1}^{+X_2} \exp\left\{\frac{-2\pi i p x}{L}\right\} dx$$

$$+ \exp\left\{\frac{2\pi i H(n-1)}{\lambda}\right\} \int_{+X_2}^{+L/2} \exp\left\{\frac{-2\pi i p x}{L}\right\} dx \qquad (B.7)$$

where H is the height of binary optic step.   Evaluating B.7 and simplifying yields:

$$\frac{\exp\left\{\frac{2\pi i H(n-1)}{\lambda}\right\} \left[\sin\left(\frac{2\pi p x_2}{L}\right) - \sin(\pi p) - \sin\left(\frac{2\pi p x_1}{L}\right)\right] + \sin\left(\frac{2\pi p x_1}{L}\right) - \sin\left(\frac{2\pi p x_2}{L}\right)}{\frac{-\pi p}{L}} \qquad (B.8)$$

Setting B.8 equal to La_p and dividing through by L yields:

$$a_p = \frac{\exp\left\{\frac{2\pi i H(n-1)}{\lambda}\right\} \left[\sin\left(\frac{2\pi p x_2}{L}\right) - \sin(\pi p) - \sin\left(\frac{2\pi p x_1}{L}\right)\right] + \sin\left(\frac{2\pi p x_1}{L}\right) - \sin\left(\frac{2\pi p x_2}{L}\right)}{-\pi p} \qquad (B.9)$$

107

Collecting terms in B.9 and simplifying for p ≠ 0 results in:

$$a_p = \frac{\left[1 - \exp\left\{\frac{2\pi i H(n-1)}{\lambda}\right\}\right]\left[\sin\left(\frac{2\pi p x_1}{L}\right) - \sin\left(\frac{2\pi p x_2}{L}\right)\right]}{-\pi p}$$

(B.10)

Now consider the case for p = 0, Equation B.7 becomes:

$$\exp\left\{\frac{2\pi i H(n-1)}{\lambda}\right\}\int_{-L/2}^{-X_2} dx + \int_{-X_2}^{-X_1} dx + \exp\left\{\frac{2\pi i H(n-1)}{\lambda}\right\}\int_{-X_1}^{+X_1} dx$$

$$+ \int_{+X_1}^{+X_2} dx + \exp\left\{\frac{2\pi i H(n-1)}{\lambda}\right\}\int_{+X_2}^{+L/2} dx$$

(B.11)

Evaluating B.11 and simplifying:

$$a_0 L = 2(x_2 - x_1) + \exp\left\{\frac{2\pi i H(n-1)}{\lambda}\right\} 2\left(\frac{L}{2} - x_2 + x_1\right)$$

(B.12)

108

APPENDIX C

FORTRAN PROGRAM TO MODEL SCALAR SCATTERING FROM A BINARY OPTIC

```
C
C      LT LARRY V. CHIZEK
C      NAVAL POSTGRADUATE SCHOOL
C      29 MAY 1989
C
C      FORTRAN PROGRAM TO CALCULATE TRANSMISSIVE NEAR ANGLE SCATTER FROM
C      BINARY OPTIC USING SCALAR THEORY (FRESNEL DIFFRACTION INTEGRAL)
C      FOR NORMAL INCIDENCE.
C
C      PROGRAM ASSUMES GAUSSIAN FOR SPECULAR AND
C      SCATTERED COMPONENT WITH EXPONENTIAL AUTOCORRELATION
C
C      DECLARE VARIABLES
C
       INTEGER I,J,M,NPTS,T
C
C
       REAL ZIN,ZM,PI,X1,X2,H,N,L,LAMBDA,DELTA,C1,C2,ALPHA,BETA
       REAL IMPINT,A(51),RL(51),IM(51),U2(42),THETA(42),EV(42),EV25(42)
       REAL SUM1,SUM2,INCR,CL,STEP,BW,GAUSEXP,C3,C4,PKD,PKE,PK,DISP
C
       COMMON A,RL,IM,PI,H,N,L,X1,X2,LAMBDA,T
C
C
       OPEN (1,FILE-'C:EXP1L5.DAT')
       OPEN (2,FILE-'D:THEORY.DAT')
       OPEN (5,FILE-'C:EXP1L25.DAT')
C
C      DISP          DISPLACEMENT CONSTANT FOR LOBES
C      PKD           PEAK OF CALCULATED DATA
C      PKE           PEAK OF EXPERIMENTAL DATA FOR 500 PINHOLE
C      PK            PEAK OF EXPERIMENTAL DATA FOR 25 PINHOLE
C      EV            EXPERIMENTAL VALUES FROM 500 MICRON PINHOLE
C      EV25          EXPERIMENTAL VALUES FROM 25 MICRON PINHOLE
C      SUM1          CONSTANT
C      SUM2          CONSTANT
C      GAUSEXP       EXPONENT FOR GAUSSIAN FUNCTION
C      BW            BEAM WIDTH AT OPTIC
C      NPTS          NUMBER OF DATA PTS TO BE GENERATED
C      INCR          INCREMENT FOR DATA PTS IN INCHES
C      A(4)          FOURIER COEFFICIENTS
C      RL(4)         REAL PART OF FOURIER COEFF
C      IM(4)         IMAGINARY PART OF FOURIER COEFF
C      L             PERIOD OF BINARY OPTIC
C      X1            TRANSITION PT FOR HEIGHT ON SURFACE OF OPTIC IN METERS
C      X2            TRANSITION PT FOR HEIGHT ON SURFACE OF OPTIC IN METERS
C      H             HEIGHT OF BINARY OPTIC IN METERS
C      ZM            DISTANCE FROM BINARY OPTIC TO DETECTOR IN METERS
C      ZIN           DISTANCE FROM BINARY OPTIC TO DETECTOR IN INCHES
C      LAMBDA        WAVELENGTH OF HENE LASER
C      N             INDEX OF REFRACTION FOR BINARY OPTIC
C      DELTA         RMS SURFACE ROUGHNESS OF OPTIC IN METERS
C      U2            INTENSITY OF SCATTERED LIGHT
C      C1            CONSTANT
C      C2            CONSTANT
C      C3            CONSTANT
C      C4            CONSTANT
C      ALPHA         CONSTANT
C      BETA          CONSTANT
C      THETA         SCATTER ANGLE IN RADIANS
```

```
C     PI          PI RADIANS
C     STEP        INCREMENT FOR ANGULAR RESOLUTION IN INCHES
C     I           COUNTER
C     J           COUNTER
C     M           COUNTER
C
C     INITIALIZE VARIABLES
C
      DISP = 0.3164E-2
      H = 6554E-10
      L = 200E-6
      X1 = 42.92E-6
      X2 = 86.5E-6
      N = 1.46
      LAMBDA = 6328E-10
      DELTA = 80.0E-10
      PI = 3.1416
      CL = 175.0E-6
      ZIN = 71.6
      ZM = 1.819
      INCR = 0.005
      NPTS = 42
      BW = 1E-2
      PKD = 0
      PKE = 0
      PK = 0
C
C     INITIALIZE ARRAYS
C
      DO 100 I = 1,NPTS
C
            U2(I) = 0
            EV(I) = 0
            EV25(I) = 0
            THETA(I) = 0
C
  100 CONTINUE
C
      DO 200 J = 1,51
C
            A(J) = 0
            RL(J) = 0
            IM(J) = 0
C
  200 CONTINUE
C
C
C     CALCULATE ANGLE IN RADIANS
C
      DO 300 I = 1,NPTS
C
            STEP = I * INCR
C
            THETA(I) = ALOG10(STEP/ZIN)
C
  300 CONTINUE
C
C
C
C     CALCULATE CONSTANTS
```

110

```
C
        C1 = (1 - ((2.0*PI*(N-1)*DELTA)/LAMBDA)**2)*(1/(LAMBDA*ZM))**2
        C2 = (((2.0*PI*(N-1)*DELTA)/LAMBDA)**2)*((BW/2)/(LAMBDA*ZM))**2
        C3 = ((BW/2)**4)*(PI**2)
        C4 = C1 * C3

C
C
C       CALCULATE INTENSITIES FOR SCATTERING ANGLES
C
        DO 600 I = 0,NPTS-1
C
            DO 700 M = -25,25,1
C
                T = 26 + M
C
                STEP = ((I*INCR)/ZIN)  +  (1.0*DISP)
C
                CALL FRCF(M)
C
                GAUSEXP = -2.0*(((PI*BW)/2)**2)*((STEP/LAMBDA
     /                       - (M/L)))**2
C
                SUM1 = A(T)*C4*EXP(GAUSEXP)
C
                ALPHA = (2.0*PI*M)/L
C
                BETA = (2.0*PI*STEP)/LAMBDA
C
                SUM2 = (A(T)*((PI**2)*(CL**2)*C2))/
     /                   (1 + (CL*(ALPHA - BETA))**2)**1.5
C
                U2(I+1) = SUM1 + SUM2 + U2(I+1)
C
700         CONTINUE
C
            READ(5,*) EV25(I+1)
C
            READ(1,*) EV(I+1)
C
C       NORMALIZE LOG OF DATA
C
            IF (I .NE. 0) THEN

                PKD = U2(1)
C
C       TAKE LOG AND NORMALIZE EXP DATA
C
                PKE = EV25(1)*(244.0)
C
                PK = EV25(1)
C
                U2(I+1) = U2(I+1)/PKD
C
                U2(I+1) = ALOG10(U2(I+1))
C
                EV(I+1) = EV(I+1)/PKE
C
                EV(I+1) = ALOG10(EV(I+1))
C
```

```
                          EV25(I+1) - EV25(I+1)/PK
C
                          EV25(I+1) - ALOG10(EV25(I+1))
C
                          WRITE(2,44)  THETA(I+1),EV25(I+1),EV(I+1),U2(I+1)
  44                      FORMAT(1X,'0',E10.3,1X,E10.3,1X,E10.3,1X,E10.3)
C
                  ENDIF
C

  600     CONTINUE
C
C

          STOP
C

          END
C
C         SUBROUTINE FRCF CALCULATES MAGNITUDE SQUARED OF FOURIER COEFFICIENTS
C         FOR SURFACE OF BINARY OPTIC
C

          SUBROUTINE FRCF(M)
C

          REAL K1,K2,K3,RL(51),IM(51),A(51),LAMBDA,H,N,PI,L,X1,X2
C

          INTEGER M,T
C

          COMMON A,RL,IM,PI,H,N,L,X1,X2,LAMBDA,T
C
C         K1        CONSTANT
C         K2        CONSTANT
C         K3        CONSTANT
C
C         CALCULATE CONSTANTS
C

          K1 - (2.0*PI*H*(N-1))/LAMBDA
          K2 - (2.0/L)*((L/2) - X2 + X1)
          K3 - SIN((2.0*PI*M*X1)/L) - SIN((2.0*PI*M*X2)/L)
C

          IF (M .EQ. 0) THEN
C

                  RL(T) - (2.0*(X2-X1)/L) + (K2 * COS(K1))
                  IM(T) - K2 * SIN(K1)
                  A(T) - (RL(T)**2 + IM(T)**2)
C

          ELSE
C

                  RL(T) - ((1.0 - COS(K1))*K3)/(-PI*M)
                  IM(T) - (SIN(K1)*K3)/(PI*M)
                  A(T) - (RL(T)**2 + IM(T)**2)
C

          ENDIF
C

          RETURN
C

          END
```

LIST OF REFERENCES

1. Fisher, Robert E.; "An Interview with Wilfrid Veldkamp: Binary Optics and its Applications," SPIE OE Reports, pp. 1, 15, July 1989

2. Veldkamp, W. B., "DARPA/TTO Program IR Binary Optics," Semiannual Technical Summary Report to the Defense Advanced Research Projects Agency, December 1984

3. Breault, Robert P., "Current Technology of Stray Light," Proceedings SPIE, Vol. 675, pp. 4-13, 1986

4. Ricks, Douglas W., "Near-Angle Scattered Light from Binary Optics," Proceedings SPIE, Vol. 818, pp. 54-60, 1987

5. Baber, S. Charles, "Application of High Resolution Laser Writers to Computer Generated Holograms and Binary Diffractive Optics," Proceedings SPIE, Vol. 1052, pp. 66-76, 1989

6. Cox, J. Allen, "Overview of Diffractive Optics at Honeywell," Proceedings SPIE, Vol. 1052, pp. 25-31, 1989

7. Fritz, Teresa A. and Cox, J. Allen, "Diffractive Optics for Broadband Infrared Imagers: Design Examples," Proceedings SPIE, Vol. 1052, pp. 25-31, 1989

8. Logue, James, "Fabrication of Binary Optics Using Electron Beam Lithography," Proceedings SPIE, Vol. 884, pp. 95-104, 1988

9. Guest, C. C., and others, "Design of Computer Generated Holograms for Electron Beam Fabrication by Means of a Computer Aided Design System," Proceedings SPIE, Vol. 884, pp. 33-37, 1988

10. Cowan, James J., and Slafer, Dennis, "Holographic Embossing at Polariod: The Polaform Process," Proceedings SPIE, Vol. 600, pp. 49-56, 1985

11. Futhey, John A., "Diffractive Bifocal Intraocular Lens," Proceedings SPIE, Vol. 1052, pp. 142-149, 1989

12. Swanson, Gary J. and Vedlkamp, Wilfrid B., "Infrared Applications of Diffractive Optical Elements," Proceedings SPIE, Vol. 883, pp. 155-162, 1988

113

13. Fritz, Teresa A. and Cox, J. Allen, "Diffractive Optics for Broadband Infrared Imagers," Proceedings SPIE, Vol. 1052, pp. 25-31, 1989

14. Byrne, D. M., "Diffractive Infrared Filters Fabricated by Electron-Beam Lithography," Proceedings SPIE, Vol. 560, pp. 70-81, 1985

15. Byrne, D. M., Brouns, A. J., Case, F. C., Tiberio, R. C., Whitehead, B. L., and Wolf, E. D., "Infrared Mesh Filters Fabricated by Electron Beam Lithography," J. Vac. Sci. Technol. B 3 (1), pp. 268-271, 1985

16. Leger, J. R., Holz, M., Swanson, G. J., and Veldkamp, W. B., "Coherent Laser Beam Addition: An Application of Binary-Optics Technology," The Lincoln Laboratory Journal, Vol. 1, No. 2, pp. 225-246, 1988

17. Talbot, W. H. F., "Facts Relating to Optical Science. No. 4," Philos, Mag., Vol. 9, No. 401, 1836

18. Veldkamp, W. B., "Laser Beam Profile Shaping with Binary Diffraction Gratings," Optics Communications, Vol. 38, No. 5,6, pp. 381-386,1981

19. Veldkamp, W. B., "Laser Beam Profile Shaping with Interlaced Binary Diffraction Gratings," Applied Optics, Vol. 21, No. 17, pp. 3209-3212, 1982

20. Veldkamp, W. B., _Laser Radar Beam Control with Holographic Diffraction Gratings_, M.I.T. Lincoln Laboratory, p. 197-204.

21. Foley, Theresa M., "Solar Array under Development to Resist Hostile Threats," Aviation Week & Space Technology, pp. 47-48, 15 August 1988

22. Francisco, San, "USAF Funding R & D to Design More Efficient Solar Cells," Aviation Week & Space Technology, pp. 81-85, 10 April 1989

23. Cowan, James J., "Holographic Honeycomb Microlens," Optical Engineering, Vol. 24, No. 5, pp. 796-802, 1985

24. Telephone conversation between James Cowan, Polaroid Corp. and the author, 4 April 1989.

25. Cowan, James J., and Slafer, W. Dennis, "Holographic Embossing at Polaroid: The Polafoam Process," Proceedings SPIE, Vol. 600, pp. 49-56, 1985

26. Honeywell, "Binary Optics Applications," Promotional Viewgraph 89-CRV-0743

27. Telephone conversation between Allen Cox, Honeywell, and the author, 5 April 1989

28. Telephone conversation between Dr. William French, 3M, and the author, 26 April 1989

29. Telephone conversation between Tom McHugh, Perkin Elmer, and the author, 5 April 1989

30. Telephone conversation between CPT Miles Scott, USAF, and the author, 5 April 1989

31. Ricks, Douglas W., "Relationship Between Near-Angle Scatter and Surface Characteristics," Proceedings SPIE, Vol. 1009, pp. 126-133, 1989

32. Telephone conversation between Gary Swanson, M.I.T. Lincoln Labs, and the author, 24 July 1989

33. Lastovka, J. B., "An Optical Apparatus for Very-Small-Angle Light Scattering Design, Analysis, and Performance," The Bell System Technical Journal," Vol. 55, No. 9, pp. 1225-1293, 1976

34. Nicodemus, Fred E., "Directional Reflectance and Emissivity of an Opaque Surface," Applied Optics, Vol. 4, No. 7, pp. 767-773, 1965

35. Davis, Leo, and Kepros, John G., "Improved Facility for BRDF/BTDF Optical Scatter Measurements, "Proceedings SPIE, Vol. 675, pp. 24-29, 1986

36. Private conversations between J. Merle Elson, Naval Weapons Center, China Lake, and the author, May 1989

37. Bennett, Jean M. and Mattsson, Lars, Introduction to Surface Roughness and Scattering, Institute of Physics, Uppsala University, Uppsala, Sweden, pp. 20-21, 1988

38. Private conversation between Douglas W. Ricks, Naval Weapons Center, China Lake, and the author, 24 May, 1989

39. Goodman, J. W., Introduction to Fourier Optics, p. 61, McGraw-Hill, New York, 1968

INITIAL DISTRIBUTION LIST

		NO. COPIES
1.	Defense Technical Information Center Cameron Station Alexandria, Virginia 22304-6145	2
2.	Library, Code 0142 Naval Postgraduate School Monterey, California 93943-5002	2
3.	Chairman, Code 62 Department of Electrical and Computer Engineering Naval Postgraduate School Monterey, California 93943-50002	1
4.	Commander Naval Space Command Attn: Code N3 Dahlgren, Virginia 22448	1
5.	United States Command Attn: Technical Library Peterson AFB, Colorado 80914	1
6.	Director Navy Space Systems Division (OP943) Washington, DC 20350-2000	1
7.	Dr. Rudolf Panholzer Space Systems Academic Group, Code 72 Naval Postgraduate School Monterey, California 93943-5000	1
8.	Professor John Neighbours Physics, Code 61NB Naval Postgraduate School Monterey, California 93943-5000	1
9.	Professor John Powers Electrical Engineering, Code 62 Naval Postgraduate School Monterey, California 93943-5000	1
10.	Douglas W. Ricks Naval Weapons Center, Code 3151 China Lake, California 939555	1

11. Dr. J. Merle Elson   1
    Naval Weapons Center, Code 3818
    China Lake, California 93555

12. LTC Daniel Lynch   1
    U.S. Army Space Program Office
    2810 Old Lee Highway
    Fairfax, Virginia 22031

13. LT Larry Chizek   2
    Strategic Weapons Facility Pacific
    Silverdale, Washington 98315-5500